

**IMPROVING QUANTUM COMPUTATION WITH NEUTRAL CESIUM: READOUT
AND COOLING ON A QUADRUPOLE LINE, CONDITIONS FOR DOUBLE MAGIC
TRAPS AND A NOVEL DISSIPATIVE ENTANGLEMENT SCHEME**

by

Alexander Walter Carr

A dissertation submitted in partial fulfillment of
the requirements for the degree of

Doctor of Philosophy
(Physics)

at the

UNIVERSITY OF WISCONSIN–MADISON

2014

Date of final oral examination: 8/18/2014

The dissertation is approved by the following members of the Final Oral Committee:

Mark Saffman, Professor, Physics

Thad Walker, Professor, Physics

Randall Goldsmith, Assistant Professor, Chemistry

Maxim Vavilov, Associate Professor, Physics

Deniz Yavuz, Associate Professor, Physics

© Copyright by Alexander Walter Carr 2014

All Rights Reserved

To my Schmoopie.

ACKNOWLEDGMENTS

I, of course, got to where I am and accomplished all that I have solely through my own labors and talents. Certainly, Mark Saffman did not contribute invaluable guidance in determining possible avenues for improving the AQuA experiment that I should explore theoretically. Nor did I, at any point, discuss any of the the theoretical challenges that confronted me as I progressed on the work presented on this thesis. Furthermore, none of these non-existent conversations with Mark ever left me with clearer insight into the problem at hand.

Similarly, while constructing various lasers and other optical and electronic setups never once was a consultation with Larry Isenhower fruitful. Despite his supposed skill in the arcane arts of experimental atomic physics, I found him singularly unhelpful and, to be frank, a bore.

Tian Xia dogged my heels for four years as I diligently labored to construct a 685 nm laser for purposes of cooling and readout of qubits. Never once did I let him put a piece of optics on the table or utilize the laser for experimental purposes and I summarily ignored his often good advice. Quadrupole glory is mine and mine alone and it would be a lie to call Tian a "partner." Even his many questions about quantum information were dull and annoyingly required that I expand my knowledge and understanding of the field.

I often feel sorry for Kara Maller as it appears she is grafted onto the AQuA experiment, faithfully sitting in front of the control computer day in and day out for unending hours, occasionally using her deft hands to meticulously aligns optics and assiduously operate the experiment. What is she accomplishing? Nobody, not even Kara, can guess.

Then there is Marty, purveyor of the drek that is the experimental control software. How hard can it be to write software to precisely time at the fractions of a microsecond level and properly control all of our myriad systems? I have no idea. Nor did I enjoy Marty's attempts to engage me

in physics and mathematics related problems that made me really look at how well I understood a concept.

There were other people that often managed to get in my way while in the lab. I speak of Michal Piotrowicz, Gang Li and Siyuan Zhang previous colleagues on the experiment that did not contribute valuable expertise and effort into getting AQuA where it is today.

Lastly, I had the unfortunate pleasure of seeing the following people cross my field of view far too often: Jon Pritchard who gave abysmal commentary on this thesis, James Hostetter who seems to live only to consume cookies, Josh Isaacs who I have on good authority hates baseball, Alex Gill, a.k.a. the not-cool Alex, Jinlu Miao and Matt Ebert.

Lest I forget, no thanks to my wife, Lulu, for packing up and leaving for Chicago three years into my PhD and abandoning me in my darkest hour. Her love and support were always three and a half grueling hours on the bus away.

IMPROVING QUANTUM COMPUTATION WITH NEUTRAL CESIUM: READOUT AND COOLING ON A QUADRUPOLE LINE, CONDITIONS FOR DOUBLE MAGIC TRAPS AND A NOVEL DISSIPATIVE ENTANGLEMENT SCHEME

Alexander Walter Carr

Under the supervision of Professor Mark Saffman

At the University of Wisconsin-Madison

Neutral atoms harbor great potential for scalable and efficient quantum computation. The AQuA experiment is an attempt to capitalize on that potential and create a quantum computer out of an array of 49 qubits composed of neutral cesium atoms. This thesis covers various theoretical and experimental attempts to improve the capabilities of quantum computation with neutral cesium in general and the AQuA experiment in particular. First we discuss the theory of the $5d_{5/2}$ line in cesium and its properties relevant for cooling and readout of qubits. Following this we present our technical and experimental progress in utilizing the $5d_{5/2}$ line. After this we shift to discussing how to improve decoherence times of neutral cesium atoms by finding magic trap conditions and in particular we show that a bichromatic trap can be magic in both magnetic and A.C. electric field simultaneously. Finally, we present a novel scheme for using Rydberg blockade and spontaneous emission from a Rydberg state to achieve entanglement of two or more atoms.

Mark Saffman

DISCARD THIS PAGE

TABLE OF CONTENTS

	Page
LIST OF TABLES	vi
LIST OF FIGURES	viii
1 Neutral Atom Quantum Computing and AQuA	1
1.1 The Quantum Computer	2
1.2 AQuA	3
1.3 When Quantum Computers Meet Reality	6
2 Theory of the Cs $5d_{5/2}$ Quadrupole Transition for Readout and Cooling	8
2.1 Cycling Transitions	9
2.1.1 Computing Cycling Rate to Raman Rate Ratios	10
2.1.2 $p_{3/2}$ Cycling Transition	11
2.1.3 Quadrupole Rabi Frequency	14
2.1.4 $d_{5/2}$ Cycling Transition	17
2.2 Measurement Fidelity	19
2.3 Cross-talk Between Atoms	21
2.3.1 Reabsorption of Scattered Light by Neighboring Atoms in a Lattice	21
2.3.2 Stark Shifting the Cycling Transition	23
2.3.3 Excited State Mixing Due to Stark Shift	24
2.4 Cooling with the $5d_{5/2}$ Quadrupole Transition	26
2.4.1 Optical Molasses Using the Quadrupole Transition	27
2.4.2 PGC on the Quadrupole Transition	28
3 Experimental Progress Towards Cooling and Readout with $5d_{5/2}$ Quadrupole Line	31
3.1 685 nm Laser	31
3.2 Spectroscopy and Cooling on the Quadrupole Line	34

	Page
4 Compensation of Trap Induced Differential Stark Shifts	37
4.1 The Hyperpolarizability and the Interaction of the Magnetic Field and Trapping Light	38
4.2 Magic Trapping for Monochromatic Light Fields	41
4.2.1 Calculating the Differential Stark Shift by Diagonalization of the Full Hamiltonian	41
4.2.2 Calculating Differential Stark Shifts Via An Effective Ground State Hamiltonian	44
4.2.3 Computing Polarizabilities and Other Terms in the Effective Hamiltonian	47
4.2.4 Conditions for Magic Trapping in Monochromatic Fields	50
4.3 Compensation of Differential Stark Shifts by Addition of a Sideband to Trapping Light	52
4.3.1 The Full Hamiltonian for Bichromatic Trapping Light	53
4.3.2 The Effective Hamiltonian for Bichromatic Trapping Light	55
4.3.3 Double Magic Conditions for Bichromatic Traps	56
5 Dissipative Entanglement with Rydberg Atoms	58
5.1 Singlet State Creation Through Dissipative Entanglement	59
5.2 Simulating the Ising Model	65
5.2.1 Ising Model Without a Magnetic Field	65
5.2.2 Antiferromagnetic Ising Model With a Transverse Magnetic Field	68
5.2.3 Frustrated Ising System	70
5.3 Other Potential Applications	71
5.3.1 One-Way Quantum Computing	72
5.3.2 The Spin Glass	72
5.3.3 Simulating the Heisenberg Model	73
6 Conclusion	76
LIST OF REFERENCES	78
APPENDICES	
Appendix A: Stark Shift Laser	86
Appendix B: 459 nm Single Site Repumper Laser	88
Appendix C: Numerical Values of Matrix Elements Used to Calculate Magic Trap Parameters	90

DISCARD THIS PAGE

LIST OF TABLES

Table	Page
4.1 Intensity magic trap conditions for various wavelengths, light polarizations, pairs of states, and magnetic fields. Also reported are the first order sensitivities to the magnetic field, and the second order sensitivities to the reduced Rabi frequency. The polarization is either σ_+ or σ_- and the states column lists $m_{F=4}, m_{F=3}$. Finally, trap depth for blue detuned traps refers to the light shift the atom experiences at the bottom of the trap rather than the actual depth of the trap. The ground state scalar polarizability is negative for the 780 and 820 nm cases so the trap depths are positive, i.e. repulsive potentials.	51
4.2 Doubly magic conditions for red and blue detuned traps for different wavelengths, pairs of states, sideband strengths (ratio of sideband field amplitude to carrier field amplitude), sideband frequency, and the residual sensitivities to field fluctuations. . .	57
5.1 Populations of the 8 possible ground states in a steady state configuration with all laser fields on and then the populations after turning laser fields off and allowing excited states to relax for $20\pi/\gamma$	71
C.1 Some hyperfine constants of Cs. Values from [45] except for a) Ref. [17], b) Ref. [95], c) Ref. [94]	91
C.2 Reduced matrix elements of coupled states $ nlsj\rangle$ in the j basis $\langle n'l'sj' r 6p_{1/2} \rangle$ for the Cs $6p_{1/2}$ state and transition vacuum wavelengths. Cwf are values calculated using Coulomb wavefunctions with experimental values for quantum defects, and r_{\min} a small r cutoff to avoid divergence. WKB are values calculated using the theory of [92]. Matrix elements are given in atomic units. a) From [41] with the sign from Cwf calculation.	92

Table	Page
C.3 Reduced matrix elements of coupled states $ nlsj\rangle$ in the j basis $\langle n'l'sj' r 6p_{3/2} \rangle$ for the Cs $6p_{3/2}$ state and transition vacuum wavelengths. Cwf are values calculated using Coulomb wavefunctions with experimental values for quantum defects, and r_{\min} a small r cutoff to avoid divergence. WKB are values calculated using the theory of [92]. Matrix elements are given in atomic units. a) From [41] with the sign from Cwf calculation.	93
C.4 Reduced matrix elements of coupled states $ nlsj\rangle$ in the j basis $\langle n'l'sj' r 7p_{1/2} \rangle$ for the Cs $7p_{1/2}$ state and transition vacuum wavelengths. Cwf are values calculated using Coulomb wavefunctions with experimental values for quantum defects, and r_{\min} a small r cutoff to avoid divergence. WKB are values calculated using the theory of [92]. Matrix elements are given in atomic units. a) From [41] with the sign from Cwf calculation.	94
C.5 Reduced matrix elements of coupled states $ nlsj\rangle$ in the j basis $\langle n'l'sj' r 7p_{3/2} \rangle$ for the Cs $7p_{3/2}$ state and transition vacuum wavelengths. Cwf are values calculated using Coulomb wavefunctions with experimental values for quantum defects, and r_{\min} a small r cutoff to avoid divergence. WKB are values calculated using the theory of [92]. Matrix elements are given in atomic units. a) From [41] with the sign from Cwf calculation.	95

DISCARD THIS PAGE

LIST OF FIGURES

Figure	Page
1.1 To the left is an illustration of the hexagonal glass cell within which we trap up to 49 atoms in a blue detuned array. The many lasers needed for the AQuA experiment are shown with their intended purpose. On the right is the energy level diagram of neutral cesium and how the transitions each wavelength is meant to drive.	5
2.1 Level structure of lines relevant to cycling transition in alkali atoms. Cycling occurs when atom is excited to $ p_{3/2}, F' = f_+ + 1, m' = F'\rangle$ for dipole transitions and $ d_{5/2}, F' = f_+ + 2, m' = F'\rangle$ for quadrupole transitions. Otherwise there exists potential for atom to spontaneously decay to $F = f_-$ and therefore go dark to our readout laser. Due to the combination of two sources of angular momentum (see text for details), we analyze quadrupole case assuming $m' = f' + 1$ as shown in the figure.	11
2.2 Fraction of the ratio of cycling to Raman rate at resonance as a function of the number of linewidths from resonance assuming $\gamma/\Delta_{hfs} \ll 1$	13
2.3 (a) Log error of state detection by resonance fluorescence for the cesium $6p_{3/2} \leftrightarrow 6s_{1/2}$ cycle with background dominated by scattered light from the readout laser. Parameters used were $\Omega_d/4\pi = 0.067$, $\Delta/\Gamma = 0$, $I/I_s \gg 1$, $\gamma = 2\pi \times 5.23$ MHz and $\eta = 0.6$. (b) Log error of state detection by resonance fluorescence for different background count rates on the cesium $5d_{5/2}$ cycling transition; blue is $10^4/s$, red is $10^3/s$, gold is $10^2/s$. The optimum threshold value depends on the time probed with each scallop increasing the threshold by one, starting with $n_c = 1$ in the leftmost scallop. Parameters used were $\Omega_d/4\pi = 0.067$, $\Delta/\Gamma = 0$, $I/I_s \gg 1$, $\gamma = 2\pi \times .130$ kHz and $\eta = 0.6$	20
2.4 The figure of merit defined in the text for wavelengths near the (a) $6p$ levels, at 852 nm and 894 nm, and (b) $7p$, at 457 nm and 459 nm line in cesium.	25
2.5 Plot of the capture distance as a function of detuning for $s = .25$, $v_i = .16$ m/s. With a beam waist of 1 mm it looks feasible to trap an atom.	27

Figure	Page
2.6 (a) Plot of the typical Doppler cooling using 685 nm that also comes out of the analysis. The peaks in the force are roughly the capture velocity. (b) A zoomed in curve that shows the approximate velocities captured by PGC. Parameters used were $\Omega = .5\gamma$, $\Delta = \gamma$, $\gamma = 2\pi \times 1.24$ kHz.	28
3.1 Allan Deviation of laser output frequency compared to a reference of the high finesse cavity.	32
3.2 High level schematic of final 685 nm laser system.	33
3.3 Doppler absorption signal (blue) and MOT depletion signal (red).	34
3.4 Fluorescence signal from a MOT that was further cooled by PGC before applying 685 nm and repumper light for 1 ms.	35
3.5 Atom cloud immediately after 25 ms of 685 nm light and 4 ms of PGC. This contrasts with no atom cloud without 685. effective power on the atoms was 200 mW with 3 mm diameter beams.	35
4.1 (a) Leading order Stark shift and fourth order Stark shift contribute to differential Stark shift of ground states with different signs. (b) Schematic representation of three of the terms important to calculating the differential shift. Here V is the second order electric dipole polarizability, ω_q is the frequency splitting of the two computational states, Ξ is the magnetic dipole coupling from a static magnetic field and finally V_{HF} is the hyperfine mixing interaction. From left to right we have the cross-term of two electric dipole coupling and a magnetic dipole coupling. This can also happen in reverse order thus the extra factor of two. Next is the fourth order term. This is also the important term for the bichromatic scheme except that it couples to the other ground state that is dressed by a sideband energy very close to the qubit splitting. Then, we have the dominant hyperfine mediated polarizability term which is diagonal in the HFI. Lastly, we have the other important third order term which involves hyperfine-induced mixing of an excited s state and the ground s states.	39
4.2 Differential light shift (DLS) as a function of trapping light intensity and magnetic field. (a) DLS at $B = 0$ using 2nd order perturbation theory (red) and 4th order (blue) for the Cs clock states $ 3, 0\rangle, 4, 0\rangle$ at $\lambda = 1038$ nm. Notice the minimum in the differential shift as a function of the light intensity (trap depth) which constitutes a magic operating point. (b) DLS as a function of the magnetic field with (blue) and without (red) the third order cross-term for $\lambda = 1038$ nm, $\Omega_0/2\pi = 100$ GHz, σ_+ polarization, and the states $ 4, 1\rangle, 3, -1\rangle$	41

Figure	Page
4.3 Schematic of the couplings contributing to the fourth order term important responsible for the efficacy of a bichromatic optical trap. Each atomic state has three dressed states split by ω_s and labeled on the right by photon field numbers m, n . The sign of the sideband frequency ω_s determines which two of the diagrams contributes most. Ω_s is the electric dipole coupling matrix element for the sideband.	54
5.1 Overview of standard optical pumping procedure to produce atoms in the computation basis states. A π polarized optical pumping laser connects the $F = 4$ ground state to the excited state except for the $m_F = 0$ projection. A repumper laser connects $F = 3$ to the excited state. After many spontaneous emissions the atom will end up in the "dark" state $ 2\rangle = F = 4, m_F = 0\rangle$ where it is unaffected by either laser. Ground state rotations via microwaves or optical Raman transitions can prepare then prepare $ 1\rangle = F = 3, m_F = 0\rangle$	60
5.2 Representation of pumping process that creates a singlet or Bell state. $ 1\rangle$ is coupled to $ 3\rangle$ via Ω_1 and $ 2\rangle$ is coupled to $ 4\rangle$ via Ω_2 . $\Delta = V_{44}/2$ to make the two photon excitation resonant and V_{44} is much different than V_{34} . Finally, Ω_g is a ground state rotation to ensure pumping out of triplet state. Spontaneous emission at a rate γ from Rydberg levels eventually drives two atom state into $ 12\rangle - 21\rangle$, i.e. the singlet or Bell state.	61
5.3 Comparison of P_{AF} from Eq. (5.2) (solid line) with singlet state fidelity F_{Bell} from numerical solution of Eq. (5.3) (red dots). Parameters: $\Omega/2\pi = 0.01$ MHz, $\gamma = 1/(0.73 \text{ ms})$, $\Delta_{34}/\Delta_{33} = 0.2$, $\Omega_R = 2\Omega^2/\Delta_{33}$, and $\Omega_g = 0.5\Omega_R$. The atomic parameters correspond to the Cs $125p_{1/2}$ state with $ 3\rangle, 4\rangle$ $m_j = \pm 1/2$ and the quantization axis perpendicular to the line containing the atoms. The inset shows the time dependence for $\Delta_{33}/2\pi = 1$ MHz.	64
5.4 Population of AF_{\pm} states from Monte-Carlo simulations of Eq. 5.3 on a square plaquette and averaged over 100 trajectories. The blue and red curves give the populations of $ 1212\rangle$ and $ 2121\rangle$. Numerical parameters were $\Omega/2\pi = 0.01$ MHz, $\gamma = 1/(0.3 \text{ ms})$, $\Delta_{33}/2\pi = 0.4$ MHz, $\Delta_{34}/\Delta_{33} = 0.85$, $\Delta = \Delta_{33}/2$, $\Omega_R = 2\Omega^2/\Delta_{33}$, and $\Omega_g = 0$. The coupling strengths between opposite corners were $\Delta'_{33} = \Delta_{33}/8$ and $\Delta'_{34} = \Delta_{34}/8$	67
5.5 The total population in states $ 1212\rangle$ and $ 2121\rangle$ as a function of B/J from numerical diagonalization of Eq. 5.6 (solid blue line) and from Monte-Carlo simulations of Eq. 5.3 (red dots).	69

Figure	Page
5.6 The simplest case of frustrated magnetism. Here three spins interact with the same coupling strength. With antiferromagnetic coupling, which spin state should the third spin be to minimize the energy of the system?	70
5.7 Schematic for mapping $ -\rangle_X \rightarrow 3\rangle$ and $ +\rangle_X \rightarrow 4\rangle$ and creating the V_X Hamiltonian. In the left figure notice the relative sign difference between the two coupling lasers that picks out $ -\rangle_X$	74
A.1 Layout of the 918 nm Stark shifting laser used to reduce cross-talk during readout. . .	86
B.1 Layout of the single site 459 nm repumper laser.	88

Chapter 1

Neutral Atom Quantum Computing and AQuA

My goal in writing this thesis is to document my small contributions to a much larger project that goes by Atomic Qubit Array (AQuA), a name surpassed in its banality only by the Very Large Array radio observatory. AQuA blithely takes sides in the ongoing debate over whether we should refer to quantum bits as *qubits* or *qbts* in the lofty pursuit of a catchy acronym.

It's also a quantum computer. A potentially really big one with the capability to load up to 49 qubits and manipulate them in such a way as to run a quantum computation. Building such an enormously complex system requires the talents of many smart physicists and a synthesis of a broad array of engineering and atomic physics techniques.

This chapter will then be an attempt to layout the general structure of a quantum computer and the AQuA quantum computer specifically. Following this will be a discussion of certain obstacles that impede good operation of a quantum computer. The impediments highlighted are chosen with an eye towards our research into triumphing over said obstacles or at least shoving them into a dark corner to be ignored while other sources of error are brought down to the same level.

With those preliminaries out of the way, the next chapter will focus on a novel method for readout and cooling of qubits via the $6s_{1/2} \rightarrow 5d_{5/2}$ quadrupole transition in cesium. At this point we will tackle decoherence due to field instabilities by exploring magic trapping conditions. Finally, we detail a method that takes a significant source of decoherence, spontaneous emissions from a Rydberg state, and bends it toward our will to entangle two atoms and further extend the idea towards simulating quantum Hamiltonians.

1.1 The Quantum Computer

Contrary to the opinions of many lay observers, a computer is not quantum if it is really small. Nor does the size play any part in the potential speed of a quantum computer. By the size metric most classical computers are quantum, being both smaller than most quantum computing experiments and far faster.

No, what makes a computer quantum is that it uses the weirdness of quantum mechanics. Classical computers, as they proceed to smaller and smaller feature sizes on a transistor device, are continually encountering quantum phenomenon. However, they do not exploit the power of quantum mechanics for computation, instead it is usually seen as an engineering problem to be overcome. However, we know that a computer that fully harnesses quantum mechanics is more powerful than a classical computer for a simple reason. Classical computers can't efficiently simulate quantum mechanics and yet nature is "performing" quantum calculations all the time. Thus quantum computers are really an attempt to use nature's higher computational power to efficiently solve problems.

The two most famous algorithms that demonstrate that a quantum computer is superior to a classical computer for some problems are Shor's Algorithm [1] and the Grover Search Algorithm [2]. The former performs a prime factorization of a large number, which may sound boring but multiplying large primes together is the basis of public key cryptography which governs many transactions on the Internet for instance. The latter is, well, a search algorithm. In both cases, classical computers can also solve the problem, but the scaling with problem size is much better on a quantum computer. For instance, Shor's algorithm is exponentially faster than the fastest known classical algorithm, the general number field sieve, which runs in $\approx \text{Exp}[n^{1/3}]$ where n is the number of bits in the input, compared to Shor's which is limited by the speed of modular exponentiation $O(n^3)$ [3].

What exactly gives quantum mechanics its computing power is still widely discussed. Two things are obviously crucial: superpositions, the ability of a quantum object to be in multiple states simultaneously, and entanglement, when the quantum state of one object is inextricable from the

quantum state of another object. One commonality usually present to all quantum algorithms is an initialization of the input quantum state as a superposition of all possible states. It's as if a quantum computer can test all possibilities simultaneously. This weirdness is particularly well illustrated by a quantum algorithm that can tell you what is in a quantum register without actually checking all the data in that register [4]. This would be like pulling out some of the socks from a sock drawer and being able to tell what color all of the socks in the drawer are.

1.2 AQuA

The ingredients for a quantum computer are relatively simple in concept if technically hard to acquire in reality. DiVincenzo identified five criteria for a functional quantum computer [5]:

1. Well-defined qubits
2. Reliable initialization of qubit states
3. Ability to complete operations before decoherence becomes significant
4. An accurate universal set of quantum gates
5. Unambiguous qubit state measurement

First, one needs a set of quantum states. Usually in analogy with a classical computer one chooses qubits where two quantum states are chosen as $|0\rangle$ and $|1\rangle$ in a physical system and then multiple copies of these systems are strung together for more complicated computations. However, one could imagine using qutrits with three quantum states or qudits for an arbitrary dimension of quantum states. In practice, qubits are usually far easier to work with.

In the AQuA experiment we have chosen to use qubits and the quantum states for this purpose are in the ground state hyperfine manifold of neutral cesium. More specifically, $|0\rangle = |6s_{1/2}, F = 3, m_F = 0\rangle$ and $|1\rangle = |6s_{1/2}, F = 4, m_F = 0\rangle$. After we load the atoms in a Magneto-Optical Trap (MOT) and engage in some Polarization Gradient Cooling (PGC) we trap the atoms in a square array of 780 nm Gaussian beams. These beams are blue detuned, higher in frequency

than the atomic transition, from the nearby $6s \rightarrow 6p$ transition and are thus repulsive to atoms in the ground state. Thus, atoms are trapped in the interstices of the foci of the beams. There are potentially 49 such locations in our array, though our loading rate averages about 50% across the entire array. Then we proceed with the above optical pumping procedure.

Now there are a multitude of other states in cesium and so we require a process that initializes our atoms in one of these two states. This optical pumping process is described in detail in Ch. 5 on Dissipative Rydberg Entanglement. Succinctly, we utilize the fact that $|1\rangle$ is uncoupled to the excited state $|6p_{1/2}, F = 4, m_F = 0\rangle$ by π polarized light to pump all the atoms into this dark state, $|1\rangle$.

That takes care of the first two criteria. In order to combat decoherence we cool and trap cesium atoms as described earlier. Our magnetic and laser fields are not spatially homogeneous and thus a colder atom that moves more slowly experiences a more uniform interaction during a computational gate. Similarly, we strive to apply gates as fast as possible to minimize errors from field noise and excited state decay. Using a blue trap ensures that Stark shifts are minimized as the atom resides at a minimum of the trapping light intensity in contrast to a red detuned trap. In these ways we limit attempt to limit the effects of decoherence.

The fourth criteria specifies a universal set of quantum gates. There are many such sets, but if we assume qubits then the simplest description is the set of all single qubit gates, that is the ability to makes any superposition state of $|0\rangle$ and $|1\rangle$, and a gate that couples two qubits, usually taken to be a CNOT gate.

For the set of single qubit gates we use microwave pulses tuned to the frequency difference of our two states, approximately 9.192631770 GHz. Alternatively, we apply a Raman optical rotation whereby two lasers that differ in frequency by the frequency splitting of our qubit are detuned slightly from the $7p$ level, 459 nm in cesium. By controlling the phase difference of these two lasers we can apply various single qubit gates.

Our CNOT gate relies on the Rydberg blockade phenomena [6] and was first demonstrated in Rubidium by earlier scientists in this very lab [7]. The idea is that one atom in a Rydberg state, a state with high principal quantum number n , perturbs the energy levels of Rydberg states of nearby

atoms. That is our ability to excite an atom to a Rydberg state depends on whether a nearby atom is or is not in a Rydberg state. This all the interaction we need for a two qubit gate. Excitation to the Rydberg state is done via a two photon process with the $7p$ level providing the intermediate step up to the Rydberg level.

Lastly, one must be able to readout the quantum state of all the qubits in the computer in order to get the results of an algorithm. This may sound trivial but as we will show later it comes with many complications. Currently we do this by shining 852 nm light that is resonant to the $|6s_{1/2}, F = 4\rangle \rightarrow |6p_{3/2}\rangle$ transition to blow away all atoms currently in $|1\rangle$. Then we keep this laser on along with a repumper resonant with $|6s_{1/2}, F = 3\rangle \rightarrow |6p_{3/2}\rangle$ and look at the scattered 852 nm light to determine if an atom is in $|0\rangle$. If we wish to measure the population in $|1\rangle$ we first use our single qubit gates to transfer the population down to $|0\rangle$ and proceed as before.

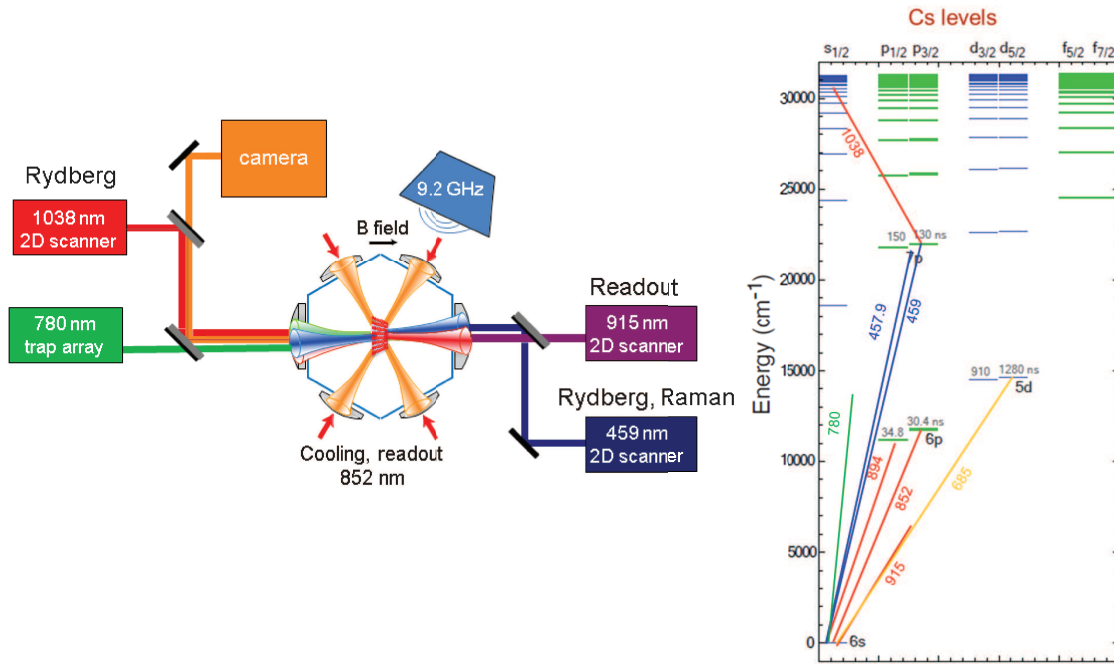


Figure 1.1 To the left is an illustration of the hexagonal glass cell within which we trap up to 49 atoms in a blue detuned array. The many lasers needed for the AQUA experiment are shown with their intended purpose. On the right is the energy level diagram of neutral cesium and how the transitions each wavelength is meant to drive.

1.3 When Quantum Computers Meet Reality

The above discussion ignores many of the harsh realities of quantum computing that makes even the simplest tasks fraught with error. The first two criteria are already well satisfied by our choice of quantum states for $|0\rangle$ and $|1\rangle$ and our scheme for optically pumping into those states. The third is always a struggle and will likely continue to be problematic for some time. Quantum states are fickle things easily perturbed by anything in the environment. In the lab, we often apply static magnetic fields, usually to break the degeneracy of quantum states, and of course multifarious lasers that bathe our qubits in A.C. electric fields for the purposes of cooling, trapping and performing gate operations. These fields cause shifts in the energy difference between our two computational basis state $|0\rangle$ and $|1\rangle$. All of our gate operations depend very precisely on this frequency difference. Static shifts can be accounted for, but the random fluctuations due to field noise or our qubit moving around in an optical trap sampling different fields reduce the fidelity of our gates. Chapter 4 in this thesis will cover an attempt to reduce the sensitivity to such fluctuations by constructing magic traps where the first derivative with respect to changes in static magnetic fields or A.C. electric fields vanish. In Ch. 2 we introduce cooling on the 685 nm quadrupole transition to the $5d_{5/2}$ excited state in cesium which could potentially cool our qubits to much lower temperatures than currently achieved. Colder atoms experience fewer unwanted phase shifts and allow for higher fidelity gate operations.

As discussed before, the fourth criterion, a universal set of gates, requires a two qubit gate like a CNOT and a set of one qubit gates. Single qubit rotations are fairly standard at this point, reaching something like 99% fidelity in AQuA. In contrast, two qubit gates are still a challenge. Excitation to a Rydberg state and leaving it there for some amount of time before returning it to the ground state is a nontrivial task. The feature that gives Rydberg atoms their usefulness as a means of coupling two atoms together is also their weakness as it now couples to the environment more readily than the relatively inert ground states. To address this we devote a chapter to an entanglement scheme that uses dissipation from Rydberg states and in doing so reduces some of the sensitivity to decoherence that can plague the usual coherent Rydberg gate.

Lastly, we come to the question of unambiguously identifying our qubit's state. The aforementioned readout scheme certainly fulfills this criterion, but if we again turn to the $5d_{5/2}$ quadrupole transition we can potentially read out faster and with lower error. This transition has the further benefit of perhaps allowing us to keep the atom in our trap thus obviating the need to reload the trap. In addition, it opens up possibilities for reducing cross talk between qubits during measurement.

This thesis then represents a multi-pronged assault with the objective to help AQUA fulfill the DiVincenzo criteria more ably.

Chapter 2

Theory of the Cs $5d_{5/2}$ Quadrupole Transition for Readout and Cooling

Reading out the computational state of a qubit is a crucial operation to build a working quantum computer. Lossless detection of single atoms has been demonstrated by a few groups [8, 9] on a closed or almost closed transition, but requires very low background levels of photons at the detection wavelength. The idea is to use a cycling transition between the $|F = 4, m_F = 4\rangle \rightarrow |F' = 5, m_{F'} = 5\rangle$ excited with σ_+ polarized light. In the ideal case of perfect polarization there is no possibility of the atom ever decaying to the other ground state $F = 3$ since the atom is exclusively excited to $F' = 5$ which must decay to $F = 4$ due to the dipole selection rules. In practice the polarization is not perfect; there is some possibility of a Raman scattering event to the other ground state at which point it no longer scatters light. If it does this early enough we will erroneously assume that it did not start in the $F = 4, m_F = 0$ ground state.

An alternative is to detect on a different wavelength than you excite as used in rubidium [10] or in ionic calcium [11]. The $|6s_{1/2}\rangle \rightarrow |5d_{5/2}\rangle$ quadrupole transition in neutral cesium due its very narrow linewidth, $\gamma/2\pi = .13$ MHz, and relatively large hyperfine splittings has a much reduced chance of a Raman scattering event. It also has the relevant feature that the excitation light is 685 nm but it decays primarily via a two photon decay that emits a photon at 852 nm. Thus detection of photons at 852 nm should have much lower background counts since the only 852 nm light in the chamber is that scattered from our qubits. This should provide an improvement in our single atom signal to noise ratio and a consequent improvement in measurement fidelity.

With the reduction in background counts, fewer photons must be detected in order to accurately determine the state of the atoms. This opens up the possibility of non-demolition measurements

where the atom is not heated out of the optical trap and we can therefore avoid reloading the atom from a MOT. Lastly, this has potential to reduce the chance that a scattered photon is absorbed by a neighboring qubit destroying any information contained in that qubit. We also attempt to combat cross-talk by site selective Stark shifting of the detection transition between $|6s_{1/2}\rangle \rightarrow |6p_{3/2}\rangle$. In this way any scattered readout photons are now detuned from the same transition in nearby qubits.

The chapter opens with a quantification of the Raman rates for the current dipole transition compared to that of the quadrupole transition. Following this we discuss the error rates and threshold photon numbers for identifying the qubit state in both schemes. Finally we determine an appropriate wavelength for site selective Stark shifting to reduce our cross-talk between qubits.

2.1 Cycling Transitions

Readout is currently done via the transition $|6s_{1/2}, F = 4\rangle \rightarrow |6p_{3/2}, F' = 5\rangle$. State dependent measurements are accomplished by blowing away one of the computational states $|0\rangle$ or $|1\rangle$ by rotating one state into $|1\rangle$ and then heating atoms in that state out of the optical trap. Then the same transition and a repumper allow us to detect enough photons to determine unambiguously which atoms are still around. Keeping track of the ground state rotation between $|0\rangle$ and $|1\rangle$ tells us which state we had.

In contrast, a cycling transition like $|F = 4, m_F = 4\rangle \rightarrow |F' = 5, m_{F'} = 5\rangle$ is a simpler affair. Assuming you know an atom is loaded and that you can retain an atom for an experiment, you just turn it on and if enough photons are detected then it is in $|1\rangle$, otherwise it is in $|0\rangle$. No repumper or microwave rotations are required. The success of such a scheme is dependent on a lack of Raman scattering events that put the atom in the ground state $F = 3$ since there is no longer a repumper.

In the following we calculate the number of photons cycled before a Raman scattering event happens for a randomly polarized laser resonant with $|6s_{1/2}, F = 4\rangle \rightarrow |6p_{3/2}, F' = 5\rangle$. We do this to approximate our current setup where MOT lasers are used for readout and to give a worst case scenario for a dipole transition. After that we attend to a similar calculation for the $|6s_{1/2}, F = 4\rangle \rightarrow |5d_{5/2}, F' = 6\rangle$ quadrupole transition and show that it has superior features in this domain.

2.1.1 Computing Cycling Rate to Raman Rate Ratios

The number of photons which can be scattered before a Raman transition occurs is calculated as follows. We assume an alkali atom with nuclear spin I_n , a $j_g = 1/2$ electronic ground state manifold, hyperfine ground states $f_+ = I_n + j_g$, $f_- = I_n - j_g$ and a cycling transition between $f_+ \leftrightarrow f_e = f_+ + \kappa$, where $\kappa = 1, 2$ for dipole and quadrupole transitions, respectively. If the atoms are illuminated by light of all polarizations and are evenly distributed among Zeeman levels, then the scattering rate for any transition is given by

$$r = \frac{\gamma}{2} \frac{I/I_{s,eff}}{1 + 4\Delta^2/\gamma^2 + I/I_{s,eff}}, \quad (2.1)$$

where $I/I_{s,eff}$ is the saturation parameter for that transition averaged over the initial states and Δ is the detuning of the probe light from the transition. That is, for the transition $f_+ \rightarrow f_e$,

$$\frac{I}{I_{s,eff}} = \frac{2 \sum_{m_e, m_g, q} |\Omega_{f_+, m_g \rightarrow f_e, m_e}|^2}{\gamma^2 (2\kappa + 1) (2f_+ + 1)} \quad (2.2)$$

$$= \frac{2|\Omega_c|^2 \sum_{m_e, m_g, q} |\Omega_{f_+, m_g \rightarrow f_e, m_e}|^2}{\gamma^2 |\Omega_c|^2 (2\kappa + 1) (2f_+ + 1)} \quad (2.3)$$

$$= \frac{\sum_{m_e, m_g, q} |\Omega_{f_+, m_g \rightarrow f_e, m_e}|^2 (I/I_{s,c})}{|\Omega_c|^2 (2\kappa + 1) (2f_+ + 1)}, \quad (2.4)$$

where we have written it in terms of the cycling Rabi frequency, $\Omega_c = \Omega_{f_g=f_+, m_g=f_+ \rightarrow f_e=f_++\kappa, m_e=f_++\kappa}$, and the saturation intensity for that transition, $I/I_{s,c} = 2|\Omega_c|^2/\gamma^2$, for later convenience.

If we tune to the cycling transition ($\Delta = 0$) with a weak laser ($I/I_{s,eff} \ll 1$) the cycling rate becomes

$$r_c = \frac{\gamma}{2} (I/I_{s,eff}). \quad (2.5)$$

Under the same conditions as above and with hyperfine splitting that is large compared to the line width, then the Raman scattering rate into $F = f_-$ can be written as

$$r_R = \frac{\gamma^3 b}{8\Delta^2} \frac{I}{I_{s,eff}}, \quad (2.6)$$

with b representing the branching ratio for decay to the lower hyperfine level of the ground state and Δ now the hyperfine splitting between the cycling hyperfine level and the relevant transition.

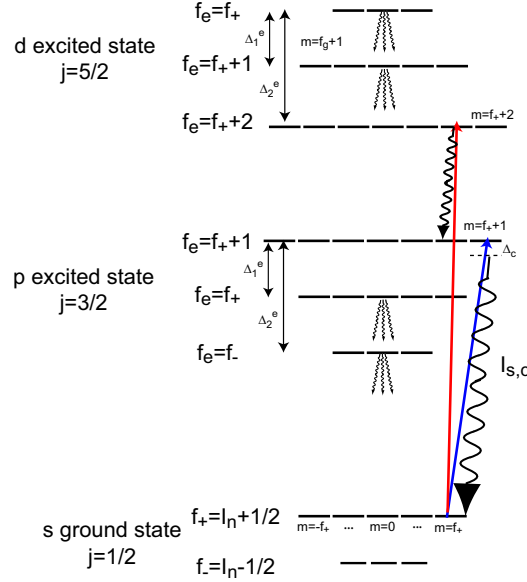


Figure 2.1 Level structure of lines relevant to cycling transition in alkali atoms. Cycling occurs when atom is excited to $|p_{3/2}, F' = f_+ + 1, m' = F'\rangle$ for dipole transitions and $|d_{5/2}, F' = f_+ + 2, m' = F'\rangle$ for quadrupole transitions. Otherwise there exists potential for atom to spontaneously decay to $F = f_-$ and therefore go dark to our readout laser. Due to the combination of two sources of angular momentum (see text for details), we analyze quadrupole case assuming $m' = f' + 1$ as shown in the figure.

We can easily calculate the saturation parameter for the cycling transition

$$\frac{I}{I_{s,eff}} = \frac{\sum_{m_e = -(f_+ + \kappa)}^{f_+ + \kappa} \sum_{m_g = -f_+}^{f_+} \sum_{q = -\kappa}^{\kappa} |C_{f_+, m_g, \kappa, q}^{f_+ + \kappa, m_g + q}|^2}{(2\kappa + 1)(2f_+ + 1)} \frac{I}{I_{s,c}} \quad (2.7)$$

$$= \frac{(2(f_+ + \kappa) + 1)}{(2\kappa + 1)(2f_+ + 1)} \frac{I}{I_{s,c}}. \quad (2.8)$$

The above relations rely on the fact that the double sum over m_g and q is unity.

2.1.2 $p_{3/2}$ Cycling Transition

One possible cycling transition is via the $6p_{3/2}$ level between $f_+ \leftrightarrow f_e = f_+ + 1$ as given by Fig. 2.1. The total Raman scattering rate for transitions $f_+ \rightarrow f_-$ via the excited states $f_e = f_+, f_-$ is

$$r_R = \frac{\gamma^3(I/I_{s,c}) \sum_{m_e} \sum_{m_g} \sum_q}{24(2f_+ + 1)|\Omega_c|^2} \left(\frac{|\Omega_{f_e=f_+, m_e; f_+, m_g}|^2 b_{f_e=f_+}}{\Delta_{f_e=f_+, f_++1}^2} + \frac{|\Omega_{f_e=f_+-1, m_e; f_+, m_g}|^2 b_{f_e=f_+-1}}{\Delta_{f_e=f_+-1, f_e=f_++1}^2} \right), \quad (2.9)$$

with Δ now corresponding to the hyperfine splitting between the two indicated excited states.

The branching ratio is merely the ratio of the strength of the relevant transition over the sum of the transition strengths of all other possible decays from the same level. Once again, these terms are proportional to the Rabi frequency squared and thus made tractable with the Wigner-Eckhart Theorem. For the transition from $6p_{3/2} \rightarrow 6s_{1/2}$ the branching ratio calculation would simplify to

$$b_{f_+ \rightarrow f_+ - 1} = \frac{\gamma_{f_e=f_+ \rightarrow f_g=f_+ - 1}}{\gamma_{f_e=f_+ \rightarrow f_g=f_+} + \gamma_{f_e=f_+ \rightarrow f_g=f_+ - 1}} \quad (2.10)$$

$$= \frac{\begin{Bmatrix} 1/2 & f_+ - 1 & I_n \\ f_+ & 3/2 & 1 \end{Bmatrix}^2}{\left[\frac{(2f_+ + 1)}{(2f_+ - 1)} \begin{Bmatrix} 1/2 & f_+ & I_n \\ f_+ & 3/2 & 1 \end{Bmatrix}^2 + \begin{Bmatrix} 1/2 & f_+ - 1 & I_n \\ f_+ & 3/2 & 1 \end{Bmatrix}^2 \right]} \quad (2.11)$$

$$= \frac{3 + 2I_n}{3 + 6I_n}. \quad (2.12)$$

Other branching ratios are computed in an identical way.

The ratio of the sums over the excitation Rabi frequencies to the cycling Rabi frequency, for a $j_g = 1/2 \rightarrow j_e = 3/2$ transition, are calculated as such

$$\frac{\sum_{m_e=-(f_+)}^{f_+} \sum_{m_g=-f_+}^{f_+} \sum_{q=-1}^1 |\Omega_{f_e=f_+, m_e; f_+, m_g}|^2}{|\Omega_c|^2} \quad (2.13)$$

$$= \frac{\begin{Bmatrix} 3/2 & f_+ & I_n \\ f_+ & 1/2 & 1 \end{Bmatrix}^2}{\begin{Bmatrix} 3/2 & f_+ + 1 & I_n \\ f_+ & 1/2 & 1 \end{Bmatrix}^2} \sum_{m_e} \sum_{m_g} \sum_q |C_{f_+, m_g, 1, q}^{f_+, m_g + q}|^2 \quad (2.14)$$

$$= \frac{4I_n}{3(2I_n + 1)} (2f_+ + 1) \quad (2.15)$$

, with other Rabi frequency ratios again computed similarly.

Placing the values for the branching ratio and excitation Rabi frequencies into the Raman rate equation yields

$$r_R = \frac{\gamma^3(I/I_{s,c})}{18(2f_+ + 1)(2I_n + 1)(3 + 6I_n)} \left[\frac{I_n(2f_+ + 1)(3 + 2I_n)}{\Delta_{f_e=f_+, f_e=f_+ + 1}^2} + \frac{(2I_n - 1)(f_+ - 1)(1 + I_n)}{\Delta_{f_e=f_+ - 1, f_e=f_+ + 1}^2} \right]. \quad (2.16)$$

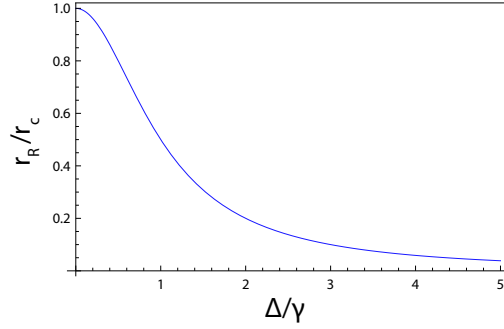


Figure 2.2 Fraction of the ratio of cycling to Raman rate at resonance as a function of the number of linewidths from resonance assuming $\gamma/\Delta_{hfs} \ll 1$

The scattering rate for the cycling transition in this case is

$$r_c = \frac{\gamma(2f_+ + 3)(I/I_{s,c})}{6(2f_+ + 1)}. \quad (2.17)$$

Taking the ratio of these two rates leads to

$$\frac{r_R}{r_c} = \frac{\gamma^2}{9(2f_+ + 3)(2I_n + 1)^2} \left[\frac{I_n(2f_+ + 1)(3 + 2I_n)}{\Delta_{f_e=f_+, f_e=f_++1}^2} + \frac{(2I_n - 1)(f_+ - 1)(1 + I_n)}{\Delta_{f_e=f_+-1, f_e=f_++1}^2} \right]. \quad (2.18)$$

We first compute this ratio for ^{87}Rb ($I_n = 3/2, f_+ = 2$) we find

$$\frac{r_R}{r_c} = \frac{5\gamma^2}{336} \left(\frac{3}{\Delta_{f_e=f_+, f_e=f_++1}^2} + \frac{1}{\Delta_{f_e=f_+-1, f_e=f_++1}^2} \right). \quad (2.19)$$

The linewidth and excited state splittings are (in units of MHz): 6.07, 266.7, 423.6 [12] and

$$\frac{r_c}{r_R} \simeq 38200.$$

Suppose our detection system has efficiency 1% and we wish to count 100 photoelectrons. This requires scattering 10^4 photons so the probing time is $t = 10^4/r_c$. The probability of having made a Raman transition is then

$$P_R = 1 - e^{-r_R t} = 1 - e^{-10^4/38200} = 0.23.$$

It should be noted that this estimate is a best possible case assuming resonant readout. Fig. 2.2 gives the scaling of the readout to Raman ratio as one moves off resonance. For example, if one

detunes by γ the desired scattering rate will go down by a factor of approximately $1/5$. This would then imply

$$P_R = 1 - e^{-r_R t_5} = 1 - e^{-5 \cdot 10^4 / 38200} = 0.73.$$

Thus, almost three-fourths of the time we would expect to suffer a Raman depumping event before completing a measurement.

For ^{133}Cs ($I_n = 7/2, f_+ = 4$) we find

$$\frac{r_R}{r_c} = \frac{7\gamma^2}{704} \left(\frac{5}{\Delta_{f_e=f_+, f_e=f_++1}^2} + \frac{3}{\Delta_{f_e=f_+-1, f_e=f_++1}^2} \right). \quad (2.20)$$

The linewidth and excited state splittings are (in units of MHz): 5.234, 251.1, 452.4 [13] and

$$\frac{r_c}{r_R} \simeq 39100,$$

giving results almost identical to that of rubidium.

However, this calculation assumes random polarization of light. As noted before, the far better method for a dipole transition is to pick a circular polarization that will pump the atom into maximal $|m_F|$. Then the atom can only absorb the probe beam by excitation to the cycling level $f_e = f_+ + 1$, which has only the one decay path to the original ground state. This eliminates all Raman scattering except that due to impurities in the polarization of the probe beam. Unfortunately, our current experimental geometry does not allow us to setup a circularly polarized beam orthogonal to our bias field; instead we settle for reading out with our MOT beams which are circularly polarized, but not all beams propagate orthogonal to bias magnetic field.

2.1.3 Quadrupole Rabi Frequency

The electric quadrupole or $E2$ matrix element is esoteric enough to spend a small amount of time covering its computation. Normally we approximate the oscillating spatial extent of an electromagnetic wave by taking the dipole approximation, that is, $e^{i\mathbf{k}\cdot\mathbf{r}} \approx 1$. For a quadrupole transition we expand out one more term $e^{i\mathbf{k}\cdot\mathbf{r}} \approx 1 + i\mathbf{k}\cdot\mathbf{r}$, where the second term gives the electric quadrupole contribution.

Therefore, evaluation of the quadrupole Rabi frequency relies on computing matrix elements of the scalar operator $(\mathbf{e} \cdot \mathbf{r})(\mathbf{k} \cdot \mathbf{r})$. This is made considerably easier by putting the operator into spherical tensors and grouping the two \mathbf{r} vectors together. Following the method in [14], a compound-tensor scalar operator can be written as, where superscripts in parentheses denote the rank and the subscript refers to the component,

$$[A^{(\kappa)} \otimes B^{(\kappa)}]_0^{(0)} = (-1)^\kappa (2\kappa + 1)^{-1/2} A^{(\kappa)} \cdot B^{(\kappa)}, \quad (2.21)$$

with the dot product now given by $A^{(\kappa)} \cdot B^{(\kappa)} = \sum_q (-1)^q A_q^{(\kappa)} B_{-q}^{(\kappa)}$. A special case of the above for vectors is

$$\mathbf{A} \cdot \mathbf{B} = -3^{1/2} [A^{(1)} \otimes B^{(1)}]_0^{(0)}. \quad (2.22)$$

Utilizing this definition twice

$$(\mathbf{e} \cdot \mathbf{r})(\mathbf{k} \cdot \mathbf{r}) = 3 [[e^{(1)} \otimes r^{(1)}]_0^{(0)} \otimes [k^{(1)} \otimes r^{(1)}]_0^{(0)}]_0^{(0)}. \quad (2.23)$$

We can regroup the operators with the help of angular momentum recoupling rules

$$(\mathbf{e} \cdot \mathbf{r})(\mathbf{k} \cdot \mathbf{r}) = \sum_{\kappa} (2\kappa + 1)^{1/2} [[e^{(1)} \otimes k^{(1)}]^{(\kappa)} \otimes [r^{(1)} \otimes r^{(1)}]^{(\kappa)}]_0^{(0)}. \quad (2.24)$$

The above is merely another compound-tensor scalar operator and thus simplifies to

$$(\mathbf{e} \cdot \mathbf{r})(\mathbf{k} \cdot \mathbf{r}) = \sum_{\kappa} (-1)^\kappa [e^{(1)} \otimes k^{(1)}]^{(\kappa)} \cdot [r^{(1)} \otimes r^{(1)}]^{(\kappa)}. \quad (2.25)$$

However, the dot product of the tensors of rank 0 and 1 are proportional to $(\mathbf{e} \cdot \mathbf{k})$ and $(\mathbf{r} \times \mathbf{r})$, respectively, and both vanish, the former due to the orthogonality condition of light. This leaves the final expression as

$$(\mathbf{e} \cdot \mathbf{r})(\mathbf{k} \cdot \mathbf{r}) = [e^{(1)} \otimes k^{(1)}]^{(2)} \cdot [r^{(1)} \otimes r^{(1)}]^{(2)}. \quad (2.26)$$

The above result is equivalent to that given in [15] as can be shown by writing out the Cartesian components of $[e^{(1)} \otimes k^{(1)}]^{(2)}$ which is equivalent to $\sqrt{3/2} c_{ij}^{(q)} e_i k_j$ in the notation of that paper. The other tensor can be written in terms of the Racah tensors or modified spherical harmonics $C_m^{(\kappa)} = \sqrt{4\pi/(2\kappa + 1)} Y_{\kappa m}$ as such

$$[r^{(1)} \otimes r^{(1)}]_q^{(2)} = r^2 \sqrt{2/3} C_q^{(2)}. \quad (2.27)$$

Combining the above equivalencies recovers the representation given in the reference.

Applying the Wigner-Eckart Theorem to the the representation in terms of the Racah Tensor and then further decoupling the angular momentum

$$\begin{aligned} \langle \alpha' | r^2 C_q^{(2)} | \alpha \rangle &= \sqrt{(2F+1)(2J+1)(2F'+1)(2J'+1)} \sqrt{(2L+1)(2L'+1)} \begin{pmatrix} F' & 2 & F \\ -m_{F'} & q & m_F \end{pmatrix} \\ &\times \begin{pmatrix} L' & 2 & L \\ 0 & 0 & 0 \end{pmatrix} \begin{Bmatrix} J' & F' & I_n \\ F & J & 2 \end{Bmatrix} \begin{Bmatrix} L' & J' & S \\ J & L & 2 \end{Bmatrix} R_{n'L',nL}^2, \end{aligned} \quad (2.28)$$

with $R_{n'L',nL}^2$ the radial matrix element between the two states.

At this point it behooves us to point out a few qualitative features of $E2$ transitions. First, the total angular momentum can change by 2, $|\Delta F| \leq 2$, and similarly $|\Delta m_F| \leq 2$. The expansion of possible angular momentum changes is a consequence of the operator now involving two sources of angular momentum: the polarization of the incoming photon and the angular momentum due to the direction, \mathbf{k} , of the beam. This contrasts with the typical dipole transition where only the relationship of the quantization axis of the atom and the polarization of the photon is relevant and the interaction is otherwise isotropic with respect to the photon direction.

The implications for the cycling transition are massive as it is not possible to engineer a system that solely excites to $|5d_5/2, F' = 6, m_{F'} = 6\rangle$. Such a system would require σ_+ polarization and a beam direction with character similar to σ_+ . Unfortunately, the equivalent would be some sort of laser that rotates around the atom while illuminating it, an unfathomable experimental challenge. Excitation of the cycling transition thus requires something like $\hat{\mathbf{x}}$ -polarized light traveling along the $\hat{\mathbf{y}}$ direction which excites transitions involving $\Delta m_F = -2, 0, 2$, which may be acceptable due to the angular momentum factors favoring $\Delta m_F = 2$.

Now we input beam parameters to give a rough estimate of the Rabi frequency. Specifying that the light is along the z direction with a σ_+ polarization, leaving the tensor product of the polarization and direction with only one component.

$$[e^{(1)} \otimes k^{(1)}]_{-1}^{(2)} = \sqrt{5} \begin{pmatrix} 1 & 1 & 2 \\ 0 & -1 & 1 \end{pmatrix}.$$

That leaves only $q = 1$ in the radial part and inputting an initial state of $\langle 6s_{1/2}, F = 4, m_F = 0 |$ and tuned to $|5d_{5/2}, F' = 6\rangle$ the matrix elements evaluate to

$$\langle i | (\mathbf{e} \cdot \mathbf{r})(\mathbf{k} \cdot \mathbf{r}) | f \rangle = \frac{1}{5} \sqrt{\frac{1}{33}} R_{6s_{1/2}, 5d_{5/2}}^2.$$

Various methods exist for approximating the radial matrix elements, here we take the value as $R_{6s_{1/2}, 5d_{5/2}}^2 = 37.5a_0^2$ for cesium using a Coulomb wavefunction calculation. Taking the quadrupole Rabi frequency as

$$|\Omega/2\pi| = \frac{e|E|}{\hbar\lambda} \langle i | (\mathbf{e} \cdot \mathbf{r})(\mathbf{k} \cdot \mathbf{r}) | f \rangle, \quad (2.29)$$

with a waist of $100 \mu\text{m}$ and an optical power of 1 mW gives a result of 39.7 kHz .

This is a fairly low Rabi frequency compared to that usually seen for the D1 and D2 line in cesium. This follows from the much higher saturation intensity of the transition. Typical saturation intensity for the D2 line is a few mW/cm^2 compared to $\approx 1 \text{ W}/\text{cm}^2$ for the $5d_{5/2}$ line. The three orders of magnitude difference is a result of the extreme weakness of quadrupole transitions, overriding even the narrow linewidth of the transition. This demand for power at an unorthodox wavelength of 685 nm has proven to be a significant barrier for experimental usage of the quadrupole line.

2.1.4 $d_{5/2}$ Cycling Transition

Another possibility for a cycling transition is a quadrupole transition to $d_{5/2}$ (see Fig. 2.1) which harbors the advantage that the probe laser frequency ($s_{1/2} \rightarrow d_{5/2}$) is different than the readout frequency ($p_{3/2} \rightarrow s_{1/2}$). The procedure for determining the rate of cycling versus a Raman transition follows along the same lines as the previous section. Due to the dipole selection rules, calculating the decay branching ratios of the $5d_{5/2}$ hyperfine levels requires determining the branching ratios of the two intermediate steps $d_{5/2} \rightarrow p_{3/2}$ and $p_{3/2} \rightarrow s_{1/2}$. Combining these sets of branching ratios will then give the probability that a hyperfine level, f_e , of $5d_{5/2}$ will decay to the lower hyperfine level, $f_g = f_+ - 1$, of the ground state $6s_{1/2}$ and therefore be “lost.”

Adding the rates for all the Raman transitions gives the rate of leakage to the lower hyperfine level of the ground state. Assuming that the decay rate for all the hyperfine levels is approximately

the same, the Raman rate can be written as

$$r_R = \frac{\gamma^3(I/I_{s,c})}{40(2f_+ + 1)(5 + 10I_n)^2} \left(\frac{8I_n(5 + 2I_n)(2f_+ + 3)}{\Delta_{f_e=f_++1}^2} + \frac{4(2 + I_n)(6I_n - 3)(2f_+ + 1)}{\Delta_{f_e=f_+}^2} \right. \\ \left. + \frac{4(9 + 6I_n)(I_n - 1)(2f_+ - 1)}{\Delta_{f_e=f_+-1}^2} + \frac{8(2I_n - 3)(1 + I_n)(2f_+ - 3)}{\Delta_{f_e=f_+-2}^2} \right). \quad (2.30)$$

The cycling rate for a quadrupole transition with weak laser intensity and zero detuning is

$$r_c = \frac{\gamma}{2}(I/I_{s,eff}) = \frac{\gamma}{10} \frac{(2f_+ + 5)}{(2f_+ + 1)} \frac{I}{I_{s,c}}. \quad (2.31)$$

Finally, the ratio of the Raman rate to the cycling rate, i.e. loss to readout, emerges as

$$\frac{r_R}{r_c} = \frac{\gamma^2}{4(2f_+ + 5)(5 + 10I_n)^2} \left(\frac{8I_n(5 + 2I_n)(2f_+ + 3)}{\Delta_{f_e=f_++1, f_e=f_++2}^2} + \frac{4(2 + I_n)(6I_n - 3)(2f_+ + 1)}{\Delta_{f_e=f_+, f_e=f_++2}^2} \right. \\ \left. + \frac{4(9 + 6I_n)(I_n - 1)(2f_+ - 1)}{\Delta_{f_e=f_+-1, f_e=f_++2}^2} + \frac{8(2I_n - 3)(1 + I_n)(2f_+ - 3)}{\Delta_{f_e=f_+-2, f_e=f_++2}^2} \right). \quad (2.32)$$

Estimates of the hyperfine splitting in the $d_{5/2}$ level can be assayed if given a value for the magnetic dipole constant, also known as the dipolar constant, A . Ignoring the electric quadrupole term, B , which is 10^{-3} smaller, the energy shifts are found from

$$\Delta E = \frac{A}{2}(F(F + 1) - I(I + 1) - J(J + 1)). \quad (2.33)$$

For ^{133}Cs ($I_n = 7/2$, $f_+ = 4$) we find

$$\frac{r_R}{r_c} = \frac{3\gamma^2}{20800} \left(\frac{308}{\Delta_{f_e=f_++1, f_e=f_++2}^2} + \frac{297}{\Delta_{f_e=f_+, f_e=f_++2}^2} \right. \\ \left. + \frac{175}{\Delta_{f_e=f_+-1, f_e=f_++2}^2} + \frac{60}{\Delta_{f_e=f_+-2, f_e=f_++2}^2} \right). \quad (2.34)$$

Taking the $5d_{5/2}$ lifetime as 1226 ns given in [16] and a value of -21.24 MHz for A from [17], the linewidth and the excited state hyperfine splitting are (in MHz): .130, 127.4, 233.6, 318.6, 382.3.

Placing these in the above equation and inverting

$$\frac{r_c}{r_R} \simeq 1.55 \times 10^7,$$

which is far better than a dipole cycling transition.

For ^{87}Rb ($I_n = 3/2$, $f_+ = 2$) on the $4d_{5/2}$ decaying via a 780 nm photon we find

$$\frac{r_R}{r_c} = \frac{\gamma^2}{1200} \left(\frac{56}{\Delta_{f_e=f_++1, f_e=f_++2}^2} + \frac{35}{\Delta_{f_e=f_+, f_e=f_++2}^2} + \frac{9}{\Delta_{f_e=f_+-1, f_e=f_++2}^2} \right). \quad (2.35)$$

From [18], the lifetime of $4d_{5/2}$ is 88.74 ns and from [19], $A = -16.75$ MHz and therefore the linewidth and excited state hyperfine splittings are (in MHz): 1.80, 67.0, 117.3, 156.81. Inputting these into the above yields

$$\frac{r_c}{r_R} \simeq 24100,$$

approximately a third less than the dipole transition and not unexpected given the relatively wide linewidth and narrow hyperfine splitting. That is, rubidium does not share the peculiar characteristics that makes the quadrupole transition attractive for readout in cesium.

2.2 Measurement Fidelity

As already stated, AQuA currently requires a repumper for measuring qubit states as it does not operate on a cycling transition and thus the Raman rate is nontrivial. We must then blow away one of our computational states first in order to make a state selective measurement. With a low enough Raman rate we can dispense with the repumper and blow away procedure. Ideally this would allow us to keep atoms in our trap without a need to reload them from a MOT.

Measurement of the atomic state by resonance fluorescence from a cycling transition relies on setting a threshold of photon scattering events to reach in a given time period. If the number of counts exceeds this threshold it is in state $|1\rangle$ otherwise it is in state $|0\rangle$. Errors occur with this measurement scheme in two ways. First, it is possible that background counts may exceed the threshold while the atom is in $|0\rangle$ and secondly, the atom may be in $|1\rangle$ but erroneously labeled if the combination of photon scattering events and background counts does not exceed the threshold.

Assuming a Poissonian photon rate the probability of an error is

$$E = P(|0\rangle) \sum_{n=n_c}^{\infty} P_n(b) + P(|1\rangle) \sum_{n=0}^{n_c-1} P_n(q) \sum_{m=n}^{n_c-n-1} P_m(b), \quad (2.36)$$

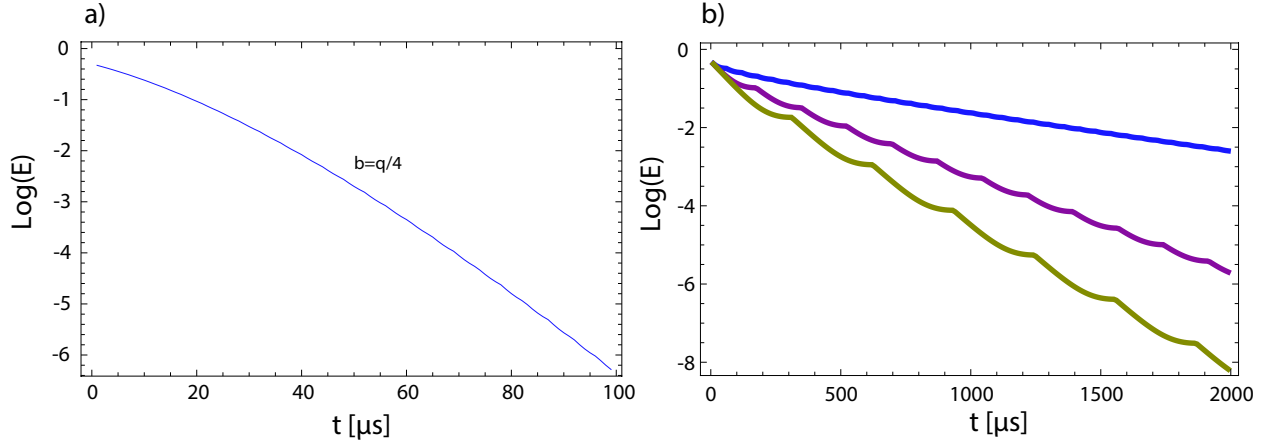


Figure 2.3 (a) Log error of state detection by resonance fluorescence for the cesium $6p_{3/2} \leftrightarrow 6s_{1/2}$ cycle with background dominated by scattered light from the readout laser. Parameters used were $\Omega_d/4\pi = 0.067$, $\Delta/\Gamma = 0$, $I/I_s \gg 1$, $\gamma = 2\pi \times 5.23$ MHz and $\eta = 0.6$. (b) Log error of state detection by resonance fluorescence for different background count rates on the cesium $5d_{5/2}$ cycling transition; blue is $10^4/s$, red is $10^3/s$, gold is $10^2/s$. The optimum threshold value depends on the time probed with each scallop increasing the threshold by one, starting with $n_c = 1$ in the leftmost scallop. Parameters used were $\Omega_d/4\pi = 0.067$, $\Delta/\Gamma = 0$, $I/I_s \gg 1$, $\gamma = 2\pi \times .130$ kHz and $\eta = 0.6$.

where q is the scattering rate, b the background rate and n_c the threshold. The photon count rate is given by

$$q(\tau) = \eta \frac{\Omega_d}{4\pi} \frac{\gamma\tau}{2} \frac{I/I_s}{1 + 4\frac{\Delta^2}{\gamma^2} + I/I_s}, \quad (2.37)$$

where τ is the collection time, Ω_d the solid angle of collection and η the detection efficiency and the background count rate is assumed linear in time. The threshold that minimizes the error depends on the measurement time and the background rate as depicted in Fig. 2.3. This formula differs from [20] in the second term as we now include the fact that background counts actually helps with detecting an atom in state $|1\rangle$. This means actual errors are slightly smaller than those investigated in that prior paper.

We compare the dipole and quadrupole transitions at large saturation parameters and zero detuning. In order to mimic the detection of 852 nm light not scattered by atoms when cycling on the dipole transition we add to the background a factor that scales with the scattering rate. For a dipole transition the error decreases to a marginal level in only $100 \mu s$. In the case of the quadrupole

transition the threshold that minimizes error is well resolved as a scalloped curve such that in practice one should determine the time of measurement and then calculate the appropriate threshold. The low scattering rate of the quadrupole transition requires much longer integration times coupled with a low background rate for operation. However, many fewer photons are scattered which opens up the possibility of reading out the computational state of an atom without heating them out of a trap.

2.3 Cross-talk Between Atoms

A potential problem with any readout scheme is that the atom targeted for readout scatters an exceedingly high number of photons and some of these photons are then reabsorbed by neighboring atoms in the array. Of course, absorption of a photon will eventually lead to spontaneous emission destroying any coherence the atom has with the rest of the qubits. In an effort to avoid this fate we take steps to address this cross-talk by using a Stark shift to bring the scattered photon out of resonance with neighboring atoms.

2.3.1 Reabsorption of Scattered Light by Neighboring Atoms in a Lattice

As already shown in previous sections, the vast majority of the scattered light will correspond to the cycling transition. Thus, assuming isotropic scattering the intensity of the scattered light is given by

$$I_{scattered} = \frac{\hbar\omega r_c}{4\pi a^2}, \quad (2.38)$$

where a is the distance from the atom and the absorption rate by a nearby atom is

$$r_{abs} = \frac{\sigma I_{scattered}}{\hbar\omega}. \quad (2.39)$$

Focusing on cycling via $p_{3/2}$ and again assuming a weak intensity and no detuning, the cycling rate can be written as

$$r_c = \frac{\gamma(2f_+ + 3)(I/I_{s,c})}{6(2f_+ + 1)} = \frac{\lambda^3(2f_+ + 3)I}{2\pi\hbar c(2f_+ + 1)}, \quad (2.40)$$

by utilizing the identity $I_{s,c} = \pi \hbar c \gamma / 3 \lambda^3$. The cross section for scattering of resonant light by an atom prepared in $m_g = 0$ is given by

$$\sigma = \frac{\lambda^2 (2f_+ + 3)}{2\pi (2f_+ + 1)}. \quad (2.41)$$

Combining all of the preceding yields the rate at which a neighboring atom is removed from the $m_g = 0$ state:

$$r_{loss} = \frac{\lambda^5 I}{16\pi^3 \hbar c a^2} \frac{(2f_+ + 3)^2}{(2f_+ + 1)^2}. \quad (2.42)$$

With the quadrupole transition, the only alteration is the cycling rate which is now

$$r_c = \frac{\gamma}{2} (I/I_{s,eff}) = \frac{\gamma}{10} \frac{(2f_+ + 5)}{(2f_+ + 1)} \frac{I}{I_{s,c}}. \quad (2.43)$$

The formula for the loss rate then becomes

$$r_{loss} = \frac{\lambda^2 |\Omega|^2}{40\pi^2 \gamma a^2} \frac{(2f_+ + 5)(2f_+ + 3)}{(2f_+ + 1)^2}, \quad (2.44)$$

with γ and Ω referring to the quadrupole transition and λ is the wavelength of the $6p_{3/2} \rightarrow 6s_{1/2}$ transition since only the second step of the decay is resonant with the nearby atoms sitting in the ground state.

We can ascertain an upper limit on this cross-talk by letting the cycling rate go to $\gamma/2$ at which point the absorption rate for both cycling schemes goes to

$$r_{loss} = \frac{\lambda^2 \gamma f_+ (5f_+ + 8)}{32\pi^2 a^2 (2f_+ + 1)^2}, \quad (2.45)$$

where $\lambda = 852 \text{ nm}$ for cesium and γ is the width of the dipole or quadrupole transition. Thus, in this limit we expect them to be related by the ratio of their linewidths. In our experiment we space atoms approximately $5 \mu\text{m}$ apart and therefore the absorption rate for each scheme is

$$r_{dipole} = 4180 \text{ s}^{-1} \quad (2.46)$$

$$r_{quad} = 104 \text{ s}^{-1}. \quad (2.47)$$

A fairer comparison is to take the results of the last section for how long readout will take in either scenario to see the odds of a cross-talk event. If we want a measurement error of .1% then

the dipole scheme takes $50 \mu\text{s}$ while the quadrupole scheme takes 1 ms giving the probability of cross talk as 21% and 10%, respectively. The slower speed, but lower cross talk of the quadrupole transition is probably preferable at the moment where measurement occurs only at the end of each experiment cycle and alcrity is not as critical.

2.3.2 Stark Shifting the Cycling Transition

Unfortunately, this is an unacceptably high amount of cross-talk in either scenario. To further reduce the chances of altering the state of nearby atoms while reading out, one can A.C. Stark shift the cycling transition so that scattered light is no longer resonant with nearby atoms. There are two potential targets for this shift, the target atom or the rest of the atoms in the array. The latter option has the advantage that these atoms are not transitioning and therefore the state mixing that occurs while perturbed by the A.C. field is largely irrelevant. However, numerous technical difficulties hamper the feasibility of basking all but one atom in light. Thus, we take the former tactic in the following analysis.

Any wavelength of light that couples either $6s_{1/2}$ or $6p_{3/2}$ to another state through the dipole operator is a possibility for Stark shifting, so it behooves one to find a transition that maximizes the Stark shift and minimizes any excited state mixing. For linearly polarized light, the vector term of the irreducible representation of the polarizability of the atom vanishes. Thus, the expression for the energy shifts with fine structure are [21]

$$\Delta W = -\frac{1}{4}\alpha_0|\mathcal{E}|^2 - \frac{1}{4}\alpha_2|\mathcal{E}|^2 \frac{3M_J^2 - J(J+1)}{J(2J-1)}, \quad (2.48)$$

$$\alpha_0 = \frac{2e^2}{3\hbar(2J+1)} \sum_{n' \neq n} \frac{\omega_{n',n}}{\omega_{n'J',nJ}^2 - \omega^2} (h_- + h_0 + h_+), \quad (2.49)$$

$$\alpha_2 = \frac{2e^2}{3\hbar(2J+1)} \sum_{n' \neq n} \frac{\omega_{n',n}}{\omega_{n'J',nJ}^2 - \omega^2} \times \left(h_0 \frac{2J-1}{J+1} - h_- - h_+ \frac{J(2J-1)}{(J+1)(2J+3)} \right), \quad (2.50)$$

where $h_0 = |\langle n'J || r || nJ \rangle|^2$, $h_- = |\langle n'J-1 || r || nJ \rangle|^2$, $h_+ = |\langle n'J+1 || r || nJ \rangle|^2$ and $\omega_{n',n}$ is the difference in energy of the two levels. To work with the hyperfine basis one needs to modify the

term proportional to the tensor polarizability, α_2 , slightly by changing the coefficient

$$\frac{3M_J^2 - J(J+1)}{J(2J-1)} \longrightarrow \frac{[3M_F^2 - F(F+1)][3X(X-1) - 4F(F+1)J(J+1)]}{F(2F-1)(2F+2)(2F+3)J(2J-1)}, \quad (2.51)$$

where $X = F(F+1) + J(J+1) - I(I+1)$.

It is convenient to define the following figure of merit

$$\mathcal{F} = |\alpha_2(6p_{3/2})|/|\alpha_0(6s_{1/2}) - \alpha_0(6p_{3/2})|, \quad (2.52)$$

a parameterization of the ratio of excited state mixing given by α_2 to the scalar shift of the $6s_{1/2} \leftrightarrow 6p_{3/2}$ transition. A glance at Fig. 2.4 and striving for a low \mathcal{F} suggests coupling $6s$ and $6p$, $6s$ and $7p$ or $6p$ and $6d$. The former is on the same frequency as our readout light and is almost identical in energy to $5d_{5/2} \leftrightarrow 8p_{3/2}$ which will induce heavy mixing in our quadrupole cycling level. Ostensibly the second option looks exceptional in terms of its figure of merit and the lack of state mixing. Yet, the figure of merit also discloses that the power requirements to stay far enough away to avoid scattering light while providing the requisite energy shift may be impractical. The last option avoids perturbing the ground state and has a relatively low and flat figure of merit around 910 nm.

Ignoring the first option, with wavelengths of 910 nm and 465 nm chosen it remains only to calculate the beam parameters to enact the required energy shift. A 5γ shift provides a convenient number to target as it will attenuate any cross-talk by a factor of approximately 100. The above requirements necessitate an average beam intensity of $1.49 \cdot 10^9 \text{ W/m}^2$ for 910 nm light and $1.07 \cdot 10^9 \text{ W/m}^2$ at 465 nm.

2.3.3 Excited State Mixing Due to Stark Shift

We have chosen to pursue a Stark shifting laser at a frequency near 910 nm and further analysis will focus on this wavelength. Application of an A.C. electric field will mix states into the cycling transition leading to losses in addition to those due to Raman scattering. If the Stark shift laser is tuned to the $6p$ and $6d$ levels in cesium, then first order perturbation theory only mixes states of the

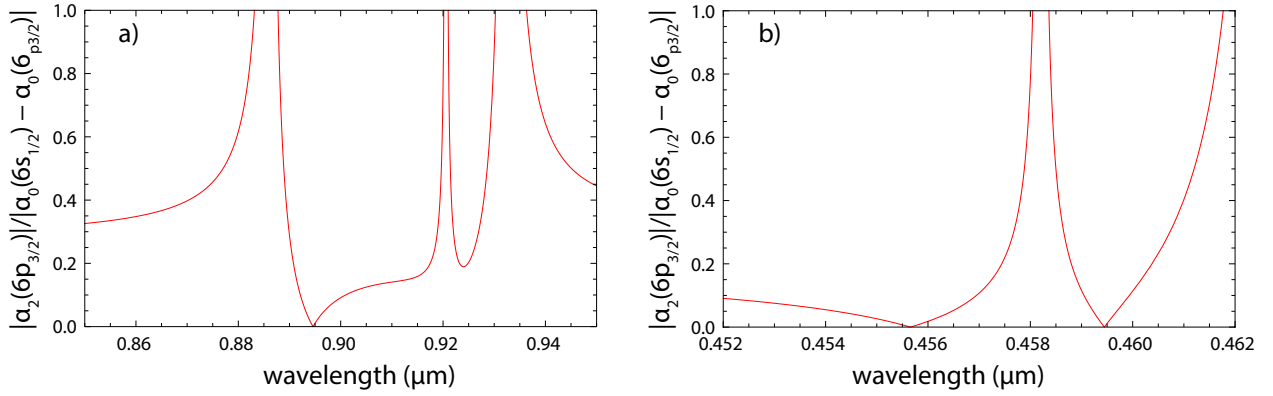


Figure 2.4 The figure of merit defined in the text for wavelengths near the (a) $6p$ levels, at 852 nm and 894 nm, and (b) $7p$, at 457 nm and 459 nm line in cesium.

same parity as the ground state into the $6p$ levels. It is therefore necessary to go to second order where the Stark beam mixes together hyperfine levels of the $6p$ level.

For a constant perturbation, V , the second order correction to the wavefunctions are

$$|n^{(2)}\rangle = \sum_{k,m} |k\rangle \frac{V_{km}V_{mn}}{(E_n - E_k)(E_n - E_m)}, \quad (2.53)$$

where the other terms will either vanish for a dipole transition or be negligible after later considerations. At this point, one can apply Floquet's Theorem to arrive at the amount of $|k\rangle$ mixed into $|n\rangle$ while situated in an A.C. electric field

$$(\beta_k^{(2)})_{ij} = \frac{|\mathcal{E}|^2}{4\hbar^2} \sum_m \left[\frac{(d_i)_{km}(d_j)_{mn}}{\omega_{mn} - \omega} \left(\frac{1}{\omega_{kn}} + \frac{1}{\omega_{kn} - 2\omega} \right) + \frac{(d_j)_{km}(d_i)_{mn}}{\omega_{mn} + \omega} \left(\frac{1}{\omega_{kn} + 2\omega} + \frac{1}{\omega_{kn}} \right) \right]. \quad (2.54)$$

The relevant mixing is confined only to the $6p$ levels, $\omega_{kn} \rightarrow 0$ and only the first and last term are of import. With a little simplification the tensor components are

$$(\beta_k^{(2)})_{ij} = \frac{|\mathcal{E}|^2}{4\hbar^2\omega_{kn}} \sum_m \left[\frac{(d_i)_{km}(d_j)_{mn}}{\omega_{mn} + \omega} + \frac{(d_j)_{km}(d_i)_{mn}}{\omega_{mn} - \omega} \right]. \quad (2.55)$$

With a large enough detuning the hyperfine splitting of the $6d$ levels may be ignored and with π -polarized light the coefficients become

$$(\beta_k^{(2)})_{zz} = \frac{|\mathcal{E}|^2 e^2}{4\hbar^2\omega_{kn}} \sum_m \frac{\omega_{mn} z_{km} z_{mn}}{\omega_{mn}^2 - \omega^2}. \quad (2.56)$$

Measurement on the $6p_{3/2}$ dipole transition by cycling on the $F = 5, m_F = 5$ Zeeman level is negligibly affected if using π -polarized light. Only states of the same magnetic quantum number are mixed together with π -polarized light and $6p_{3/2}$ has no other states with $m_F = 5$. We can also ignore $6s \rightarrow 7p$ mixing because of the large hyperfine splitting of the ground state and the fact that mixing is suppressed for $J = 1/2$ states. Unfortunately, mixing affects a quadrupole measuring scheme as now even when the atom is excited to the highest hyperfine level in $5d_{5/2}$ there is a small chance that the atom will decay to the lower hyperfine level of the ground state. Essentially the branching ratio of $6p_{3/2}, F = 5 \rightarrow 6s_{1/2}, F = 4$ is no longer equal to unity because small amounts of other hyperfine levels are now mixed into it. Thus the cycling rate and Raman rate in the previous sections will be modified. The new cycling to Raman ratio is related to the old one by

$$\left(\frac{r_R}{r_c}\right)_{new} = \frac{r_R + br_c}{(1-b)r_c} = \frac{r_R}{(1-b)r_c} + \frac{b}{(1-b)}. \quad (2.57)$$

Taking the beam intensity as calculated in the last section, $\omega_{6p_{3/2}, 6d_{3/2}} = 2\pi \cdot 325.6 \text{ THz}$, $\omega_{6p_{3/2}, 6d_{5/2}} = 2\pi \cdot 326.8 \text{ THz}$ and $\omega = 2\pi \cdot 329.4 \text{ THz}$ yields $b = 1.86 \cdot 10^{-6}$ which gives a modified ratio of

$$\frac{r_c}{r_R} = 2.472 \cdot 10^4.$$

Further complicating matters, the choice of frequency for ω lies somewhat close to the $5d_{5/2} \rightarrow 8p$ transition (893 nm and 900 nm for $8p_{3/2}$ and $8p_{1/2}$, respectively). This will mix the hyperfine states of $5d_{5/2}$ together and again affect the branching ratio. Repeating the same calculation as above reveals that this is a very small correction, $r_c/r_R = 2.470 \cdot 10^4$.

Yet one more source of mixing appears as now first order perturbation theory will mix $8p$ directly into $5d$ and therefore the state can now decay directly to the ground state. However, the effect is even more diminutive than the above and we will safely ignore it.

2.4 Cooling with the $5d_{5/2}$ Quadrupole Transition

The peculiar characteristics of the cesium $5d_{5/2}$ level also show promise for laser cooling applications. This is a result of its relatively narrow linewidth and the consequently low Doppler cooling limit of approximately $3 \mu\text{K}$ compared to $125 \mu\text{K}$ for the D2, $6p_{3/2}$, line. Narrow line cooling is an

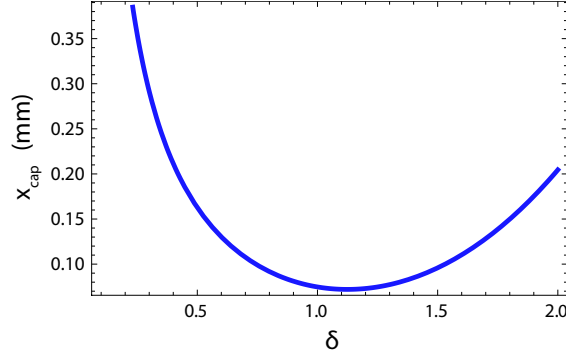


Figure 2.5 Plot of the capture distance as a function of detuning for $s = .25$, $v_i = .16$ m/s. With a beam waist of 1 mm it looks feasible to trap an atom.

increasingly popular topic with demonstrations in species as diverse as Li [22], K [23], Ca [24], Er [25] and Dy [26]. The capture velocity of narrow lines is quite small and thus we expect to use some sort of two stage cooling; starting with a MOT on the D2 line in cesium before cooling on the quadrupole line. Such a scheme as already been employed in strontium [27] at a wavelength, 689 nm, very similar to our own. Here we take a short theoretical analysis of the feasibility and effectiveness of cooling on the quadrupole transition.

2.4.1 Optical Molasses Using the Quadrupole Transition

The simplest analysis is to look at a one dimensional optical molasses. In that case the force equation as a function of velocity for an atom in two counter-propagating beams is

$$F(v) = \hbar k \gamma s / 2 \left(\frac{1}{1 + 4(\frac{\Delta + kv}{\gamma})^2 + s} - \frac{1}{1 + 4(\frac{\Delta - kv}{\gamma})^2 + s} \right), \quad (2.58)$$

where k is the wavenumber, Δ the detuning and s the saturation parameter. With this we can integrate $mv \frac{dv}{dx} = F(v)$ to arrive at the approximate length to stop an atom with initial velocity v_i

$$x_{cap} = \int_{v_i}^0 \frac{-m dv}{8 \hbar k^2 s \delta} \left(\frac{16(kv)^4}{\gamma^4} + \frac{8(kv)^2}{\gamma^2} (1 + s - 4\delta^2) + 8\delta^2 (1 + s + 2\delta^2) + (1 + s)^2 \right), \quad (2.59)$$

where we have swapped variables to $\delta = \Delta/\gamma$. Carrying out the relatively trivial integration yields

$$x_{cap} = \frac{m}{8 \hbar k^2 s \delta} \left(\frac{16k^4 v_i^5}{5\gamma^4} + \frac{8k^2 v_i^3}{3\gamma^2} (1 + s - 4\delta^2) + v_i (8\delta^2 (1 + s + 2\delta^2) + (1 + s)^2) \right). \quad (2.60)$$

In Fig. 2.5 we plot this function with parameters relevant to our current experimental capabilities and assume that we start at the Doppler temperature limit of the D2 line. That is, this is

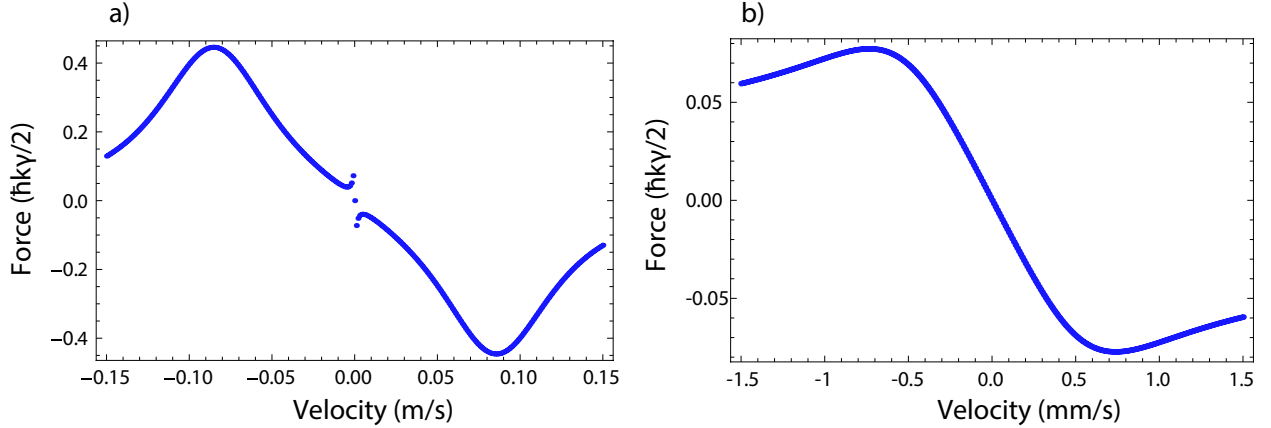


Figure 2.6 (a) Plot of the typical Doppler cooling using 685 nm that also comes out of the analysis. The peaks in the force are roughly the capture velocity. (b) A zoomed in curve that shows the approximate velocities captured by PGC. Parameters used were $\Omega = .5\gamma$, $\Delta = \gamma$, $\gamma = 2\pi \times 1.24 \text{ kHz}$.

only valid if we first cool the atoms before attempting to use the quadrupole transition for further cooling. We in fact already apply Polarization Gradient Cooling (PGC) to cool below this Doppler limit so this analysis is somewhat of a worst case scenario and we would expect to stop atoms even more quickly. However, by optimizing the detuning it appears that by this analysis we could indeed trap and cool atoms on the quadrupole line.

2.4.2 PGC on the Quadrupole Transition

We now move onto a more formal analysis that also investigates the potential for PGC with 685 nm light. In order to conduct this analysis we follow the method pioneered by Dalibard and Cohen-Tannoudji in [28]. We are interested in the case of counter-propagating $\sigma_+ - \sigma_-$ configuration as that is our current method for sub-Doppler cooling.

The physical basis of this method as elucidated in the aforementioned paper is that this configuration creates a spatially varying light polarization. As an atom moves along the beam path it experiences a rotating linear polarization orthogonal to the beam wavevector which is equivalent to an effective magnetic field. As the atom moves in this effective magnetic field the population of its ground states is redistributed based on its velocity. This redistribution is such that it is pumped

into a ground state that, because of angular momentum factors, is more likely to absorb a photon from the circularly polarized light propagating anti-parallel to the atom. A net force then arises that is opposite in sign to that of the atom velocity and thus the atom is cooled.

Our analysis includes all Zeeman levels in $|5d_{5/2}, F = 6\rangle$, $|6p_{3/2}, F = 5\rangle$ and $|6s_{1/2}, F = 4\rangle$ with excitation only to the quadrupole line, but decay through the D2 line. We avoid replicating the tedious details of this calculation as they can be extrapolated, with some effort, from the simplest case explored in [28]. Instead we give only the broad strokes before giving the results.

As we often do in atomic physics, we turn to the optical Bloch equations or Lindblad master equation and write down the perturbation Hamiltonian and the spontaneous emission operators for all states:

$$\frac{d\rho}{dt} = -\frac{i}{\hbar}[\mathcal{H}, \rho] + \mathcal{L}. \quad (2.61)$$

Our perturbation is

$$V = \frac{\hbar}{2} \sum_{m_s, m_d} \Omega_{m_s, m_d} |6s_{1/2}, F = 4, m_s\rangle \langle 5d_{5/2}, F = 6, m_d| + h.c., \quad (2.62)$$

where the sum runs over all the states in the ground state manifold and excited state manifold and we restrict ourselves to $\Delta m = \pm 1$. Lastly, the collapse operators from the d states to the p states and the p states to the s ground states are needed.

The trickiest part is to then make a transformation to a moving rotating frame, that is the frame where the atom is at rest and rotating with the rotating linear polarization the atom experiences as it moves. Mathematically we transform the density matrix elements with the following relationship

$$\tilde{\rho}(d, m_d = m_s \pm 1, s, m_s) = \rho(d, m_d = m_s \pm 1, s, m_s) \exp(i\omega_{\mp} t), \quad (2.63)$$

with $d = 5d_{5/2}, F = 6$, $s = 6s_{1/2}, F = 4$, $\omega_{\mp} = \omega \mp kv$ and ω the frequency of the incident light, k its wavenumber and v the velocity of the atom.

Now we take advantage of the low intensities presumed for PGC and adiabatically eliminate the excited states to put everything in terms of ground state populations and coherences. To do this we write the ground-excited state coherences in terms of ground state populations and coherences

while ignoring any term proportional to the assumed negligible excited state populations and coherences. Substitute these into steady state equations for the excited state populations and coherences and in turn use these results in the equations for the ground state populations and coherences.

At this point we are nearly done as we have a set of equations written entirely in terms of ground state populations and coherences. Setting their time derivative to zero to get the steady state solution will allow us to find explicit values for these elements of the density matrix which we can then use to determine the optical ground-excited state coherences, the real aim of all of this math. These are what enter the perturbation Hamiltonian and the force is the average of the gradient of the perturbation Hamiltonian.

A particular parameter case is plotted in Fig. 2.6 that reproduces both the Doppler and PGC features of the force on the atom. Again we see a capture velocity around the Doppler limit of cooling on the D2 line suggesting a two stage cooling method. However, the PGC regime is fairly low in temperature, on the order of the recoil temperature of $200 \mu\text{K}$, and thus, the validity of these results is questionable. Proper analysis in this regime requires a full accounting of the momentum states of the atom and their recoil from spontaneous emission.

Chapter 3

Experimental Progress Towards Cooling and Readout with $5d_{5/2}$ Quadrupole Line

We now proceed to a discussion of the experimental and technical progress achieved in attempting to implement the theoretical systems of the last chapter.

3.1 685 nm Laser

The primary obstacle to working with the quadrupole transition is to create a laser with a linewidth narrower than the transition and simultaneously able to output enough power to at least partially saturate the transition.

In order to accomplish the first goal we first constructed an External Cavity Diode Laser (ECDL) in the Littman-Metcalf configuration. The primary benchmark here was a laser linewidth narrow enough to be locked via the Pound-Drever-Hall (PDH) method [29] to a very high finesse ULE cavity. Sadly, laser diode technology at 685 nm is still in its infancy though improving due to demand for use in strontium. We found most diodes required a large fraction of their output power to be fed back in order to properly narrow the linewidth. Achieving this benchmark required purchase of a diffraction grating with a blaze angle very near the calculated angle for optimum power feedback into the laser diode.

The other crucial ingredient was finding a suitable laser diode. We tried a number of laser diodes specced at or near 685 nm including the Hitachi HL6750 and HL6738, a Toptica 685-050-4 and a Roithner QL68J6SA. Unfortunately, in all cases we had trouble locking to our high finesse cavity when properly tuned to near the quadrupole line. We believe this is due to a typical

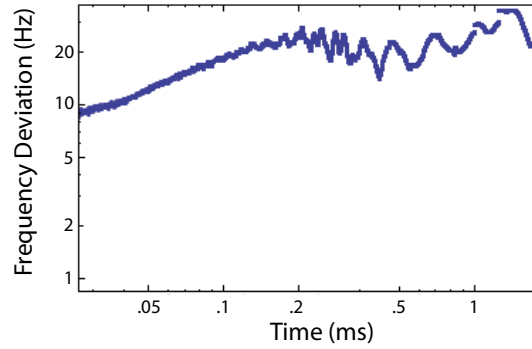


Figure 3.1 Allan Deviation of laser output frequency compared to a reference of the high finesse cavity.

linewidth out of the ECDL of about a MHz and the feedback bandwidth of our locking electronics being only slightly wider at about 1.2 MHz. Finally we tried an anti-reflection coated Sacher SAL-690-025 which produced a 300 kHz linewidth out of the external cavity when pulled to the desired wavelength. In the end this locked to our cavity quite well, but since we did not have a non-AR coated Sacher diode we cannot say for sure whether this was due to superior diodes from Sacher or the AR coating.

The ULE cavity is 10 cm in length and situated in a vacuum can held to approximately 4×10^{-8} Torr. We placed O-rings around the cavity to situate it snugly in the can and filed small holes in the rings to allow pumping throughout the can. On top of the can is a reducing tee connected to a valve followed by an ion pump to maintain vacuum pressure. We wrap two heating strips around the can and attach a thermistor for temperature sensing all of which are attached to a temperature controller. The entire can is then wrapped in insulation to further stabilize the temperature. The ring down time of our cavity suggests a finesse of 150,000. We lock to the transmission peak of the cavity that corresponds to the 0, 1 Hermite-Gaussian mode.

In order to quantify the stability of our lock we measured the Allen Deviation of the output frequency compared to that of the high finesse cavity. Fig. 3.1 displays our results and confirms a frequency noise of less than 100 Hz out to a millisecond which is about the interrogation time needed for readout on the quadrupole line. This, of course, tells us nothing about the frequency drift of our ULE cavity. However, frequency shifts due to temperature fluctuations for a ULE cavity at its zero crossing for the coefficient of expansions are $\approx 10 \text{ kHz/K}^2$ at 685 nm if we take the first

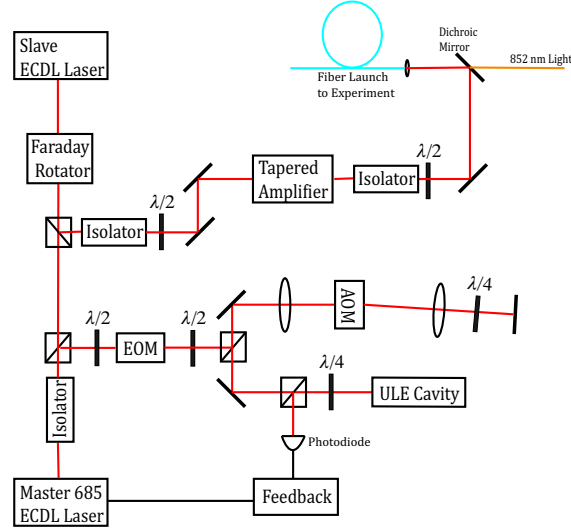


Figure 3.2 High level schematic of final 685 nm laser system.

derivative of the coefficient of expansion of ULE as $\approx 10^9 / \text{K}^2$. With a temperature stability of about a mK this only gives drifts of tens of Hz. We have not done exhaustive searches for the zero crossing, but even in a linear thermal expansion regime ULE has a thermal expansion coefficient of $\approx 10^8 / \text{K}$ which would result in approximately 100 kHz drifts in our setup.

Unfortunately, it quickly became apparent that our system output inadequate power for our purposes. The saturation intensity of the quadrupole line is approximately 1 W/cm or about a thousand times more than the D2 line in cesium. This is a consequence of the very weak transition probability of an E2 transition that overwhelms even the contribution of the narrow linewidth to the saturation intensity. In a stroke of good timing a 690 nm tapered amplifier (TA) from Toptica hit the market. While the amplification and maximum power were not up to the standards of TAs at other wavelengths, it still promised a factor of a hundred increase in power.

However, our ECDL did not output enough power to properly seed the TA and we were forced to first slave a laser to our original ECDL. We chose the Toptica diode for this purpose as it had shown the most power output of all the diodes we tested. With this accomplished we fed the slave output into the TA and realized a large increase in power over our initial setup.

In Fig. 3.2 we provide a high level optical layout of the entire 685 nm system including master ECDL, locking apparatus, slave laser and TA. To give a measure of the power increases wrought

at each step: from the ECDL we measure about 3.5 mW of which about a half mW goes into the locking arm of the setup. The output of the slave laser into the TA is about 20 mW and the maximum we have seen after the TA is 400 mW though we still have room to increase the current into the TA. The TA output is then combined with the 852 nm light we use for our MOT and routed through a fiber entailing a loss of about half our power.

3.2 Spectroscopy and Cooling on the Quadrupole Line

While the literature has accurate measured values for the fine structure energies of $5d_{5/2}$ we only have access to a wavemeter with resolution of 100 MHz and thus our first order of business was to in fact find the line. A heated vapor cell of cesium proved up to the task and we quickly observed the Doppler broadened absorption signal of the $5d_{5/2}$ line.

To make this a cycling transition we need to excite to $F' = 6$ and thus we needed to resolve the hyperfine structure of the level. Saturated absorption spectroscopy in the heated cell failed, likely due to inadequate power at the time. We thus moved to a MOT and attempted to observe a fluorescence signal. This yielded no results until we realized that the combination of the 685 nm light and the trapping light, 532 nm at the time, put us over the ionization threshold. We then

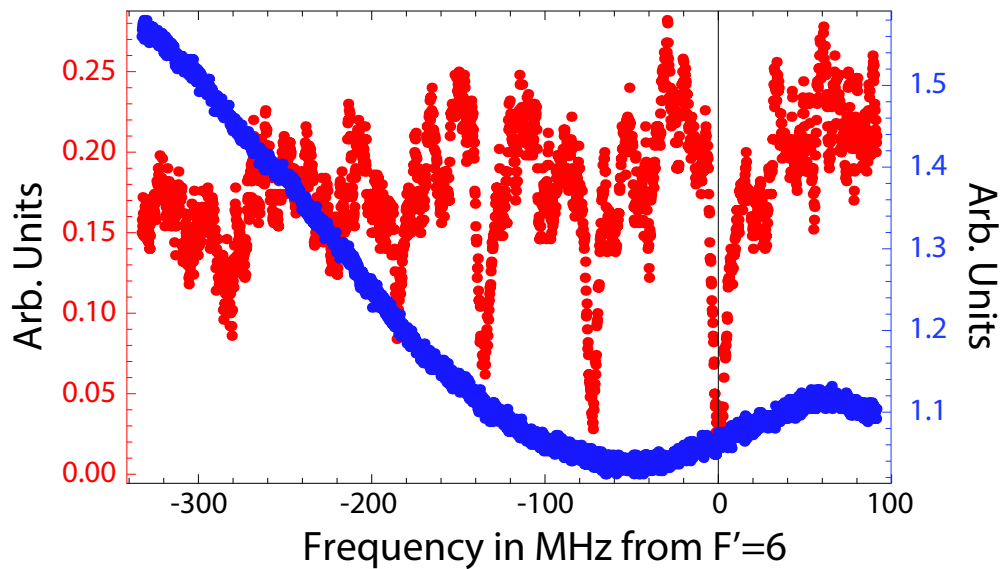


Figure 3.3 Doppler absorption signal (blue) and MOT depletion signal (red).

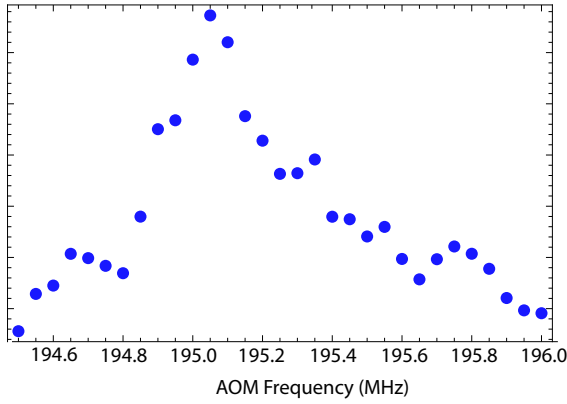


Figure 3.4 Fluorescence signal from a MOT that was further cooled by PGC before applying 685 nm and repumper light for 1 ms.

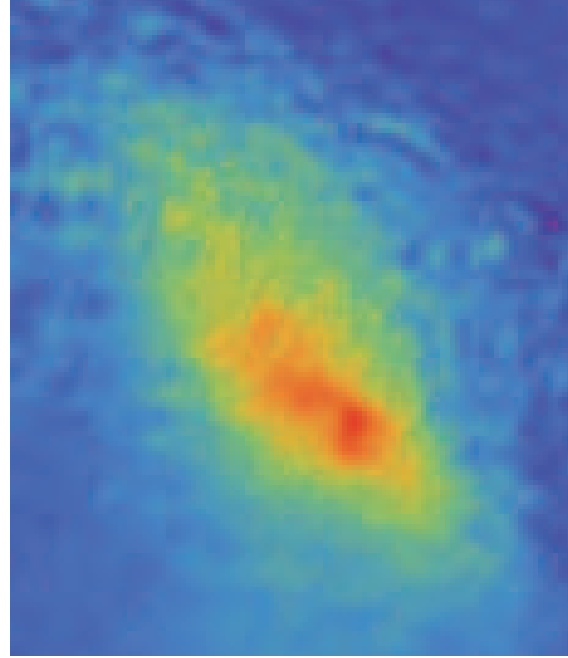


Figure 3.5 Atom cloud immediately after 25 ms of 685 nm light and 4 ms of PGC. This contrasts with no atom cloud without 685. effective power on the atoms was 200 mW with 3 mm diameter beams.

switched to measuring atom loss via photoionization and recorded an unambiguous signal corresponding to the hyperfine levels, see Fig. 3.3. The furthest right and deepest dip corresponds to the $F' = 6$ transition as angular momentum factors give it the highest transition probability. Each dip going left then corresponds to dropping F' by one with 6 through 3 well resolved and $F' = 2$ starting to sink into the noise. Further analysis shows that $F' = 6$ and the bottom of the Doppler peak are separated by approximately 100 MHz, very close to the theoretical value of 99 MHz and that all the other levels are separated very by an amount near their theoretical values, further confirming we indeed measured the hyperfine levels. Unfortunately, we don't have access to a good absolute frequency reference at 685 nm. However, it should be noted that there exists no previous measurement of the hyperfine structure of $5d_{5/2}$ in the literature.

Once we transitioned into a 780 nm trap the threat of photoionization no longer loomed over our head and we once again attempted to observe fluorescence now armed with the proper frequency. This time we succeeded as seen in Fig. 3.4. Furthermore, we managed to see some evidence of a cooling effect from 685. The procedure was to create a MOT then cool it even further by PGC before shining 685 nm on the atoms for 25 ms while keeping the quadrupole MOT field coils on at a reduced value (to compensate for the narrower linewidth) and applying the repumper laser. Subsequent experimentation determined that the repumper had no effect as expected from our analysis of the Raman transition rate for the quadrupole line. We follow this by 4 ms of PGC while the slow mechanical shutter on 685 closed. The application of a small amount of PGC is needed unfortunately to maintain the atoms during this shuttering period. After this sequence we perform a temperature measurement by turning everything off for increasing lengths of time and taking snapshots of the atom distribution with 852 nm light, i.e. a time-of-flight measurement. This revealed that after 29 ms there were atoms remaining in contrast to their complete disappearance with no 685 nm light present. Fitting the atom cloud expansion suggests a temperature of $85\text{ }\mu\text{K}$ at the beginning of the temperature measurement phase. This of course also includes the cooling from PGC and is thus not an unambiguous measurement of cooling temperature on the quadrupole line.

At this point we tabled 685 nm experimentation to pursue other goals more urgently needed for a working quantum computer. Improving the potential for cooling will require a better power balance and alignment of the MOT beams. More 685 nm power would allow a larger beam size than currently allowed and consequently an easier alignment. Readout will require a much lower background count rate than that currently seen which is mostly dominated by the 780 nm trapping light.

Chapter 4

Compensation of Trap Induced Differential Stark Shifts

Atomic clock and quantum information experiments depend on very accurately knowing the energy difference between two states, either for timekeeping purposes or for applying qubit operations. In the case of cesium it would be a state in the $F = 4$ hyperfine manifold and another in the $F = 3$ manifold. Thus, any non-static differential shifts are a significant source of errors. The primary cause of differential shifts in a typical experiment are changes in the magnetic and electric fields experienced by the atom. Two sources of fluctuations in these fields are usually present. If the stability of the trapping light or bias magnetic field is not perfect this will cause a time varying differential shift. Furthermore, an atom at a finite temperature oscillates in its optical trap and thus experiences varying levels of light intensity and magnetic field strength. A differential Stark shift then arises from the slight difference in the coupling of the two hyperfine ground states to excited states by the laser light of the trap. In addition, the magnetic field couples even the nominally Zeeman effect insensitive $m_F = 0$ clock states at the second order resulting in a differential shift at finite field values.

Magic traps are experimental settings for an optical trap that attempt to minimize the sensitivity of the differential shift to changes in either the magnetic field or the intensity of light seen by the atom. Thus we define a magic trap in a field as a trap where the first derivative of the differential shift with respect to that field is zero. A doubly magic trap would manage to set the derivative with respect to both fields to zero. With those conditions the differential shift would be approximately constant for small changes in field strengths.

Various methods for compensating these differential shifts and creating a magic trap exist for a wide array of states and polarizations [30, 31, 32, 33, 34, 35]. One in particular, proposed in [36],

added a second laser that along with a trap laser photon would nearly resonantly couple the two ground states to each other in a two photon process. This proposal shows promise because of its simplicity and efficacy. We could imagine adding a frequency sideband to our trap laser, via an Electro-Optical Modulator, in order to add a second laser frequency which could then compensate for the differential shift by coupling back to the ground state. Our polarizations and intensity profiles would also match, significantly simplifying the experimental setup, and we would have two levers to play with, sideband frequency and intensity. This affords us great flexibility in creating traps insensitive to both magnetic and trap noise.

4.1 The Hyperpolarizability and the Interaction of the Magnetic Field and Trapping Light

The above bichromatic scheme depends crucially on a perturbation term that is fourth order in the electric field amplitude for its efficacy. Previous literature on magic trapping has neglected to realize that even with a monochromatic field a similar fourth order term becomes relevant for alkali atoms at typical trap depths. Now this term is not new, having been discussed in [37] for instance, and has been coined the hyperpolarizability. However, the addition of the hyperpolarizability profoundly affects the differential Stark shift since it pushes the two hyperfine ground states in alkali atoms apart whereas the leading order Stark shift pushes them together. Since the two terms scale differently as a function of the light intensity we would expect that at some point the hyperpolarizability will compensate for the leading order shift and create a trap insensitive at first order to changes in light intensity.

The hyperpolarizability typically becomes important at field strengths around 10^8 V/m [37]. In terms more practical for experiments in atomic physics, an optical dipole trap for Cs atoms based on a modest power of 20 mW at $\lambda = 1.06 \mu\text{m}$ focused to a waist ($1/e^2$ intensity radius) of $w = 2 \mu\text{m}$ gives a field strength of 4.9×10^7 V/m and a trap depth of 15.5 MHz. We can estimate the magnitude of the dipole transition matrix element when the fourth order term surpasses that of the leading order term for a general alkali atom using perturbation theory in a three state system

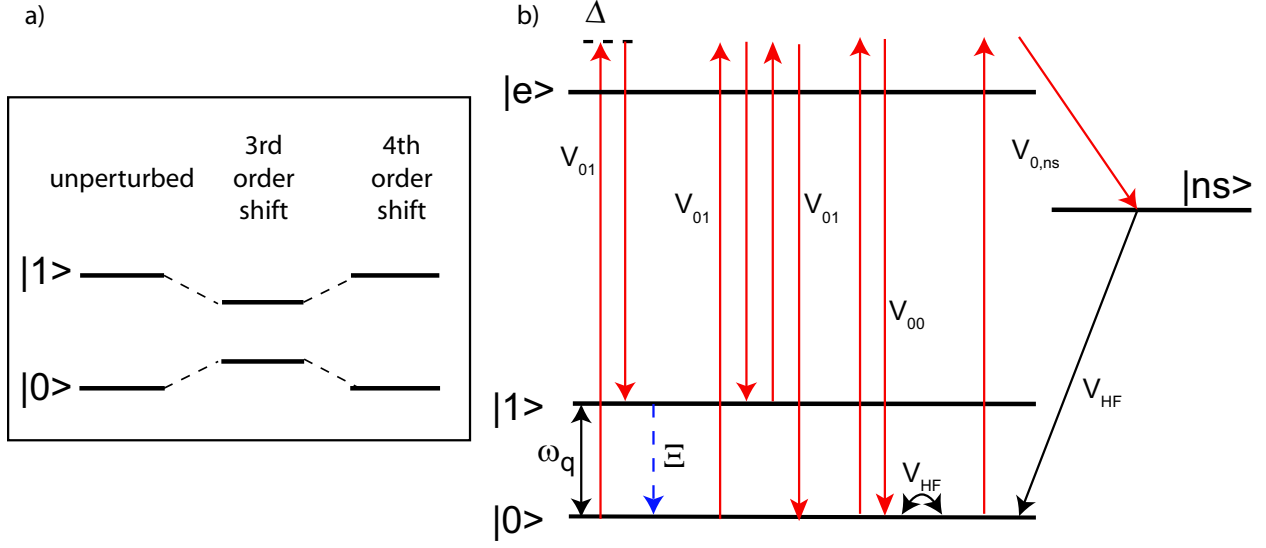


Figure 4.1 (a) Leading order Stark shift and fourth order Stark shift contribute to differential Stark shift of ground states with different signs. (b) Schematic representation of three of the terms important to calculating the differential shift. Here V is the second order electric dipole polarizability, ω_q is the frequency splitting of the two computational states, Ξ is the magnetic dipole coupling from a static magnetic field and finally V_{HF} is the hyperfine mixing interaction. From left to right we have the cross-term of two electric dipole coupling and a magnetic dipole coupling. This can also happen in reverse order thus the extra factor of two. Next is the fourth order term. This is also the important term for the bichromatic scheme except that it couples to the other ground state that is dressed by a sideband energy very close to the qubit splitting. Then, we have the dominant hyperfine mediated polarizability term which is diagonal in the HFI. Lastly, we have the other important third order term which involves hyperfine-induced mixing of an excited s state and the ground s states.

with two ground states and an excited state:

$$\delta E^{(3)} \simeq \frac{-\omega_q V^2}{\Delta^2} \quad (4.1)$$

$$\delta E^{(4)} = \frac{V^4}{\omega_q \Delta^2} + \frac{V^4}{\omega_q (\Delta - \omega_q)^2} \simeq \frac{2V^4}{\omega_q \Delta^2} \quad (4.2)$$

$$\frac{\omega_q V^2}{\Delta^2} = \frac{2V^4}{\omega_q \Delta^2} \rightarrow V^2 = \omega_q^2 / 2 \rightarrow \Omega^2 = 2\omega_q^2. \quad (4.3)$$

Here $V = \Omega/2$ is roughly the matrix element (Rabi frequency) between the ground states and the excited state, ω_q is the hyperfine splitting in the ground state and Δ is the detuning from the

excited state of the trapping light. Thus, the smaller the difference in energy of the two ground states (e.g. rubidium compared to cesium), the smaller the trap intensity before the fourth order term becomes important.

The above is only valid when no magnetic field is present. Apart from the normal first and second order Zeeman shift, if both a magnetic field and an optical trap are applied to the atoms then a third order cross term that includes a magnetic dipole and two electric dipole matrix elements arises. The origin of this term is an electric dipole coupling to an excited state, followed by another electric dipole coupling to the other ground state and finally a magnetic dipole coupling back to the original ground state or the same thing but in reverse order (see Fig. 4.1). Another way to think about is that the two electric dipole couplings combine to form a vector polarizability which can be interpreted as an effective magnetic field and thus this is analogous to a second order Zeeman shift.

Previous literature on the subject of magic traps has failed to grasp the full import of this term. For instance in [38], the author determines the magic magnetic field without this term failing to realize that the magic magnetic field now depends on the light intensity at the atoms. With this term, magic conditions, when the first derivative of the differential shift with respect to the light intensity or magnetic field vanishes, for either field depend on the other and doubly magic conditions boil down to solving a coupled system of equations in both fields as we will show later.

The importance of above the above two terms is exhibited in Fig. 4.2 by sketching magic field points with and without the hyperpolarizability and cross term. The effect is staggeringly significant at typical trap depths and once must conclude that their inclusion is mandatory in a search for magic conditions. It is no longer correct to speak of magic wavelengths, instead one must find magic intensities for specific wavelengths. On one hand, this is unfortunate as previous magic trap conditions essentially presumed to eliminate all sensitivity to electric fields and thus worked at any intensity. On the other, as we will show, this allows for far more flexibility in which wavelengths magic trapping can occur.

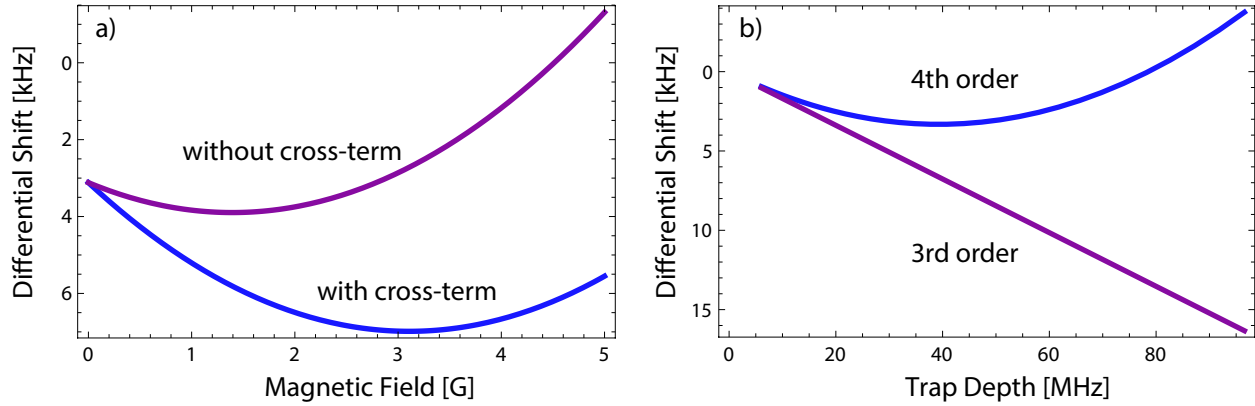


Figure 4.2 Differential light shift (DLS) as a function of trapping light intensity and magnetic field. (a) DLS at $B = 0$ using 2nd order perturbation theory (red) and 4th order (blue) for the Cs clock states $|3, 0\rangle, |4, 0\rangle$ at $\lambda = 1038$ nm. Notice the minimum in the differential shift as a function of the light intensity (trap depth) which constitutes a magic operating point. (b) DLS as a function of the magnetic field with (blue) and without (red) the third order cross-term for $\lambda = 1038$ nm, $\Omega_0/2\pi = 100$ GHz, σ_+ polarization, and the states $|4, 1\rangle, |3, -1\rangle$.

4.2 Magic Trapping for Monochromatic Light Fields

4.2.1 Calculating the Differential Stark Shift by Diagonalization of the Full Hamiltonian

The first step in finding magic trap conditions is accurately determining the differential Stark shift of two basis states. One can, of course, use perturbation theory as in [38] and accompany it with various techniques to optimize the wavefunctions of the basis states. This requires a detailed knowledge of techniques in computational atomic physics that only experts in that field can feasibly develop. In contrast, we will present a method that merely requires a basic knowledge of quantum mechanics and the dressed atom formalism for describing atom-photon interactions. At its simplest it comes down to diagonalizing a Hamiltonian; a function modern computers can handle quickly even with many dimensional systems.

The first step is, as always, constructing the basis states for the calculation. As stated above, dressed states provide a convenient description. We want to calculate the differential Stark shift of cesium's hyperfine ground state and as such, set the center of gravity of the ground state to zero energy. The ground state is then split by the hyperfine interaction. The excited states included are

the ones in the dressed states picture with small energies, in the cases of interest, states where a single photon is subtracted from the field. One then compares the energy of the excited atomic state and the photon field with one fewer photon to the center of gravity and this becomes the energy of that state in the Hamiltonian. In this way one populates the diagonal of the Hamiltonian and does it with exact experimental energies.

Then we must specify the coupling of the various basis states by our laser. This is merely half the normal Rabi frequency between the two states $\Omega_{ij} = \langle i | e \mathcal{E} \epsilon \cdot \mathbf{r} | j \rangle / 2\hbar$, where i, j are collections of quantum numbers $\{nFILLSm_F\}$ with the usual definitions $F = I + J$ and $J = L + S$, I the nuclear spin, L the orbital angular momentum, S the spin angular momentum of the electron and ϵ is the polarization vector, \mathbf{r} the electron position and e the elementary charge of an electron. We can then use the Wigner-Eckart Theorem to decouple the angular momentum down to the J basis.

$$\begin{aligned} \langle n'F'I'J'L'S'm_{F'} | r_q | nFIJLSm_F \rangle = & (-1)^{F'+F+I+J'-m_{F'}} \begin{pmatrix} F' & 1 & F \\ -m_{F'} & q & m_F \end{pmatrix} \sqrt{(2F+1)(2F'+1)} \\ & \times \begin{Bmatrix} J' & F' & I \\ F & J & 1 \end{Bmatrix} \langle n'J'L'S || r_q || nJLS \rangle, \end{aligned} \quad (4.4)$$

where the tensor components r_q needed are determined by $\epsilon \cdot \mathbf{r} = \sum_{q=-1,0,1} r_q \epsilon_{-q}$.

To illustrate the basic idea here is the Hamiltonian in matrix form if we only included the $6p_{1/2}$ excited levels with a σ_+ polarized trap.

$$H = \begin{pmatrix} \omega_0 & 0 & 0 & \Omega_{03} \\ 0 & \omega_1 & \Omega_{12} & 0 \\ 0 & \Omega_{12} & \Delta_p - \Delta_{32} & 0 \\ \Omega_{03} & 0 & 0 & \Delta_p \end{pmatrix}, \quad (4.5)$$

with basis states $|0\rangle = |6s_{1/2}, F=3, m=0\rangle$, $|1\rangle = |6s_{1/2}, F=4, m=0\rangle$, $|2\rangle = |6p_{1/2}, F=3, m=1\rangle$, $|3\rangle = |6p_{1/2}, F=4, m=1\rangle$, $\Delta_p = \omega_{30} - \omega_{laser}$, with $\omega_{30} = \omega_3 - \omega_0$, ω_Λ the energy of a state compared to center of gravity of ground state, and an excited state hyperfine splitting of $\Delta_{32} = \omega_3 - \omega_2$.

Unfortunately, in order to accurately calculate the differential Stark shift, one must also include potential for a two photon excitation to a high lying s state that is connected to the ground state via

small amount of hyperfine-induced mixing. We will split this part of the Hamiltonian into three parts: the atomic energy of these s states, the perturbation due to the laser light that transitions from excited p states to excited s states and finally the hyperfine mixing of s states.

First the diagonal matrix describing the energy of the excited s states is given simply in the dressed state picture as

$$H_s = \sum_s (\omega_s - 2\omega_{laser}) |s\rangle \langle s|, \quad (4.6)$$

where the sum runs over sets of n, F, M for all s states you plan to include in the calculation.

Second, is the counterpart to the perturbation Hamiltonian between $6s \rightarrow np$ already discussed above.

$$H_{sp} = \sum_{i,j} \Omega_{ij} |i\rangle \langle j| + h.c. \quad (4.7)$$

where i and j sums over sets of n, F, J, M for all excited s and p states, respectively.

Finally we come to the hyperfine mixing of the s states. In this case we introduce the following term

$$V_{\text{hf},6sns} = \langle 6s_{1/2} FM | V_{\text{hf}} | ns_{1/2} FM \rangle = A_{6sns} \mathbf{I} \cdot \mathbf{J}. \quad (4.8)$$

One can approximate the hyperfine constant characterizing the mixing as [39]

$$A_{6sns} = \sqrt{A_{6s} A_{ns}}, \quad (4.9)$$

which is verified empirically to work at the 1% level.

With this term the Hamiltonian for this part of the calculation is

$$H_{mix} = \sum_{n,F,M} |ns_{1/2} FM\rangle \langle 6s_{1/2} FM| + h.c., \quad (4.10)$$

Now this only covers the Hamiltonian for the atom and the trapping light. For a full double magic calculation you will also need the Hamiltonian for the magnetic field. In the same basis

$$H_B = \begin{pmatrix} Z_0 & Z_{01} & 0 & 0 \\ Z_{01} & Z_1 & 0 & 0 \\ 0 & 0 & Z_2 & Z_{23} \\ 0 & 0 & Z_{23} & Z_3 \end{pmatrix}, \quad (4.11)$$

with the following definitions for the Zeeman shift $Z_{FM} = M\mu_b g_F B/\hbar$ and the coupling of two states due to a static magnetic field $Z_{FMF'M'} = \mu_B g_J (-1)^{F+I+J+1} \sqrt{(2F+1)J(J+1)(2J+1)} \begin{Bmatrix} J & I & F \\ F' & 1 & J \end{Bmatrix} C_{FM10}^{F'M'}/\hbar$, where g_F and g_J are the Landè g-factors for their respective angular momentum quantum numbers.

From this point one merely need to diagonalize the full Hamiltonian to find the energy eigenvalues of each state and then from that subtract the initial energy of the state to find the total shift. Furthermore, this Hamiltonian can also be used to find the time evolution of all states by matrix exponentiation to get a unitary matrix:

$$U = e^{-iHt}, \quad (4.12)$$

which can then be applied directly to a state or a density matrix.

4.2.2 Calculating Differential Stark Shifts Via An Effective Ground State Hamiltonian

While the above method works excellently, it does require a large matrix that only grows in size as one includes ever more excited states. Another approach is to use polarizabilities to calculate shifts directly or to create an effective Hamiltonian for the ground states to once again diagonalize. Increasing precision by including more excited states is then compacted into computing polarizabilities rather than adding more dimensions to a matrix and it has the further benefit of connecting back to perturbation theory and the processes that contribute to the differential shift.

An example of a Hamiltonian between $|0\rangle = |F = 3, m = 1\rangle$ and $|1\rangle = |F = 4, m = 1\rangle$ in cesium will best elucidate our procedure for searching for double magic traps. Though these states are not ideal for magic conditions, for the case of non-elliptically polarized light their analysis reduces to a simple 2×2 matrix. The following would need to be appropriately modified in the case of searching for magic conditions for states with different m values and elliptical polarizations of light. For instance, the Hamiltonian for non-elliptical light is always constructed from 2x2 block diagonal matrices, making the following analytic analysis always in principle possible. However,

for other polarizations this is no longer the case and a diagonalization of the full Hamiltonian is required.

The effective Hamiltonian for these two states is:

$$\mathcal{H} = \begin{pmatrix} V_{\text{hf},0} + V_{00} + \beta_{00} + Z_{00} & V_{01} + \beta_{01} + Z_{01} \\ V_{01} + \beta_{01} + Z_{01} & V_{\text{hf},1} + V_{11} + \beta_{11} + Z_{11} \end{pmatrix}. \quad (4.13)$$

In this matrix we labeled everything with the kets defined above. The various elements of the matrix are, with i and j standing in for a hyperfine number, F , and Zeeman sublevel, m_F : $V_{\text{hf},i}$ is the diagonal hyperfine interaction, V_{ij} arises from the quadratic polarizability due to the trapping light, β_{ij} is from the third order diagonal and off-diagonal hyperfine-mediated polarizability, Z_{ij} is the magnetic dipole coupling due to the external magnetic field, and Z_{ii} are the first order diagonal Zeeman shifts.

Since this is a two dimensional matrix we can easily write down an analytic expression for the eigenvalues. Replacing the diagonals by $\Delta E_0, \Delta E_1$ facilitates ease of reading and yields

$$\delta E_{1,0} = (\Delta E_0 + \Delta E_1 \pm \sqrt{4(V_{10} + Z_{01})^2 + (\Delta E_1 - \Delta E_0)^2})/2, \quad (4.14)$$

where I have ignored the off-diagonal contribution from β since it is smaller by a factor of a hyperfine mixing matrix element divided by the energy splitting between the ground s state and an excited s state. In the limit where the the hyperfine interaction dominates other perturbations, i.e. $(\Delta E_1 - \Delta E_0)^2 \gg (V_{10} + Z_{01})^2$, the differential shift compared to the hyperfine splitting $V_{\text{hf},1} - V_{\text{hf},0}$ is

$$\delta E = \beta_1 - \beta_0 + Z_1 - Z_0 + 2 \frac{Z_{01}^2 + 2V_{10}Z_{01} + V_{10}^2}{\Delta E_1 - \Delta E_0}. \quad (4.15)$$

$V_{00} = V_{11}$ since the electric dipole operator only couples to the electronic quantum numbers which are the same for both states and thus they cancel out of the differential shift. From here we can make the connection to non-degenerate perturbation theory. The last three terms, from left to right, are: the second order Zeeman shift, the third order cross-term that is two electric dipole matrix elements and one magnetic dipole coupling matrix element and finally a term fourth order in the electric dipole operator. Fig. 4.1 depicts the physical origin of each of the more esoteric terms.

Now we can write down a system of equations that need to be solved for doubly magic conditions to exist. We make the following replacements in order to isolate the dependence on the amplitude of the optical trapping field \mathcal{E} and the magnetic field B : \mathcal{E} and the magnetic field B : $\Omega_0 = \frac{\mathcal{E}}{\hbar} \langle 6p_{1/2} || er || 6s_{1/2} \rangle$, $\beta_{11} - \beta_{00} \rightarrow \beta^{(1)}\Omega_0^2$, $Z_{11} - Z_{00} \rightarrow \mu^{(1)}B$, $2\frac{Z_{01}^2}{\Delta E_1 - \Delta E_0} \rightarrow \mu^{(2)}B^2$, $4\frac{V_{10}Z_{01}}{\Delta E_1 - \Delta E_0} \rightarrow \beta^{(2)}\Omega_0^2 B$, $2\frac{V_{01}^2}{\Delta E_1 - \Delta E_0} \rightarrow \beta^{(4)}\Omega_0^4$. Then the differential shift is

$$\delta E = \mu^{(1)}B + \mu^{(2)}B^2 + \beta^{(1)}\Omega_0^2 + \beta^{(2)}\Omega_0^4 + \beta^{(4)}\Omega_0^2 B, \quad (4.16)$$

and after taking the appropriate derivatives

$$\frac{d\delta E}{dB} = \mu^{(1)} + 2\mu^{(2)}B + \beta^{(2)}\Omega_0^2 \quad (4.17)$$

$$\frac{d\delta E}{d\Omega_0^2} = \beta^{(1)} + \beta^{(2)}B + 2\beta^{(4)}\Omega_0^2. \quad (4.18)$$

Doubly magic trapping occurs when both derivatives simultaneously vanish for a set of parameters (Ω_0, B) , thus eliminating the first order sensitivity to both electric and magnetic fields.

It is the implications of the two terms with coefficients γ and $\beta^{(2)}$ that explain the major difference between this current search for magic traps and previous attempts in the literature. No previous work has even mentioned the latter term with respect to alkali atoms and [38], for example, only incorporated the cross term, with coefficient γ , when calculating the magic wavelength for the electric field when it clearly influences the magic magnetic field as well. Finally, we must note that while the above is a perfectly valid method for determining singly or doubly magic trap conditions (again with proper modifications for different pairs of states and polarizations of light), all results present in this thesis will use a diagonalization of the effective Hamiltonian for all ground states in cesium. In that case, one searches for maxima or minima in the differential shift (in practice, it is always a minima) as a function of both magnetic and electric fields that denotes a doubly magic operating point. Diagonalizing the Hamiltonian is more precise, but the analytic equations above provide a convenient check for any results.

4.2.3 Computing Polarizabilities and Other Terms in the Effective Hamiltonian

We now detail how to compute the various terms that appear in the effective Hamiltonian. Writing down the earlier example Hamiltonian between $|0\rangle = |F = 3, m = 1\rangle$ and $|1\rangle = |F = 4, m = 1\rangle$:

$$\mathcal{H} = \begin{pmatrix} V_{\text{hf},0} + V_{00} + \beta_{00} + Z_{00} & V_{01} + \beta_{01} + Z_{01} \\ V_{01} + \beta_{01} + Z_{01} & V_{\text{hf},1} + V_{11} + \beta_{11} + Z_{11} \end{pmatrix}. \quad (4.19)$$

We have left the hyperfine interaction (HFI) as a perturbation term and thus all of our polarizability terms will use fine structure energy denominators. For the second order polarizability we use the equations of [40].

$$V_{ij} = \frac{\Omega_0^2}{4} \sum_{\substack{K=0,1,2 \\ q=-K,\dots,K}} \alpha_{nJ}^{(K)} \{u^* \otimes u\}_{Kq} (-1)^{J+I+q-M_i+3F_i-M_j} \sqrt{2F_i+1} \\ \times C_{F_i M_i K q}^{F_j M_j} \begin{Bmatrix} F_i & K & F_j \\ J & I & J \end{Bmatrix}, \quad (4.20)$$

with the following further definitions for the reduced polarizability and polarization tensor

$$\alpha_{nJ}^{(K)} = (-1)^{K+J} \sqrt{2K+1} \sum_{n'J'} (-1)^{J'} \begin{Bmatrix} 1 & K & 1 \\ J & J' & J \end{Bmatrix} \left| \frac{\langle n'J' || r || nJ \rangle}{\langle 6p_{1/2} || r || 6s_{1/2} \rangle} \right|^2 \\ \times \left(\frac{1}{\omega - \omega_{n'J'nJ}} + \frac{(-1)^{(K+1)}}{\omega + \omega_{n'J'nJ}} \right), \quad (4.21)$$

$$\{\mathbf{u}^* \otimes \mathbf{u}\}_{Kq} = \sum_{m,m'=0,\pm 1} u_m^* u_{m'} C_{1,m,1,m'}^{K,q}, \quad (4.22)$$

with $K = 0, 1, 2$ a tensor rank corresponding to the scalar, vector and tensor polarizabilities, q a spherical tensor component, \mathbf{u} a polarization vector written in the spherical tensor basis, I the nuclear spin and J, J' the total spin and orbital angular momentum of the ground and excited state, respectively. $\Omega_0 = \frac{\mathcal{E}}{\hbar} \langle 6p_{1/2} || er || 6s_{1/2} \rangle$ is the reduced Rabi frequency with $\mathcal{E} = (2I_0/\epsilon_0 c)^{1/2}$, I_0 is the optical intensity and e is the elementary electric charge. As stated before $\omega_{n'J'nJ}$ is the energy difference between the ground state and an excited state without any hyperfine splitting, i.e. just fine structure energies. We write all of our results in terms of the reduced Rabi frequency,

Ω_0 . Finally, we only included four excited np states in our calculations $6p_{1/2}, 6p_{3/2}, 7p_{1/2}, 7p_{3/2}$. The reduced matrix elements from the $6s_{1/2}$ ground state to these states are given in Appendix C. The static polarizability is dominated by the $6p$ terms, on the order of 96% according to [41], and the dynamic polarizabilities near these transitions are even more dominated by $6p$ since the energy denominators are even smaller for these states by roughly a factor of Δ/ω_{6s6p} with Δ the detuning from $6p$ while leaving relatively unchanged those of other states. The only other notable contribution is from $7p$, being the next allowed dipole transition, but as can be seen the reduced radial matrix element is an order of magnitude smaller along with carrying a much larger energy denominator for the cases we study.

Next is the hyperfine-mediated polarizability, β , that consists of two electric dipole couplings and a HFI coupling. This can be split into 4 broad categories based on the nature of the hyperfine interaction matrix element: diagonal in the ground state, off-diagonal mixing of the ground state with other s and d levels, diagonal in the excited p levels, off-diagonal mixing of excited p levels. We only include the terms with the hyperfine operator in the ground states and further ignore mixing of the s ground state with excited d states as including excited state and other off-diagonal HFI terms results in a smaller than 1% correction. For a more in depth discussion of the hyperfine-mediated polarizability we recommend either [32] for computational details and [42, 43, 44] for a clear physical origin of all the potential terms.

The term with the HFI matrix diagonal in the ground state term can be written as

$$\beta'_{ii} = -V_{\text{hf},i} V'_{ii}, \quad (4.23)$$

where $V'_{ii} = V_{ii}$ with the replacement $(\omega \pm \omega_{n'J'nJ}) \rightarrow (\omega \pm \omega_{n'J'nJ})^2$ and

$$V_{\text{hf},i} = \langle 6s_{1/2} F_i M_i | V_{\text{hf}} | 6s_{1/2} F_i M_i \rangle \quad (4.24)$$

the diagonal matrix element of the standard magnetic dipole hyperfine operator[45] V_{hf} in the ground states.

The other term involving hyperfine mixing of the s ground state with excited ns states is similar to that of the previous section. We again approximate the hyperfine constant characterizing the

mixing as

$$A_{6sns} = \sqrt{A_{6s}A_{ns}}. \quad (4.25)$$

The matrix element is related to this constant in the usual way

$$V_{\text{hf},6\text{sns}} = \langle 6s_{1/2}FM | V_{\text{hf}} | ns_{1/2}FM \rangle = A_{6sns} \mathbf{I} \cdot \mathbf{J}, \quad (4.26)$$

and the operator appearing in the Hamiltonian is

$$\beta''_{ij} = V_{\text{hf},6\text{sns}} V''_{ij}, \quad (4.27)$$

with $V''_{ii} = V_{ii}$ where in one reduced matrix element the ground state is replaced by an excited s state, $\langle 6p_{1/2} || r || 6s_{1/2} \rangle \rightarrow \langle 6p_{1/2} || r || ns_{1/2} \rangle$, and the energy denominator is now $(\omega \pm \omega_{n'J'nJ}) \rightarrow (\omega \pm \omega_{n'J'nJ})(\omega_{6s_{1/2},ns_{1/2}})$ and we include a sum over excited ns states. For this calculation we only include mixing up to $14s_{1/2}$ and use reduced electric dipole matrix elements calculated from a WKB approximation for elements involving $8s_{1/2}$ or higher. It is vital to note that the sign of the reduced matrix elements is now crucial since they are no longer squared in the polarizability, V'' .

Combining the above contributions the hyperfine-mediated polarizability is

$$\beta_{ij} = \beta'_{ij} \delta_{i,j} + \beta''_{ij}, \quad (4.28)$$

where the first term is diagonal and the second also contributes an off-diagonal vector component. We keep this vector component in our calculations though it is dwarfed by the second order vector polarizability by a factor that is approximately the hyperfine mixing matrix element divided by the energy difference between the ground state and an excited s state or $\simeq 10^{-5}$.

Two sources contribute the majority of the error in our calculation. First, the accuracy of our WKB approximation of the reduced dipole matrix elements connecting $6p$ and $7p$ to excited ns levels is unknown. Secondly, β''_{ij} is known to converge slowly as a function of the included excited states and thus our truncation at $14s_{1/2}$ will introduce nontrivial inaccuracies. Comparison with recent experimental determinations of the DC Stark coefficient, k_s , yields an error of approximately 5%. A more pertinent test for our calculations is to compare against the experimental data in [32] for the differential light shift per unit of intensity. For 780 nm light they record $-2.27(40) \times$

10^{-2} Hz/W/cm² compared to our value of -2.02×10^{-2} Hz/W/cm² and for 532 nm light they measured $-3.51(70) \times 10^{-4}$ Hz/W/cm² whereas we calculate -4.08×10^{-4} Hz/W/cm². Thus, in both cases we are within experimental error bars and differ by no more than 15%.

Finally there are Zeeman terms

$$Z_{ij} = \delta_{M_i M_j} \frac{\mu_B (-1)^{F_i+I+J+1} \sqrt{2F_i+1}}{\hbar} C_{F_i M_i 10}^{F_j M_j} \times \left(g_J \sqrt{J(J+1)(2J+1)} \begin{Bmatrix} J & I & F_i \\ F_j & 1 & J \end{Bmatrix} + g_I (-1)^{F_j-F_i} \sqrt{I(I+1)(2I+1)} \begin{Bmatrix} I & J & F_i \\ F_j & 1 & I \end{Bmatrix} \right). \quad (4.29)$$

Here we have specialized to the case of a static magnetic field polarized along \hat{z} . The diagonal coefficients Z_{ii} give the usual expression for the hyperfine Zeeman shifts

$$Z_{ii} = \frac{M_i \mu_B g_{F_i} B}{\hbar}. \quad (4.30)$$

For the Cs ground state $g_J \simeq 2$, $g_{F=3} \simeq -1/4$, $g_{F=4} \simeq 1/4$, and the nuclear Landé factor is $g_I = -0.00039885395$ $\mu_B = -0.73235679 \mu_N$ with μ_B the Bohr magneton and μ_N the nuclear magneton.

4.2.4 Conditions for Magic Trapping in Monochromatic Fields

With the computational preliminaries out of the way we can now investigate conditions for magic trapping. We reiterate a few facts about our calculation. All results are obtained by diagonalizing an effective Hamiltonian of the ground states. We include only $6p_{1/2}$, $6p_{3/2}$, $7p_{1/2}$, $7p_{3/2}$ levels and their counter rotating terms as possible excited state couplings in our polarizability. Hyperfine mixing elements up to $14s_{1/2}$ are accounted for and the needed electric dipole transition elements for these states. All numbers used are listed in Appendix C, the WKB column. Finally, we looked for minima in the differential shift, either in B or Ω_0 or both, depending on whether we were searching for singly or doubly magic traps.

We were, unfortunately, unable to find doubly magic conditions for monochromatic trapping light of any wavelength for any pair of states. This contrasts with previous literature on the subject,

λ (nm)	σ	states	B (G)	$\Omega_0/2\pi$ (GHz)	Trap Depth (MHz)	$\frac{d\delta E}{dB}$ (Hz/G)	$\frac{d^2\delta E}{d\Omega_0^2}$ (10^{-18}Hz^{-1})
1038	+	0,0	1.4	158.0	-60.0	-2440	2.50
1038	+	0,0	1.0	150.0	-54.3	-2440	2.26
1038	+	0,0	0	129.0	-40.3	-2440	1.60
1038	+	1,-1	1.4	164	-66.5	-3680	2.53
945	+	-1,1	1.4	70.8	-23.3	-1000	10.4
820	+	0,0	1.4	70.4	35.5	-3680	22.4
780	+	0,0	1.4	124	49.2	-2720	4.68
780	-	1,-1	1.4	85.6	24.3	1760	2.10

Table 4.1 Intensity magic trap conditions for various wavelengths, light polarizations, pairs of states, and magnetic fields. Also reported are the first order sensitivities to the magnetic field, and the second order sensitivities to the reduced Rabi frequency. The polarization is either σ_+ or σ_- and the states column lists $m_{F=4}, m_{F=3}$. Finally, trap depth for blue detuned traps refers to the light shift the atom experiences at the bottom of the trap rather than the actual depth of the trap. The ground state scalar polarizability is negative for the 780 and 820 nm cases so the trap depths are positive, i.e. repulsive potentials.

but as already stated, they neglected terms that are nontrivial to calculations of the differential Stark Shift. It is possible that some elliptical polarization we did not check or just a more precise calculation could turn up something useful. What we can say is that for most wavelengths, magnetic field strengths, pairs of states and polarizations there is a magic intensity where first-order sensitivity to the light intensity is zero. Table 4.1 provides examples of magic intensities for various wavelengths, bias magnetic fields and pairs of state and the residual sensitivities. As one can see, despite not being truly double magic, the sensitivity to the magnetic field can be quite small for some magic intensity conditions, in particular at 1038nm with the unorthodox $|F = 4, m = -1\rangle$ and $|F = 3, m = 1\rangle$ states. If one can stabilize the magnetic field to $100 \mu\text{G}$ then the above states can have differential shifts of only 0.1 Hz.

It is worth pointing out some of the trends in the Table 4.1. Increasing the bias magnetic field increases the trap depth of the magic intensity for the states 0, 0 and 1, -1. Similarly, increasing the detuning increases the trap depth and decreases the residual sensitivity to the trapping light.

We chose 1.4 G since it is very close to the magic magnetic field with no trapping light and thus elucidates how important a proper accounting of the aforementioned cross-term is for accurately assessing magic conditions.

4.3 Compensation of Differential Stark Shifts by Addition of a Sideband to Trapping Light

While disappointing that doubly magic traps do not appear possible with a monochromatic field, the addition of another laser field with a detuning similar to the hyperfine splitting of the ground states in an alkali atom still provides hope of doubly magic trapping. This idea was first suggested by Radnaev et al. [36]. They envisioned applying another laser that would couple the two ground s hyperfine levels via a two photon transition where the two photon fields differ in frequency by very near the hyperfine splitting of the two ground states. Practically, this could be accomplished by a high frequency electro-optical modulator (or EOM) that can modulate a frequency sideband that is approximately the hyperfine ground splitting away from the carrier signal, e.g. 9.192 GHz in cesium. Thus, we obviate the need for another laser and automatically match the intensity profile of our second light frequency to our trapping frequency.

The second field adds yet another term that is fourth order in the electric field amplitude. This term is much like the fourth order term introduced for a single frequency in that it couples a ground state to the other ground state and back, but in this case that other state is a dressed state nearly resonant with the initial state due to the sideband. Fig. 4.3 elucidates the physical origin of this term. Roughly the term of import is $V_{ij}^s V_{ij}^s / (\omega_q - \omega_s)$ in the polarizability picture, where V_{ij}^s uses the field amplitude of the sideband and the carrier, i.e. $\Omega_0^2 \rightarrow \Omega_0 \Omega_{0,s}$ with $\Omega_{0,s}$ the reduced Rabi frequency of the sideband. The denominator depends on the difference of the sideband and qubit frequencies. This then gives us two levers with which to adjust this fourth order term's magnitude and sign: the intensity of the sideband and its frequency. With that flexibility we will demonstrate that double magic trapping is possible for states separated by one or two photon transitions.

4.3.1 The Full Hamiltonian for Bichromatic Trapping Light

Once again we start by presenting a method by which one arrives at the differential shift by diagonalizing the full Hamiltonian. This is best done by adopting the dressed state formalism. Now our states have three labels: the atomic state and the photon number of our two fields. While there are infinitely many dressed states, the only ones of import are those relatively close in energy. In practice, we only need to include three dressed states for each atomic ground state: $|\Gamma, m+1, n-1\rangle$, $|\Gamma, m, n\rangle$, $|\Gamma, m-1, n+1\rangle$ with energies $E_\Gamma - \omega_s$, E_Γ , $E_\Gamma + \omega_s$, respectively. In these states m and n are photon field numbers with photon energies ω_m and ω_n , the sideband frequency is $\omega_s = \omega_n - \omega_m$ and Γ is again the atomic state with energy E_Γ . The dressed excited states that must be account for are $|\Gamma, m-1, n\rangle$, $|\Gamma, m, n-1\rangle$.

As already pointed out, the important couplings sketched in Fig. 4.3 lead to a term in perturbation theory like $\Omega^2 \Omega_s^2 / (\omega_q - \omega_s)$. When any two levels coupled together in the figure become nearly degenerate the fourth order term becomes very large. This occurs when $\omega_s = \pm \omega_q$ where the sign determines which two of the diagrams becomes nearly resonant. Of course, the strength of this term is also set by the value of Ω and Ω_s , the Rabi frequencies for the carrier and sideband, respectively. Thus, as noted before, we can tune the importance of this fourth-order, two-frequency term by changing the sideband frequency or the intensities.

As an example let us write down the Hamiltonian without including the hyperfine mixing interaction for the four state model of two ground states and two excited states introduced for the monochromatic case with the ordering of basis states $|0, m+1, n-1\rangle$, $|0, m, n\rangle$, $|0, m-1, n+1\rangle$,

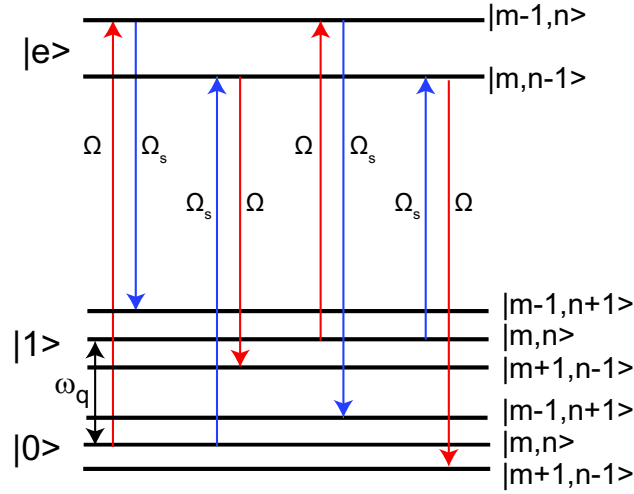


Figure 4.3 Schematic of the couplings contributing to the fourth order term important responsible for the efficacy of a bichromatic optical trap. Each atomic state has three dressed states split by ω_s and labeled on the right by photon field numbers m, n . The sign of the sideband frequency ω_s determines which two of the diagrams contributes most. Ω_s is the electric dipole coupling matrix element for the sideband.

$$|1, m+1, n-1\rangle, |1, m, n\rangle, |1, m-1, n+1\rangle, |2, m-1, n\rangle, |2, m, n-1\rangle, |3, m-1, n\rangle, |3, m, n-1\rangle:$$

$$H =$$

$$\begin{pmatrix} \omega_0 - \omega_s & 0 & 0 & Z_{01} & 0 & 0 & 0 & 0 & 0 & 0 \\ 0 & \omega_0 & 0 & 0 & Z_{01} & 0 & \Omega_{02} & \Omega_{s,02} & \Omega_{03} & \Omega_{s,03} \\ 0 & 0 & \omega_0 + \omega_s & 0 & 0 & Z_{01} & 0 & 0 & 0 & 0 \\ Z_{01} & 0 & 0 & \omega_1 - \omega_s & 0 & 0 & 0 & 0 & 0 & 0 \\ 0 & Z_{01} & 0 & 0 & \omega_0 & 0 & \Omega_{12} & \Omega_{s,1e} & \Omega_{13} & \Omega_{s,13} \\ 0 & 0 & Z_{01} & 0 & 0 & \omega_0 + \omega_s & 0 & 0 & 0 & 0 \\ 0 & \Omega_{02} & 0 & 0 & \Omega_{12} & 0 & \Delta_p - \Delta_{32} - \omega_s & 0 & Z_{23} & 0 \\ 0 & \Omega_{s,02} & 0 & 0 & \Omega_{s,12} & 0 & 0 & \Delta_p - \Delta_{32} + \omega_s & 0 & Z_{23} \\ 0 & \Omega_{03} & 0 & 0 & \Omega_{13} & 0 & Z_{23} & 0 & \Delta_p - \omega_s & 0 \\ 0 & \Omega_{s,03} & 0 & 0 & \Omega_{s,13} & 0 & 0 & Z_{23} & 0 & \Delta_p + \omega_s \end{pmatrix}, \quad (4.31)$$

where all quantities were defined earlier except Ω_s which is calculated like Ω except with the polarization and field amplitude of the sideband. Notice that the magnetic field only couples states with the same photon field numbers. One must also make sure that one uses Ω_s when n changes and Ω when m changes. Once again, diagonalizing this Hamiltonian will yield the differential

shift. In this case the levels of interest are the middle ground dressed states with photon field number $|m, n\rangle$.

4.3.2 The Effective Hamiltonian for Bichromatic Trapping Light

With an effective Hamiltonian we can again eliminate all of the excited states of which there are a multiplicity with sidebands and again reduce the dimensionality of our Hamiltonian by approximately a half. We include the same dressed ground states as for the full Hamiltonian and populate our Hamiltonian using the same equations defined before, ignoring the dressed energy of the excited states.

As an example we utilize the same states as in the Hamiltonian we wrote down for the monochromatic, $|0\rangle = |F = 3, m = 1\rangle$ and $|1\rangle = |F = 4, m = 1\rangle$. Now our basis is $|0, m + 1, n - 1\rangle, |0, m, n\rangle, |0, m - 1, n + 1\rangle, |1, m + 1, n - 1\rangle, |1, m, n\rangle, |1, m - 1, n + 1\rangle$ where m and n are the photon numbers of our two fields with energy ω_m and ω_n , respectively, and $\omega_s = \omega_n - \omega_m$. Our matrix dimension is then threefold larger as each ground state has two additional dressed states that differ in energy by $\pm\omega_s$ from the original state. In all other respects they are identical and the previous definitions for matrix elements are still valid except that we must keep track of when the sideband amplitude is used. To this end we introduce V^s when the sideband is one of the field amplitudes in the polarizability, $\Omega_0^2 \rightarrow \Omega_0\Omega_s$, and assume that when V_{ij} appears that one computes it for the carrier amplitude and the sideband amplitude, $\Omega_0^2 \rightarrow \Omega_s^2$ where Ω_s is the reduced Rabi frequency for the sideband. Finally, for brevity we make the following substitution $\Delta E_i = HF_{\Gamma} + V_{ii} + \beta_i + Z_i$. We write down a 6×6 example Hamiltonian for the ground states in the above basis with non-elliptical polarization.

$$H = \begin{pmatrix} \Delta E_0 - \omega_s & V_{00}^s & 0 & Z_{01} + V_{01} & Z_{01} + V_{01}^s & 0 \\ V_{00}^s & \Delta E_0 & V_{00}^s & Z_{01} + V_{01}^s & Z_{01} + V_{01} & Z_{01} + V_{01}^s \\ 0 & V_{00}^s & \Delta E_0 + \omega_s & 0 & Z_{01} + V_{01}^s & Z_{01} + V_{01} \\ Z_{01} + V_{01} & Z_{01} + V_{01}^s & 0 & \Delta E_1 - \omega_s & V_{11}^s & 0 \\ Z_{01} + V_{01}^s & Z_{01} + V_{01} & Z_{01} + V_{01}^s & V_{11}^s & \Delta E_1 & V_{11}^s \\ 0 & Z_{01} + V_{01}^s & Z_{01} + V_{01} & 0 & V_{11}^s & \Delta E_1 + \omega_s \end{pmatrix} \quad (4.32)$$

At this point one can diagonalize and find the eigenvalues of the states with m, n as their quantum field number to acquire the shifts of the atomic state due to the magnetic and A.C. electric fields. It should be noted that the above formulation breaks down when ω_s becomes small as then the dressed states for a particular atomic state become nearly degenerate. Also since we are ignoring the dressed state energy in the excited state it is imperative that the detuning from any excited state obey $\Delta \gg \omega_s$.

4.3.3 Double Magic Conditions for Bichromatic Traps

With our new computational apparatus we can now attempt a search for double magic traps. Again we diagonalize an effective Hamiltonian of ground states and use only $6p_{1/2}, 6p_{3/2}, 7p_{1/2}, 7p_{3/2}$ levels and their counter rotating terms as possible excited states in our polarizabilities.

In Table 4.2 we present the results of our search for doubly magic conditions at physically feasible parameters. As can be seen, doubly magic conditions exist for blue and red detuned traps and multiple pairs of states. Bringing the sideband frequency closer to the qubit frequency lowers the magic magnetic field, the trap depth and the residual sensitivity to the trapping light. Reducing the sideband intensity reduces the residual light sensitivity for a given magic trap depth and magnetic field. Lastly, the residual magnetic field sensitivity is entirely determined by the pairs of states chosen and even then is approximately the same for all pairs at the double magic point. Thus, bichromatic trapping light allows one to not only create a doubly magic trap but also to tune the parameters of said trap by adjusting the sideband strength and frequency.

Table 4.2 Doubly magic conditions for red and blue detuned traps for different wavelengths, pairs of states, sideband strengths (ratio of sideband field amplitude to carrier field amplitude), sideband frequency, and the residual sensitivities to field fluctuations.

λ (nm)	States	SB Strength	$\omega_s/2\pi$ (GHz)	B (G)	$\Omega_0/2\pi$ (GHz)	Trap Depth (MHz)	$\frac{d^2\delta E}{dB^2}$ ($\frac{\text{Hz}}{\text{G}^2}$)	$\frac{d^2\delta E}{d\Omega_0^2}$ (10^{-18}Hz^{-1})
1038	0,0	0.1	9.15	1.35	88.3	-19	854	2.49
1038	0,0	1	8	1.39	63.6	-19.5	854	4.97
1038	1,-1	1	8	3.63	80.7	-32.2	801	7.5
1038	-1,1	0.1	9	1.78	135	-43.5	801	2.59
920	0,0	0.1	9.185	0.364	17.7	2.26	854	18.5
920	0,0	0.1	9.15	1.54	27.2	-5.89	854	34.6
780	0,0	0.1	9.185	0.27	29.9	2.89	854	3.56
780	0,0	0.1	9.17	0.798	51.4	8.56	854	4.1

Chapter 5

Dissipative Entanglement with Rydberg Atoms

Coherent entanglement of two or more atoms by a Rydberg interaction has already been demonstrated by our group and others. However, this process is plagued by many sources of decoherence; in particular, spontaneous emission. Is there perhaps some way to harness decoherence to our ends and entangle atoms not by avoiding decoherence but through it? Other groups have written extensively on the subject of so-called dissipative entanglement [46, 47, 48, 49, 50] and its power in various important processes in quantum computation [51, 52] and there are even experimental demonstrations [53, 54]. This has led to further investigation of dissipative entanglement in a varied range of physical platforms [55, 56, 57, 58, 59, 60].

It turns out that we can do something similar using Rydberg atoms. A dissipative approach to antiferromagnetic ordering using Rydberg interactions was proposed in [61] and in a similar vein to our own work was a method for creating dark entangled steady states using the Rydberg interaction [62]. Here we consider an arrangement with spin-dependent Rydberg interactions, which allows us to prepare the two-atom spin singlet state as a dark state of the dissipative evolution. In contrast to coherent blockade experiments [63, 7, 64] which rely on minimizing dissipation in order to maximize the fidelity of the target quantum state, the present approach exploits spontaneous emission, yet can be used to prepare a maximally entangled singlet state with fidelity exceeding 0.998. These dynamics enable high fidelity entanglement at long range which will be useful for teleporting gates in a spatially extended qubit array, creating coupled clusters for one-way quantum computing or fabricating strongly correlated spin systems. Remarkably the dissipative approach described here is capable of creating the same entanglement fidelity as a coherent Rydberg blockade gate [65] but with 1500 times smaller Rydberg interaction. This implies that entanglement can

be extended to much larger interparticle separations which will enable efficient computation and many particle entanglement in extended qubit arrays.

5.1 Singlet State Creation Through Dissipative Entanglement

The essential ingredient of our dissipative entanglement scheme is optical pumping. For instance, in our experiment we must optically pump atoms into our computational basis of the two $m_F = 0$ states of our two hyperfine ground states. In order to accomplish this task we apply a π polarized beam of light resonant between the $F = 4$ ground state and the $F' = 4$ excited state. Due to the dipole selection rules this is a forbidden transition for atoms in $F = 4, m = 0$ ground state, that is $\Delta m_F \neq 0$ when $F = F'$ and $m_F = m_{F'} = 0$ and thus this is a “dark” state for this laser. Atoms in any other Zeeman level are excited with no change in m_F and then spontaneously relax back to a ground state but with $\Delta m_F = -1, 0, +1$. We have a repumper that connects the $F = 3$ ground state to an $F' = 4$ excited state that prevents occupation of the $F = 3$ ground state and allows spontaneous emission back to the $F = 4$ ground state. After many excitations atoms will eventually random walk into $F = 4, m_F = 0$ and then become dark to the lasers. In this way we prepare atoms in the computational basis.

The trick then is arrange our lasers such that an entangled state is the dark state. This of course requires some sort of interaction between atoms which is conveniently supplied by the Rydberg interaction. Except that in this case rather than utilize a blockade effect we will use an anti-blockade where the Rydberg interaction brings an excitation process into resonance.

A toy model with two atoms and only four levels that ignores Zeeman degeneracy is most suitable for understanding the scheme and simulating it. In this model we have two ground states, $|1\rangle$ and $|2\rangle$, split by a hyperfine interaction and two different Rydberg levels, $|3\rangle$ and $|4\rangle$. The crucial detail about these Rydberg levels is that their Rydberg interaction differs depending on the Rydberg state of a nearby atom. Mathematically, the interaction of two atoms in the same state is $V_{44} = V_{33}$ and atoms in different states $V_{43} = V_{34}$ and $V_{44} \neq V_{43}$. The idea of utilizing asymmetric Rydberg states for quantum state control is not new having been explored in several other papers [66, 67, 68].

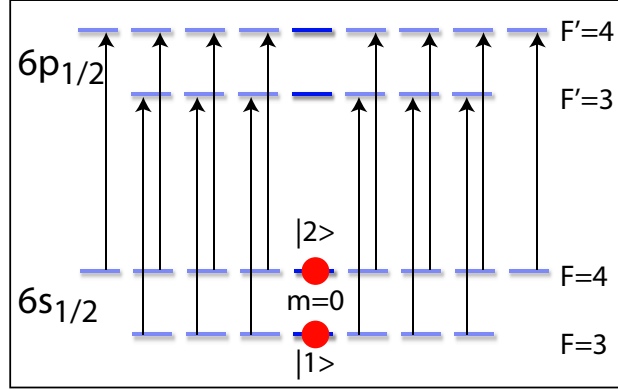


Figure 5.1 Overview of standard optical pumping procedure to produce atoms in the computation basis states. A π polarized optical pumping laser connects the $F = 4$ ground state to the excited state except for the $m_F = 0$ projection. A repumper laser connects $F = 3$ to the excited state.

After many spontaneous emissions the atom will end up in the "dark" state $|2\rangle = |F = 4, m_F = 0\rangle$ where it is unaffected by either laser. Ground state rotations via microwaves or optical Raman transitions can prepare then prepare $|1\rangle = |F = 3, m_F = 0\rangle$.

With our atomic structure settled we turn to the required lasers. For each atom we couple one ground state to one Rydberg level. For our purposes we will couple $|1\rangle \rightarrow |3\rangle$ and $|2\rangle \rightarrow |4\rangle$ with the assumption that the hyperfine splitting of the ground states, $|1\rangle$ and $|2\rangle$, is large enough to ignore other potential couplings. That merely leaves us to determine the detuning. As noted earlier we are going to use a Rydberg anti-blockade effect where we tune our lasers to excite both atoms into a Rydberg level simultaneously. As such we set our lasers to a frequency detuning of $\Delta = V_{44}/2$ which is resonant for the two photon process where both atoms are excited to the same Rydberg level.

Before we continue, let us look at the dynamics of this system more closely. We have set our lasers such that atoms in the same ground state will be resonantly excited to the same Rydberg level and then spontaneously decay to either ground state. The process where atoms in different ground state are excited to different Rydberg states is off-resonant by an amount $V_{44} - V_{43}$, thus the aforementioned need for these two values to differ by as much as possible. Finally there is the possibility of a single atom being excited to a Rydberg level, but this process is detuned by $V_{44}/2$. As such the only state that is optically pumped appreciably is when both atoms are in the same ground state. Our dark state is the incoherent superposition of $|12\rangle$ and $|21\rangle$ since spontaneous

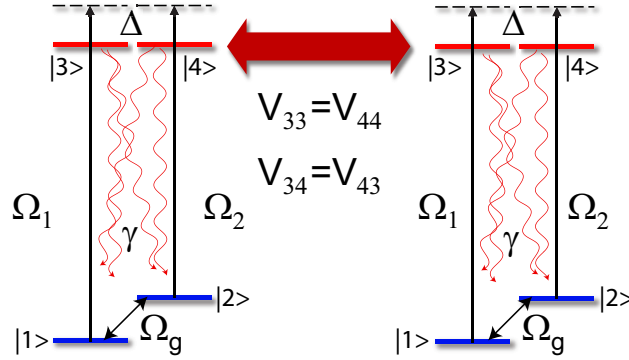


Figure 5.2 Representation of pumping process that creates a singlet or Bell state. $|1\rangle$ is coupled to $|3\rangle$ via Ω_1 and $|2\rangle$ is coupled to $|4\rangle$ via Ω_2 . $\Delta = V_{44}/2$ to make the two photon excitation resonant and V_{44} is much different than V_{34} . Finally, Ω_g is a ground state rotation to ensure pumping out of triplet state. Spontaneous emission at a rate γ from Rydberg levels eventually drives two atom state into $|12\rangle - |21\rangle$, i.e. the singlet or Bell state.

emission, unfortunately, wipes out all phase information. We have therefore created a mixed state and are still one step away from true entanglement.

Producing entanglement then requires the addition of one more coupling, this time between the two ground states. Practically this corresponds to a microwave tuned on resonance to the hyperfine splitting or even an optical Raman rotation between the states. Applying such a ground state rotation allows us to take advantage of the differing structure of the singlet and triplet states of two coupled spins. The singlet state is an $S = 0, m = 0$ state and is thus unaffected by a global rotation; there are literally no other states to rotate into. This is not true for the triplet state. Global ground state rotations cause the $|S = 1, m = 0\rangle = |12\rangle + |21\rangle$ to rotate into the other possible triplet state projections, $|S = 1, m = 1\rangle = |22\rangle$ and $|S = 1, m = -1\rangle = |11\rangle$.

Why are we talking about singlet and triplet states? Because if we squint hard enough at the dark state we created earlier we realize that it is in essence a superposition of the $m = 0$ singlet and triplet states. Therefore applying a global ground state rotation leaves the singlet part alone, but rotates the triplet component into $|11\rangle$ and $|22\rangle$ which are not dark to our lasers. They will then be excited and decay. If they decay into the singlet state they will then stay there as this state is unaffected by our ground state rotation or our Rydberg excitation laser. Otherwise we rotate the triplet state into another angular momentum projection, m , and excite them again. Therefore,

the inclusion of a global ground state rotation has narrowed our dark state to the singlet state $|S = 0, m = 0\rangle = |12\rangle - |21\rangle$ and we have finally entangled two atoms by a dissipative process.

We can make a very good estimate of the fidelity of our entanglement using a simple rate equation analysis. We merely multiply the scattering rate by the probability of decaying into or out of the singlet state to arrive at a set of rate equation for one and two photon processes.

$$r_{1,\text{in}} = (1 - P_{\text{AF}}) 2 \frac{\gamma}{4} \frac{\frac{\Omega^2}{\gamma^2}}{1 + \frac{\Delta_{33}^2}{\gamma^2} + \frac{2\Omega^2}{\gamma^2}}, \quad (5.1a)$$

$$r_{1,\text{out}} = P_{\text{AF}} 2 \frac{3\gamma}{4} \frac{\frac{\Omega^2}{\gamma^2}}{1 + \frac{\Delta_{33}^2}{\gamma^2} + \frac{2\Omega^2}{\gamma^2}}, \quad (5.1b)$$

$$r_{2,\text{in}} = (1 - P_{\text{AF}}) \frac{\gamma}{4} \frac{\frac{\Omega_R^2}{\gamma^2}}{1 + \frac{2\Omega_R^2}{\gamma^2}}, \quad (5.1c)$$

$$r_{2,\text{out}} = P_{\text{AF}} \frac{3\gamma}{4} \frac{\frac{\Omega_R^2}{\gamma^2}}{1 + \frac{4\delta^2}{\gamma^2} + \frac{2\Omega_R^2}{\gamma^2}}. \quad (5.1d)$$

with $\delta = \Delta_{33} - \Delta_{34}$, $\Delta_{33} = V_{33}/2$, $\Omega_R = 2\Omega^2/\Delta_{33}$ the two photon Rabi frequency to the Rydberg level and P_{AF} the population in the singlet state. The factors of $1/4$ and $3/4$ come from the probability to spontaneously decay into the singlet state or into any other state, respectively. There is a 50% probability of decaying into $|12\rangle$ and $|21\rangle$ and another 50% chance that it decays into the singlet and not the triplet state, thus a total of $1/4$ and then its complementary probability $3/4$.

From here we solve $r_{1,\text{in}} + r_{2,\text{in}} = r_{1,\text{out}} + r_{2,\text{out}}$, to find the equilibrium population in the singlet state

$$P_{\text{AF}} = \frac{(\gamma^2 + 4\delta^2 + 2\Omega_R^2) [\Omega_R^2 (\gamma^2 + \Delta_{33}^2) + 2\Omega^2 (\gamma^2 + 3\Omega_R^2)]}{4\Omega_R^2 (\gamma^2 + \Delta_{33}^2) (\gamma^2 + \delta^2 + 2\Omega_R^2) + 8\Omega^2 [\gamma^4 + \gamma^2 (4\delta^2 + 5\Omega_R^2) + 9\delta^2\Omega_R^2 + 6\Omega_R^4]}. \quad (5.2)$$

In the limiting case found by taking $\delta \gg \gamma$, Ω_R , $\Delta_{33} \gg \Omega$ so that both the one and two atom rates out of the singlet state are small, which leads to $P_{\text{AF}} \simeq \left(1 + \frac{\gamma^2}{2\Omega^2}\right) / \left(1 + \frac{2\gamma^2}{\Omega^2}\right)$. We see that provided $\Omega \gg \gamma$, then $P_{\text{AF}} \rightarrow 1$. From this analysis we establish the criteria for good fidelity as: Ω small compared to $\Delta_{33}/2$ to avoid single photon excitation and a large asymmetry in the Rydberg interaction compared to the two photon Rabi frequency to avoid unwanted two photon excitations out of the singlet state.

To further verify the efficacy of our scheme we conducted simulations of a two atom system using a Lindblad master equation formalism. This involves solving the following set of coupled equations

$$\frac{d\rho}{dt} = -\frac{i}{\hbar}[\mathcal{H}, \rho] + \mathcal{L}, \quad (5.3)$$

with $\mathcal{H} = \mathcal{H}_1 \otimes I_2 + I_1 \otimes \mathcal{H}_2 + \mathcal{V}$, $\mathcal{L} = \mathcal{L}_1 \otimes I_2 + I_1 \otimes \mathcal{L}_2$, and I_1, I_2 are 4×4 identity matrices. \mathcal{H}_i are the single atom Hamiltonians and \mathcal{L}_i are Lindblad superoperators constructed from collapse and dephasing operators for each atom.

Working in the interaction picture and making the rotating wave approximation the one atom operators expressed in the basis $\{|1\rangle, |2\rangle, |3\rangle, |4\rangle\}$ are

$$\mathcal{H}_j = \hbar \begin{bmatrix} 0 & \Omega_g^*/2 & \Omega_1^*/2 & 0 \\ \Omega_g/2 & 0 & 0 & \Omega_2^*/2 \\ \Omega_1/2 & 0 & -\Delta & 0 \\ 0 & \Omega_2/2 & 0 & -\Delta \end{bmatrix}, \quad (5.4a)$$

$$\mathcal{L}_j = -\frac{1}{2} \sum_{k,l=1}^4 \gamma_{kl} \left(\sigma_{kl}^{(j)} \sigma_{lk}^{(j)} \rho + \rho \sigma_{kl}^{(j)} \sigma_{lk}^{(j)} - 2\sigma_{lk}^{(j)} \rho \sigma_{kl}^{(j)} \right). \quad (5.4b)$$

In the expression for \mathcal{L}_j , $\sigma_{kl}^{(j)} = |k\rangle^{(j)} \langle l|$ are one-atom operators acting on atom j , $\gamma_{31} = \gamma_{32} = \gamma_{41} = \gamma_{42} = \gamma/2$ and all other $\gamma_{kl} = 0$. Or, in other words, only four operators are nonzero for each atom: $\sigma_{13}, \sigma_{23}, \sigma_{14}, \sigma_{24}$. The interaction term is

$$\mathcal{V} = \hbar \Delta_{33} (|33\rangle \langle 33| + |44\rangle \langle 44|) + \hbar \Delta_{34} (|34\rangle \langle 34| + |43\rangle \langle 43|). \quad (5.5)$$

Numerical solutions of (5.3) are used to extract the fidelity of the Bell singlet state $|-\rangle$ given by $F = \frac{1}{2}(\rho_{11;22} + \rho_{22;11}) + |\rho_{12;21}|$. Values of F found from integrating to $t = 90/\Omega_R$ starting from the initial condition $|11\rangle$ are compared with the approximate result for P_{AF} that comes from solving Eqs. (5.1) in Fig. 5.3.

We see that the approximate result agrees well with numerical solutions. The maximum Bell state fidelity is $F_{\text{Bell}} = 0.9988$ at $\Delta_{33}/2\pi = 3$ MHz. This is essentially the same fidelity as the best found in [65] for the coherent Rydberg blockade controlled phase gate.

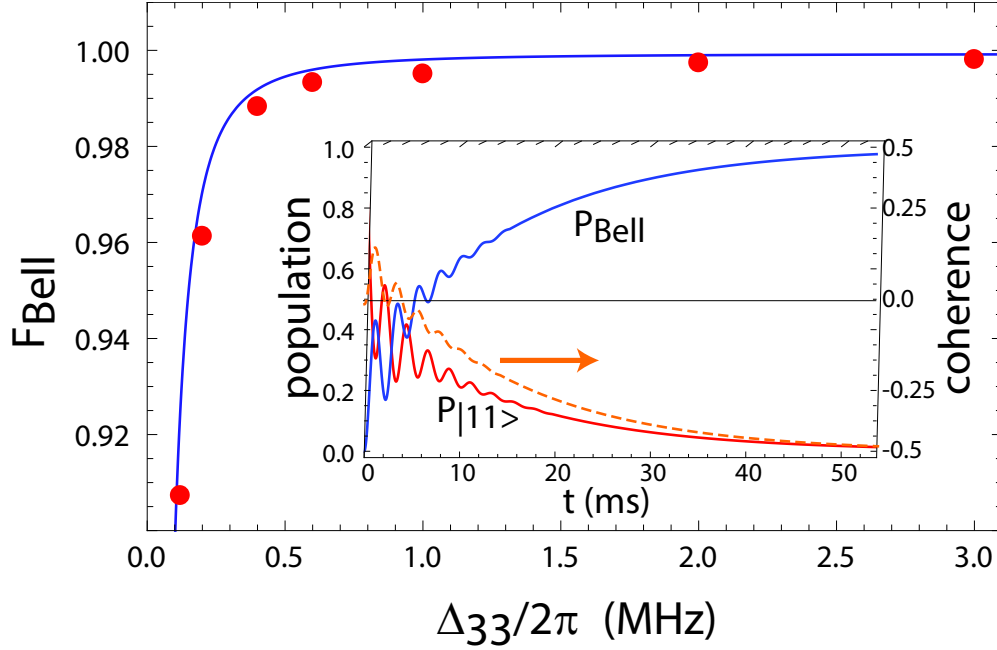


Figure 5.3 Comparison of P_{AF} from Eq. (5.2) (solid line) with singlet state fidelity F_{Bell} from numerical solution of Eq. (5.3) (red dots). Parameters: $\Omega/2\pi = 0.01$ MHz, $\gamma = 1./(0.73 \text{ ms})$, $\Delta_{34}/\Delta_{33} = 0.2$, $\Omega_R = 2\Omega^2/\Delta_{33}$, and $\Omega_g = 0.5\Omega_R$. The atomic parameters correspond to the Cs $125p_{1/2}$ state with $|3\rangle, |4\rangle$ $m_j = \pm 1/2$ and the quantization axis perpendicular to the line containing the atoms. The inset shows the time dependence for $\Delta_{33}/2\pi = 1$ MHz.

Again we reiterate that the dissipative approach does not require single atom addressing and the fidelity is achieved with about 1500 times smaller Rydberg interaction strength than needed for a coherent Rydberg gate. This implies that high fidelity entanglement can be achieved at very much larger atomic separations than entanglement via a coherent interaction. A viable approach to long range gates in an array of qubits could thus be based on teleportation [69] using the dissipative mechanism for establishing entanglement, followed by short range coherent gates between neighboring qubits.

Our calculations ignore undesired entanglement between spin and center of mass degrees of freedom. This can be suppressed, despite the presence of spontaneous emission from the Rydberg levels, provided we confine the atoms in the Lamb-Dicke regime and use magic ground-Rydberg trapping potentials [70]. Furthermore we have ignored Zeeman degeneracy of all levels under the assumption that optical pumping into $m_F = 0$ as described earlier is always present.

5.2 Simulating the Ising Model

Neutral atoms provide a new and powerful tool for exploring many body interactions and quantum magnetism [71, 72, 73, 74]. Recent progress with Rydberg excited atoms [75, 76] has demonstrated strong and long-range dipolar interactions which are suitable for creating magnetic phases with long range order [77, 78, 79, 80, 81, 82]. Of a similar vein to the entanglement scheme presented here is a dissipative approach to antiferromagnetic ordering using Rydberg interactions proposed in [61].

We have already demonstrated a potentially powerful method to entangle atoms that is resistant to some forms of decoherence, but can we go further? What if we could make our dark state the ground state of some interesting Hamiltonian? In that case our optical pumping process could be said to be simulating said Hamiltonian. It turns out that if we look closer at our coupling scheme that we are already simulating a very common condensed matter model: the Ising Model.

5.2.1 Ising Model Without a Magnetic Field

The Ising model is a Hamiltonian for a lattice of spins that interact with each other depending on their spin in the Z direction or explicitly

$$\mathcal{H} = \sum_{\langle i,j \rangle} J_{ij} \sigma_z^{(i)} \sigma_z^{(j)} - \mu \sum_j h_j \vec{\sigma}^{(j)}, \quad (5.6)$$

where i and j sum over every atom pair in the lattice only once and the second term accounts for a magnetic field in some direction. This is about as general as the basic Ising model gets and can be tweaked by adjusting the parameters J and h or how many other atoms each atom interacts with.

It is not immediately clear that the scheme of the previous section simulates the Ising model. Yes, it creates a state that is antiferromagnetic for two atoms, but that is inconclusive evidence. Crucial to understanding how we simulate a Z-Z spin interaction is to realize that our lasers are mapping ground states to Rydberg states. That is, our laser coupling defines $|3\rangle$ as the down state, $|1\rangle$, and $|4\rangle$ as the up state, $|2\rangle$. These Rydberg levels interact with each other and since we mapped our spin states to Rydberg levels this becomes very similar to the J coupling term in the Ising Hamiltonian. The strength of this coupling in our system is proportional to the rate of

excitation to and decay from the particular two atom Rydberg state which we have now associated with the spins in the Ising model.

The two photon Rabi rate is $\Omega_R = \frac{\sqrt{2\Omega_1\Omega_2}}{2\Delta} = \frac{2\Omega_1\Omega_2}{\Delta_{33}}$ where the factor of $\sqrt{2}$ follows because it is a coherent two atom process. The scattering rate from the two atom Rydberg state is then

$$r_R = \frac{\gamma\Omega_R^2}{\gamma^2 + 4\Delta_2^2 + 2\Omega_R^2}, \quad (5.7)$$

where Δ_2 denotes the two photon detuning from the Rydberg level.

Setting the detuning at $\Delta = \Delta_{44}/2$ means that $|44\rangle$ and $|33\rangle$ are resonantly excited, $\Delta_2 = 0$, and have the fastest scattering rate. Or in terms of the Ising model, $J_{44} = J_{33} = J_{\uparrow\uparrow} = J_{\downarrow\downarrow} \sim \Omega_R^2/\gamma$ since for optimal pumping we want $\Delta_{44} \gg \Omega_1, \Omega_2 \gg \gamma$ and $\gamma \gg \Omega_R$. However, for the antiferromagnetic states, $|34\rangle$ and $|43\rangle$, $\Delta_2 = \Delta_{44} - \Delta_{34}$ and $J_{43} = J_{34} = J_{\uparrow\downarrow} = J_{\downarrow\uparrow} \sim \Omega_R^2/4(\Delta_{44} - \Delta_{34})$ assuming an asymmetry in the Rydberg interaction much larger than γ and Ω_R . Thus, the antiferromagnetic interaction is smaller by a factor $\gamma/4(\Delta_{44} - \Delta_{34})$ which we have set to be very small. The lowest energy state of our entanglement scheme, and therefore the ground state, is then the state with spins anti-aligned as in the antiferromagnetic Ising model.

The above describes the admittedly more interesting case of an antiferromagnetic coupling. It is possible to implement a ferromagnetic Ising model in our system by changing the detuning. Set $\Delta = \Delta_{43}/2$ and now the states $|12\rangle$ and $|21\rangle$ are resonantly excited and are swiftly evacuated by our lasers. The dark state is now with spins aligned, $|11\rangle$ and $|22\rangle$, which is off-resonant by an amount $\Delta_{44} - \Delta_{43}$.

The above is a plausible justification for the statement that we are simulating an Ising Hamiltonian, but we can go a step further and expand our numerical simulation to more atoms and see if we actually create the ground state of the Ising model. In this case we simulated the dynamics of a four atom square configuration, the simplest two dimensional configuration, but rather than solving the master equation we turned to Monte Carlo methods as the time and memory requirements scale more slowly with the dimension of the system. The details of the Monte Carlo method are widely available [83] and so we will just note that the basic idea is to evolve the wavefunction according to Schrödinger's equation except that we roll the dice, so to speak, to see if the atom spontaneously

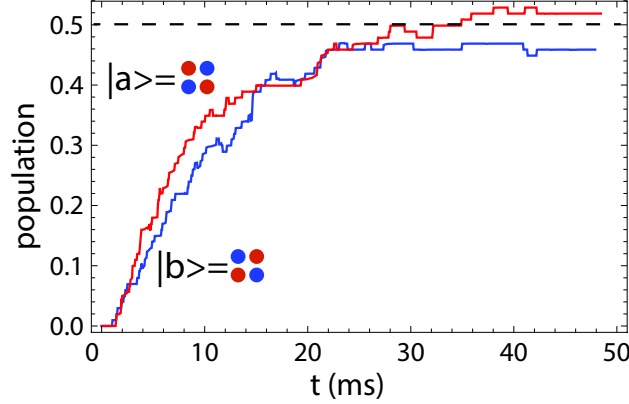


Figure 5.4 Population of AF_{\pm} states from Monte-Carlo simulations of Eq. 5.3 on a square plaquette and averaged over 100 trajectories. The blue and red curves give the populations of $|1212\rangle$ and $|2121\rangle$. Numerical parameters were $\Omega/2\pi = 0.01$ MHz, $\gamma = 1/(0.3 \text{ ms})$, $\Delta_{33}/2\pi = 0.4$ MHz, $\Delta_{34}/\Delta_{33} = 0.85$, $\Delta = \Delta_{33}/2$, $\Omega_R = 2\Omega^2/\Delta_{33}$, and $\Omega_g = 0$. The coupling strengths between opposite corners were $\Delta'_{33} = \Delta_{33}/8$ and $\Delta'_{34} = \Delta_{34}/8$.

decayed back down to the ground state. A single simulation, known as a trajectory, is not a precise or accurate simulation of the system since it has these probabilistic quantum jumps. Instead we run many of these trajectories and average the results to get an idea of the average system dynamics.

Extension of the Hamiltonian and collapse operators of Eq. 5.3 to four atoms is fairly straightforward, mostly involving further Kronecker products of the single atom operators already described to span the now 256 dimensional subspace. The only exception is the interaction Hamiltonian. Now we have the possibility of more than two atoms excited to Rydberg states and we must say something about the Rydberg interaction between atoms on diagonally opposite corners of our square plaquette. We have chosen to include an appropriately scaled interaction between diagonal atoms both for fidelity with an actual experiment and because it would allow us to test our simulation in the presence of a next nearest neighbor interaction. Such an interaction would have a strength $\Delta_{44}/2^3$ since the Rydberg interaction scales as r^{-6} and the atoms are $\sqrt{2}$ lattice spacings apart. With these considerations the interaction Hamiltonian is:

$$\mathcal{V} = \sum_{ijkl} \hbar (\Delta_{ij} + \Delta_{ik} + \Delta_{jl} + \Delta_{kl} + (\Delta_{il} + \Delta_{jk})/8) |ijkl\rangle \langle ijkl|. \quad (5.8)$$

The atoms are labeled such that i is in the top left, j top right, k bottom left and l bottom right and Δ_{mn} is still only nonzero for $\Delta_{33} = \Delta_{44} \neq \Delta_{34} = \Delta_{43}$. As one can see in Fig. 5.4, we make a state

where adjacent spins are antiparallel as we would expect for the ground state of the antiferromagnetic Ising model. We should note that despite the bevy of Rydberg excited states now possible, the detuning is still set to resonantly drive only the two photon excitation for directly adjacent atoms. As discussed before it is the scattering rate of the two photon excitation that determines the J coupling in the Ising Hamiltonian and thus by setting the detuning for directly adjacent atoms we make sure their coupling is strongest. Finally, for these simulations no ground state rotations were included and our final state is a mixed state of the two possible antiferromagnetic states.

Results for four atoms on a square plaquette are given in Fig. 5.4. When there is no transverse field ($\Omega_g = 0$) we pump close to 100% of the population into a superposition of the $M = 0$ states $|a\rangle = |1212\rangle$ and $|b\rangle = |2121\rangle$, corresponding to the ground state of the Ising model (5.6) with $h = 0$. The remaining few percent of the population is fairly evenly distributed over the 12 higher energy states. Solution of (5.6) on a square plaquette with $1/R^6$ van der Waals scaling of the interaction strength shows that the ground states have energy $\frac{-15J}{4}$, while the next four states are at $\frac{-J}{4}$. Our physical model with Rydberg interactions and dissipation shows relaxation to the ground state with purity of about 96%.

5.2.2 Antiferromagnetic Ising Model With a Transverse Magnetic Field

The last section provided very good evidence that our scheme is a reasonable facsimile of the Ising model. Yet the problems we have simulated so far do not require the full power of a quantum simulator and are reasonably tractable on a classical computer. The really hard Ising problem is either in three dimensions or taking the two dimensional problem and adding a magnetic field [84].

Thankfully, adding a transverse magnetic field is something we have already developed; it's just our global ground state rotation. It's easy to see this if we just explicitly write out the Hamiltonian

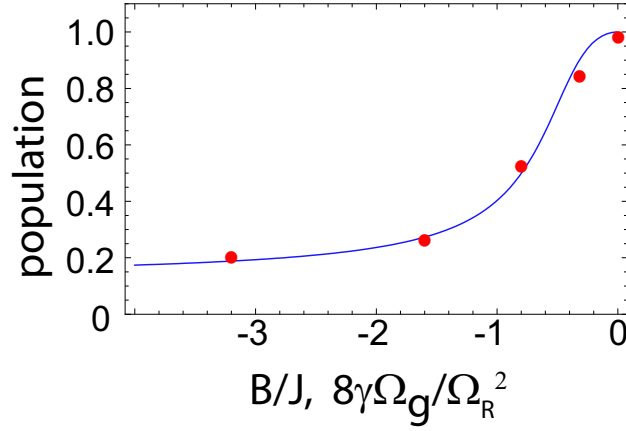


Figure 5.5 The total population in states $|1212\rangle$ and $|2121\rangle$ as a function of B/J from numerical diagonalization of Eq. 5.6 (solid blue line) and from Monte-Carlo simulations of Eq. 5.3 (red dots).

of a two level atom in a transverse magnetic field or with a ground state rotation.

$$-\mu h \sigma_x = \begin{pmatrix} 0 & -\mu h \\ -\mu h & 0 \end{pmatrix}, \quad (5.9a)$$

$$\frac{\Omega_g}{2} |2\rangle\langle 1| + H.c. = \begin{pmatrix} 0 & \Omega_g^*/2 \\ \Omega_g/2 & 0 \end{pmatrix}. \quad (5.9b)$$

With this equivalence recognized it is merely a matter of running the numerical simulations of the previous section but flipping the global ground rotations back on. In order to confirm that we are indeed seeing the correct behavior as we alter our magnetic field strength, Ω_g , we compared our simulation results to a simple diagonalization of a four atom square Ising model with a transverse magnetic field. For large transverse magnetic fields we expect a strong polarization along the direction of the magnetic field which results in all atoms being in a superposition of the two ground states. Our numerical simulation results in Fig. 5.5 shows the proper behavior with each antiferromagnetic state asymptotically approaching 1/16 of the total population.

As explained before, we identify the spin-spin coupling strength J as proportional to our two photon scattering rate Ω_R^2/γ . If we account for the factor of 1/4 that arises from the probability to scatter into the antiferromagnetic ground state then we would predict the ratio of B/J in the Ising model to correspond to $2\gamma\Omega_g/\Omega_R^2$ where another factor of 1/2 arises from $\Omega_g/2 \leftrightarrow B$.

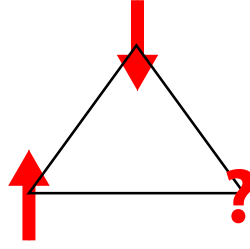


Figure 5.6 The simplest case of frustrated magnetism. Here three spins interact with the same coupling strength. With antiferromagnetic coupling, which spin state should the third spin be to minimize the energy of the system?

Fig. 5.5, plots our results as a function of the ratio B/J for diagonalization of the four atom Ising Hamiltonian and our numerical Monte Carlo simulation. Unfortunately, in order to get good agreement between these methods we have to make a correspondence $B/J \leftrightarrow 8\gamma\Omega_g/\Omega_R^2$ rather than the factor of 2 we would have predicted. The source of this discrepancy is currently not understood.

5.2.3 Frustrated Ising System

An interesting situation occurs in the Ising model when we have a geometry that allows a multitude of degenerate ground states. The simplest example would be placing three spins on the vertices of an equilateral triangle as in Fig.5.6. If two of the spins are antiparallel, what do we expect the third spin to be? Either spin state would minimize the system's energy and in fact this system has six degenerate ground states; all the states where one spin is antiparallel to the other two.

We can check if that is the case for our simulation of the Ising model. For this purpose we find steady state solutions to the full master equation to extract the steady state population of each of the degenerate ground states. In this case our interaction Hamiltonian is

$$\mathcal{V} = \sum_{ijk} \hbar (\Delta_{ij} + \Delta_{ik} + \Delta_{jk}) |ijk\rangle \langle ijk|.$$

State	Steady State	Post-Relaxation
$\downarrow\downarrow\downarrow$	0.029	0.064
$\downarrow\downarrow\uparrow$	0.110	0.145
$\downarrow\uparrow\downarrow$	0.110	0.145
$\downarrow\uparrow\uparrow$	0.110	0.145
$\uparrow\downarrow\downarrow$	0.110	0.145
$\uparrow\downarrow\uparrow$	0.110	0.145
$\uparrow\uparrow\downarrow$	0.110	0.145
$\uparrow\uparrow\uparrow$	0.029	0.064

Table 5.1 Populations of the 8 possible ground states in a steady state configuration with all laser fields on and then the populations after turning laser fields off and allowing excited states to relax for $20\pi/\gamma$.

As Table 5.1 shows, we do indeed see the bulk of the population evenly distributed in the six degenerate ground states with exactly two spins aligned. The steady state fidelity is only 66%, but if we allow all the excited states to relax then our fidelity shoots up to 87%.

5.3 Other Potential Applications

Our technique is quite flexible. We can map arbitrary ground states to Rydberg states and couple them, opening up the possibility of simulating couplings other than $Z - Z$ spin interactions. We have also demonstrated that the strength of our spin couplings is related to the strength of scattering from multiply excited Rydberg states and thus we can manipulate that strength by changing the detuning. Change it enough and the spin coupling turns ferromagnetic. This ability to tune various parameters opens up the possibility of simulating a Spin Glass or Heisenberg Hamiltonian. A disclaimer, the following ideas are currently speculative and would require further study to fully gauge their efficacy.

5.3.1 One-Way Quantum Computing

Earlier we mentioned the possibility of using the fact that our entanglement scheme requires relatively weak Rydberg interactions compared to a coherent Rydberg gate to entangle atoms relatively far away physically. Doing so would allow implementation of something like the quantum teleportation protocol described in [69].

Another potential avenue for exploiting the nature of this dissipative entanglement scheme as simultaneously an Ising spin model is that of one-way quantum computing. The basic idea behind a one-way quantum computer is to entangle a number of atoms together into something called a resource or cluster state. You then measure the qubits in a particular order and in a basis that depends on previous measurement results and finally end up with the answer to your computation. This is equivalent to the quantum circuit model despite the much different methods for proceeding [85].

Where our entanglement scheme comes in is for preparation of the cluster state. It turns out that preparation of a cluster state is equivalent to the quantum Ising spin model [85, 86]. Thus our scheme is suitable for creating the cluster states used in one-way computing. Furthermore, one can create cluster states using our scheme without single-site addressing. For instance, one laser beam large enough to give similar scattering rates from all atoms and that is detuned by $\Delta = \Delta_{33}/2$ would simultaneously entangle all atoms. This is potentially faster and certainly experimentally less challenging than creating cluster states via pairwise entanglement.

5.3.2 The Spin Glass

There has already been some discussion in the literature about using Rydberg interactions to model dissipative quantum glasses [87, 88]. Here we consider an expansion of the simple Ising model into that of the spin glass. In this model the interaction of any two spins is arbitrary in strength and sign. That is, the system is comprised of both ferromagnetic and antiferromagnetic couplings of varying strengths and with potentially little pattern across the system.

However, this poses little problem for our scheme as we have already demonstrated how to manipulate the couplings between spins. If one wishes to switch the sign of J just change the

detuning such that the state opposite the one you want is pumped, i.e. pump $|12\rangle$ and $|21\rangle$ for a ferromagnetic interaction and vice versa for an antiferromagnetic interaction. The strength of the coupling is also determined by the detuning or the intensity of the excitation lasers. Thus, the main experimental impediment to implementation of a spin glass with our scheme is that of single site addressing that allows different intensities and detunings on each site.

Unfortunately, much of the interesting physics in spin glass revolves around temperature effects [89], something we have not touched upon at all. The main effect of temperature comes in through the partition function $\mathcal{Z} = \text{Tr}(e^{-\mathcal{H}/k_B T})$, with \mathcal{H} the Hamiltonian, k_B Boltzmann's constant and T the temperature. This has the effect of populating states other than the absolute ground state, suggesting that we could perhaps interpret the imperfect pumping of our procedure as an estimate of the temperature of our simulation. In that case we could manipulate the temperature by adjusting things such as the detuning, Rabi frequency or asymmetry of the Rydberg coupling. However, this correspondence requires further investigation.

5.3.3 Simulating the Heisenberg Model

Now the Ising model is something of a special case of a more complicated model called the Heisenberg model. In contrast to the Ising Hamiltonian, we include spin couplings in all three directions:

$$\mathcal{H} = \sum_{\langle i,j \rangle, k} J_k^{ij} \sigma_k^{(i)} \sigma_k^{(j)}, \quad (5.10)$$

where the only difference is the sum over k runs over x, y and z . Simulating the Heisenberg model is a more relevant problem to the condensed matter field and is only exactly solvable in one dimension [90].

It is helpful to return to the conceptual model for how our scheme simulated the Ising model in order to see how we can extend it to simulating the Heisenberg Hamiltonian. Recall that we mapped the spin up and spin down states to separate Rydberg levels using our lasers. The Rydberg interaction then substituted for our $Z - Z$ coupling. In the same way we can map the eigenstates of the X and Y spin operators to different Rydberg levels and then let the Rydberg interaction stand in for our $X - X$ and $Y - Y$ coupling. Practically this means coupling both ground states to

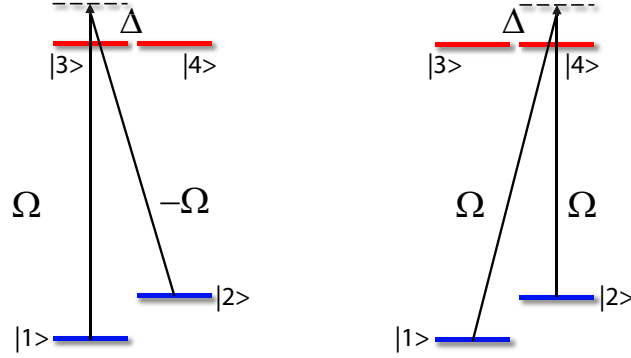


Figure 5.7 Schematic for mapping $|-\rangle_X \rightarrow |3\rangle$ and $|+\rangle_X \rightarrow |4\rangle$ and creating the V_X Hamiltonian. In the left figure notice the relative sign difference between the two coupling lasers that picks out $|-\rangle_X$.

each Rydberg state but injecting a phase shift between the two lasers coupling to the same Rydberg level. For instance to map $|-\rangle_X \rightarrow |3\rangle$ to a Rydberg level we would have a relative minus sign between the laser coupling $|1\rangle \rightarrow |3\rangle$ and the laser coupling $|2\rangle \rightarrow |3\rangle$. This ensures that only the positive eigenstate is excited while the negative eigenstate is unperturbed. Writing out the single atom Hamiltonians for this laser scheme (the Z direction is the same as in the Ising Model):

$$V_X = \frac{1}{2} \begin{pmatrix} 0 & 0 & \Omega & -\Omega \\ 0 & 0 & \Omega & \Omega \\ \Omega & -\Omega & 0 & 0 \\ \Omega & \Omega & 0 & 0 \end{pmatrix}, \quad (5.11a)$$

$$V_Y = \frac{1}{2} \begin{pmatrix} 0 & 0 & \Omega & \Omega \\ 0 & 0 & -i\Omega & i\Omega \\ \Omega & i\Omega & 0 & 0 \\ \Omega & -i\Omega & 0 & 0 \end{pmatrix}. \quad (5.11b)$$

The exact mapping to Rydberg states is not important as long as it is consistent across atoms and it is taken into account when determining the detuning.

A simple test of our scheme is to again look at the two atom case. If the coupling strengths in all three directions are equivalent and negative we expect a spin zero singlet state or in the case of two atoms the typical antisymmetric singlet state of our original entanglement scheme. Therefore,

our test is to see if we can turn off the global ground state rotation and apply our Heisenberg lasers to create the antisymmetric singlet state and indeed that is what we see. Unfortunately, this is a relatively uninformative result as our implementation of an $X - X$ coupling is essentially a Raman rotation equivalent to our ground state rotation, thus we should expect a singlet state even if it is not simulating a Heisenberg Hamiltonian. More suggestive is the fact that any two couplings $Z - X$, $Z - Y$ or $X - Y$ will also produce a singlet state and that is exactly what we see. This is encouraging evidence that we can implement couplings in any direction, but we would need to expand this to four atoms for confirmation. We still expect an $m = 0$ state for four atoms, but analysis is complicated by a number of possible states with zero projection.

Chapter 6

Conclusion

To bring this thesis to an end we will take a short look at the current status of AQUA and the challenges that lie ahead.

We have already crossed the threshold of coherence needed to conclude that we can indeed entangle two neutral cesium atoms in our array. However, we have only done so by a nose. Thus our foremost concern right now is to improve our ability to entangle atoms and achieve a better fidelity CNOT gate. Two primary components go into determining our fidelity: state populations and coherence. These are usually characterized by T_1 and T_2 and the atom lifetime in the trap. The former value is around half a second. The limiting factor for T_1 is Raman scattering from our 780 nm trapping light. Unfortunately, we cannot lower the trap power without lowering the trap depth and we can only accommodate such a change with cooler atom temperatures. Lower temperatures could be achieved using the 685 nm quadrupole transition investigated in this thesis. However, we are currently attempting to implement gray molasses [91] to potentially achieve sub- μK temperatures.

The atom lifetime is quite good, on the order of 10 seconds, far longer than one cycle of our experiment. This only refers to the ground state lifetime. We have noticed that atoms in the Rydberg level seem to escape our trap at higher rates than we would expect from heating, photoionization or other trap loss mechanisms. This loss is convenient for aligning our Rydberg beams, but is a significant source of error when it comes to the fidelity of our entangling gate. Determining the cause of this Rydberg loss and eliminating it should be a primary goal going forward.

The limiting time in our experiment is T_2 which is only about 7 ms. Contributing to this low time scale is magnetic field noise and trap laser intensity fluctuations. Combating these sources of noise was one chapter of this thesis and implementing the bichromatic doubly magic traps investigated earlier would largely eliminate these errors.

Lest we be too negative, we should reiterate what is already accomplished. Though a shaky entangling gate, it is still entanglement. Furthermore, our single qubit rotation fidelity is 99%. We can load 29 single atoms every experiment cycle on average out of a potential 49 sites. These atoms have a temperature in the range of $20 - 40 \mu\text{K}$. We can resolve single sites and measure their state with high fidelity.

The challenges ahead of AQuA are known and ideas for improving them already put forward. We have the utmost confidence that overcoming these technical issues will result in a high fidelity entanglement and the achievement of the many goals outlined at the inception of the AQuA project.

LIST OF REFERENCES

- [1] P. W. Shor, “Algorithms for quantum computation: discrete logarithms and factoring,” in *Foundations of Computer Science, 1994 Proceedings., 35th Annual Symposium on*, pp. 124–134, IEEE, 1994.
- [2] L. K. Grover, “A fast quantum mechanical algorithm for database search,” in *Proceedings of the twenty-eighth annual ACM symposium on Theory of computing*, pp. 212–219, ACM, 1996.
- [3] R. Van Meter, K. M. Itoh, and T. D. Ladd, “Architecture-dependent execution time of shor’s algorithm,” *arXiv preprint quant-ph/0507023*, 2005.
- [4] W. Van Dam, “Quantum oracle interrogation: Getting all information for almost half the price,” in *Foundations of Computer Science, 1998. Proceedings. 39th Annual Symposium on*, pp. 362–367, IEEE, 1998.
- [5] D. P. DiVincenzo, “Topics in quantum computers,” in *Mesoscopic electron transport*, pp. 657–677, Springer, 1997.
- [6] D. Jaksch, J. I. Cirac, P. Zoller, S. L. Rolston, R. Côté, and M. D. Lukin, “Fast quantum gates for neutral atoms,” *Phys. Rev. Lett.*, vol. 85, pp. 2208–2211, 2000.
- [7] L. Isenhower, E. Urban, X. L. Zhang, A. T. Gill, T. Henage, T. A. Johnson, T. G. Walker, and M. Saffman, “Demonstration of a neutral atom controlled-not quantum gate,” *Phys. Rev. Lett.*, vol. 104, p. 010503, 2010.
- [8] M. J. Gibbons, C. D. Hamley, C.-Y. Shih, and M. S. Chapman, “Nondestructive fluorescent state detection of single neutral atom qubits,” *Phys. Rev. Lett.*, vol. 106, p. 133002, 2011.
- [9] A. Fuhrmanek, R. Bourgain, Y. R. P. Sortais, and A. Browaeys, “Free-space lossless state detection of a single trapped atom,” *Phys. Rev. Lett.*, vol. 106, p. 133003, 2011.
- [10] H. Ohadi, M. Himsworth, A. Xuereb, and T. Freearge, “Magneto-optical trapping and background-free imaging for atoms near nanostructured surfaces,” *Opt. Exp.*, vol. 17, no. 25, pp. 23003–23009, 2009.

- [11] N. Linke, D. Allcock, D. Szwer, C. Ballance, T. Harty, H. Janacek, D. Stacey, A. Steane, and D. Lucas, “Background-free detection of trapped ions,” *Appl. Phys. B*, vol. 107, no. 4, pp. 1175–1180, 2012.
- [12] D. A. Steck, “Rubidium 87 d line data (2001),” URL <http://george.ph.utexas.edu/~dsteck/alkalidata/rubidium87numbers.pdf>, 2001.
- [13] D. A. Steck, “Cesium d line data,” *Los Alamos National Laboratory (unpublished)*, vol. 124, 2003.
- [14] R. N. Zare, *Angular Momentum: Understanding Spatial Aspects in Chemistry and Physics*. John Wiley & Sons, Inc., 1988.
- [15] D. James, “Quantum dynamics of cold trapped ions with application to quantum computation,” *Appl. Phys. B*, vol. 66, p. 181, 1998.
- [16] B. Hoeling, J. Yeh, T. Takekoshi, and R. Knize, “Measurement of the lifetime of the atomic cesium $5^2d_{5/2}$ state with diode-laser excitation,” *Opt. Lett.*, vol. 21, p. 74, 1996.
- [17] W. Yei, A. Sieradzian, E. Cerasuolo, and M. Havey, “Measurement of hyperfine coupling constants of the $5d^2d_j$ levels in cs using polarization quantum-beat spectroscopy,” *Phys. Rev. A*, vol. 57, p. 3419, 1998.
- [18] C. E. Theodosiou, “Lifetimes of alkali-metal–atom rydberg states,” *Phys. Rev. A*, vol. 30, p. 2881, 1984.
- [19] W.-K. Lee, H. S. Moon, and H. S. Suh, “Measurement of the absolute energy level and hyperfine structure of the $^{87}\text{rb } 4d_{5/2}$ state,” *Opt. Lett.*, vol. 32, p. 2810, 2007.
- [20] M. Saffman and T. G. Walker, “Analysis of a quantum logic device based on dipole-dipole interactions of optically trapped rydberg atoms,” *Phys. Rev. A*, vol. 72, p. 022347, 2005.
- [21] K. D. Bonin and M. A. Kadar-Kallen, “Theory of the light-force technique for measuring polarizabilities,” *Phys. Rev. A*, vol. 47, p. 944, 1993.
- [22] P. Duarte, R. Hart, J. Hitchcock, T. Corcovilos, T.-L. Yang, A. Reed, and R. Hulet, “All-optical production of a lithium quantum gas using narrow-line laser cooling,” *Phys. Rev. A*, vol. 84, no. 6, p. 061406, 2011.
- [23] D. McKay, D. Jervis, D. Fine, J. Simpson-Porco, G. Edge, and J. Thywissen, “Low-temperature high-density magneto-optical trapping of potassium using the open $4s \rightarrow 5p$ transition at 405 nm,” *Phys. Rev. A*, vol. 84, no. 6, p. 063420, 2011.
- [24] J. Grünert and A. Hemmerich, “Sub-doppler magneto-optical trap for calcium,” *Phys. Rev. A*, vol. 65, no. 4, p. 041401, 2002.

- [25] A. J. Berglund, J. L. Hanssen, and J. J. McClelland, “Narrow-line magneto-optical cooling and trapping of strongly magnetic atoms,” *Phys. Rev. Lett.*, vol. 100, no. 11, p. 113002, 2008.
- [26] M. Lu, N. Q. Burdick, S. H. Youn, and B. L. Lev, “Strongly dipolar bose-einstein condensate of dysprosium,” *Phys. Rev. Lett.*, vol. 107, no. 19, p. 190401, 2011.
- [27] L. Ye, L. Yi-Ge, Z. Yang, W. Qiang, W. Shao-Kai, Y. Tao, C. Jian-Ping, L. Tian-Chu, F. Zhan-Jun, and Z. Er-Jun, “Stable narrow linewidth 689 nm diode laser for the second stage cooling and trapping of strontium atoms,” *Chin. Phys. Lett.*, vol. 27, no. 7, p. 074208, 2010.
- [28] J. Dalibard and C. Cohen-Tannoudji, “Laser cooling below the doppler limit by polarization gradients: simple theoretical models,” *J. Opt. Soc. Am. B*, vol. 6, no. 11, pp. 2023–2045, 1989.
- [29] R. Drever, J. Hall, F. Kowalski, J. Hough, G. Ford, A. Munley, and H. Ward, “Laser phase and frequency stabilization using an optical resonator,” *Appl. Phys. B*, vol. 31, no. 2, pp. 97–105, 1983.
- [30] J. M. Choi and D. Cho, “Elimination of inhomogeneous broadening for a ground-state hyperne transition in an optical trap,” *J. Phys. Conf. Ser.*, vol. 80, p. 012037, 2007.
- [31] V. Flambaum, V. A. Dzuba, and A. Derevianko, “Magic frequencies for cesium primary-frequency standard,” *Phys. Rev. Lett.*, vol. 101, p. 220801, 2008.
- [32] P. Rosenbusch, S. Ghezali, V. A. Dzuba, V. V. Flambaum, K. Beloy, and A. Derevianko, “ac stark shift of the cs microwave atomic clock transitions,” *Phys. Rev. A*, vol. 79, p. 013404, 2009.
- [33] N. Lundblad, M. Schlosser, and J. V. Porto, “Experimental observation of magic-wavelength behavior of ^{87}Rb atoms in an optical lattice,” *Phys. Rev. A*, vol. 81, p. 031611, 2010.
- [34] Y. O. Dudin, R. Zhao, T. A. B. Kennedy, and A. Kuzmich, “Light storage in a magnetically dressed optical lattice,” *Phys. Rev. A*, vol. 81, p. 041805(R), 2010.
- [35] A. Derevianko, “Theory of magic optical traps for Zeeman-insensitive clock transitions in alkali-metal atoms,” *Phys. Rev. A*, vol. 81, p. 051606(R), 2010.
- [36] A. G. Radnaev, Y. O. Dudin, R. Zhao, H. H. Jen, S. D. Jenkins, A. Kuzmich, and T. A. B. Kennedy, “A quantum memory with telecom-wavelength conversion,” *Nat. Phys.*, vol. 6, pp. 894–899, 2010.
- [37] N. L. Manakov, V. D. Ovsiannikov, and L. P. Rapoport, “Atoms in a laser field,” *Phys. Rep.*, vol. 141, p. 319, 1986.
- [38] A. Derevianko, ““doubly magic” conditions in magic-wavelength trapping of ultracold alkali-metal atoms,” *Phys. Rev. Lett.*, vol. 105, p. 033002, 2010.

- [39] A. Derevianko, M. S. Safronova, and W. R. Johnson, “Ab initio,” *Phys. Rev. A*, vol. 60, pp. R1741–R1742, 1999.
- [40] F. Le Kien, P. Schneeweiss, and A. Rauschenbeutel, “Dynamical polarizability of atoms in arbitrary light fields: general theory and application to cesium,” *The Euro. Phys. J. D*, vol. 67, no. 5, pp. 1–16, 2013.
- [41] E. Iskrenova-Tchoukova, M. S. Safronova, and U. I. Safronova, “High-precision study of Cs polarizabilities,” *J. Comp. Meth. Sci. Eng.*, vol. 7, p. 521, 2007.
- [42] P. M. S. Ulzega, A. Hofer and A. Weis, “Reconciliation of experimental and theoretical electric tensor polarizabilities of the cesium ground state,” *EPL*, vol. 76, p. 1074, 2006.
- [43] Ulzega, S., Hofer, A., Moroshkin, P., and Weis, A., “Reconciliation of experimental and theoretical electric tensor polarizabilities of the cesium ground state,” *EPL*, vol. 78, no. 6, p. 69901, 2007.
- [44] A. Hofer, P. Moroshkin, S. Ulzega, and A. Weis, “Calculation of the forbidden electric tensor polarizabilities of free cs atoms and of cs atoms trapped in a solid ^4He matrix,” *Phys. Rev. A*, vol. 77, p. 012502, 2008.
- [45] E. Arimondo, M. Inguscio, and P. Violino, “Experimental determinations of the hyperfine structure in the alkali atoms,” *Rev. Mod. Phys.*, vol. 49, pp. 31–75, Jan 1977.
- [46] M. B. Plenio, S. F. Huelga, A. Beige, and P. L. Knight, “Cavity-loss-induced generation of entangled atoms,” *Phys. Rev. A*, vol. 59, pp. 2468–2475, 1999.
- [47] S. Schneider and G. J. Milburn, “Entanglement in the steady state of a collective-angular-momentum (dicke) model,” *Phys. Rev. A*, vol. 65, p. 042107, 2002.
- [48] D. Braun, “Creation of entanglement by interaction with a common heat bath,” *Phys. Rev. Lett.*, vol. 89, p. 277901, 2002.
- [49] L. Jakobczyk, “Entangling two qubits by dissipation,” *J. Phys. A*, vol. 35, no. 30, p. 6383, 2002.
- [50] A. Basharov, “Entanglement of atomic states upon collective radiative decay,” *J. Exp. and Theo. Phys. Lett.*, vol. 75, no. 3, pp. 123–126, 2002.
- [51] S. Diehl, A. Micheli, A. Kantian, B. Kraus, H. Büchler, and P. Zoller, “Quantum states and phases in driven open quantum systems with cold atoms,” *Nat. Phys.*, vol. 4, no. 11, pp. 878–883, 2008.
- [52] F. Verstraete, M. M. Wolf, and J. I. Cirac, “Quantum computation and quantum-state engineering driven by dissipation,” *Nat. Phys.*, vol. 5, no. 9, pp. 633–636, 2009.

- [53] H. Krauter, C. A. Muschik, K. Jensen, W. Wasilewski, J. M. Petersen, J. I. Cirac, and E. S. Polzik, “Entanglement generated by dissipation and steady state entanglement of two macroscopic objects,” *Phys. Rev. Lett.*, vol. 107, p. 080503, 2011.
- [54] J. T. Barreiro, M. Müller, P. Schindler, D. Nigg, T. Monz, M. Chwalla, M. Hennrich, C. F. Roos, P. Zoller, and R. Blatt, “An open-system quantum simulator with trapped ions,” *Nature*, vol. 470, no. 7335, pp. 486–491, 2011.
- [55] D. Martin-Cano, A. Gonzalez-Tudela, L. Martin-Moreno, F. J. Garcia-Vidal, C. Tejedor, and E. Moreno, “Dissipation-driven generation of two-qubit entanglement mediated by plasmonic waveguides,” *Phys. Rev. B*, vol. 84, p. 235306, 2011.
- [56] K. W. Murch, U. Vool, D. Zhou, S. J. Weber, S. M. Girvin, and I. Siddiqi, “Cavity-assisted quantum bath engineering,” *Phys. Rev. Lett.*, vol. 109, p. 183602, 2012.
- [57] J. Cho, S. Bose, and M. S. Kim, “Optical pumping into many-body entanglement,” *Phys. Rev. Lett.*, vol. 106, p. 020504, 2011.
- [58] G. Kordas, S. Wimberger, and D. Witthaut, “Dissipation-induced macroscopic entanglement in an open optical lattice,” *EPL*, vol. 100, no. 3, p. 30007, 2012.
- [59] E. G. Dalla Torre, J. Otterbach, E. Demler, V. Vuletic, and M. D. Lukin, “Dissipative preparation of spin squeezed atomic ensembles in a steady state,” *Phys. Rev. Lett.*, vol. 110, p. 120402, 2013.
- [60] H. Tan, G. Li, and P. Meystre, “Dissipation-driven two-mode mechanical squeezed states in optomechanical systems,” *Phys. Rev. A*, vol. 87, p. 033829, 2013.
- [61] T. E. Lee, H. Häffner, and M. C. Cross, “Antiferromagnetic phase transition in a nonequilibrium lattice of rydberg atoms,” *Phys. Rev. A*, vol. 84, p. 031402, 2011.
- [62] D. D. B. Rao and K. Mølmer, “Dark entangled steady states of interacting rydberg atoms,” *Phys. Rev. Lett.*, vol. 111, p. 033606, 2013.
- [63] T. Wilk, A. Gaëtan, C. Evellin, J. Wolters, Y. Miroshnychenko, P. Grangier, and A. Browaeys, “Entanglement of two individual neutral atoms using rydberg blockade,” *Phys. Rev. Lett.*, vol. 104, p. 010502, 2010.
- [64] X. L. Zhang, L. Isenhower, A. T. Gill, T. G. Walker, and M. Saffman, “Deterministic entanglement of two neutral atoms via rydberg blockade,” *Phys. Rev. A*, vol. 82, p. 030306, 2010.
- [65] X. L. Zhang, A. T. Gill, L. Isenhower, T. G. Walker, and M. Saffman, “Fidelity of a rydberg-blockade quantum gate from simulated quantum process tomography,” *Phys. Rev. A*, vol. 85, p. 042310, 2012.

- [66] E. Brion, A. S. Mouritzen, and K. Mølmer, “Conditional dynamics induced by new configurations for rydberg dipole-dipole interactions,” *Phys. Rev. A*, vol. 76, p. 022334, 2007.
- [67] M. Saffman and K. Molmer, “Efficient multiparticle entanglement via asymmetric rydberg blockade,” *Phys. Rev. Lett.*, vol. 102, p. 240502, 2009.
- [68] L. Isenhower, M. Saffman, and K. Mlmer, “Multibit c k not quantum gates via rydberg blockade,” *Quantum Information Processing*, vol. 10, no. 6, pp. 755–770, 2011.
- [69] D. Gottesman and I. L. Chuang, “Demonstrating the viability of universal quantum computation using teleportation and single-qubit operations,” *Nature*, vol. 402, no. 6760, pp. 390–393, 1999.
- [70] S. Zhang, F. Robicheaux, and M. Saffman, “Magic-wavelength optical traps for rydberg atoms,” *Phys. Rev. A*, vol. 84, p. 043408, 2011.
- [71] I. Bloch, J. Dalibard, and W. Zwerger, “Many-body physics with ultracold gases,” *Rev. Mod. Phys.*, vol. 80, pp. 885–964, 2008.
- [72] T. Esslinger, “Fermi-Hubbard Physics with Atoms in an Optical Lattice,” in *ANNUAL REVIEW OF CONDENSED MATTER PHYSICS, VOL 1* (Langer, JS, ed.), vol. 1 of *Annual Review of Condensed Matter Physics*, pp. 129–152, 2010.
- [73] C. Trefzger, C. Menotti, B. Capogrosso-Sansone, and M. Lewenstein, “Ultracold dipolar gases in optical lattices,” *J. Phys. B*, vol. 44, no. 19, p. 193001, 2011.
- [74] M. A. Baranov, M. Dalmonte, G. Pupillo, and P. Zoller, “Condensed matter theory of dipolar quantum gases,” *Chem. Rev.*, vol. 112, no. 9, pp. 5012–5061, 2012.
- [75] M. Saffman, T. G. Walker, and K. Mølmer, “Quantum information with rydberg atoms,” *Rev. Mod. Phys.*, vol. 82, pp. 2313–2363, 2010.
- [76] R. Löw, H. Weimer, J. Nipper, J. B. Balewski, B. Butscher, H. P. Büchler, and T. Pfau, “An experimental and theoretical guide to strongly interacting rydberg gases,” *J. Phys. B*, vol. 45, no. 11, p. 113001, 2012.
- [77] H. Weimer, M. Müller, I. Lesanovsky, P. Zoller, and H. P. Büchler, “A rydberg quantum simulator,” *Nat. Phys.*, vol. 6, no. 5, pp. 382–388, 2010.
- [78] H. Weimer and H. P. Büchler, “Two-stage melting in systems of strongly interacting rydberg atoms,” *Phys. Rev. Lett.*, vol. 105, p. 230403, 2010.
- [79] E. Sela, M. Punk, and M. Garst, “Dislocation-mediated melting of one-dimensional rydberg crystals,” *Phys. Rev. B*, vol. 84, p. 085434, 2011.
- [80] I. Lesanovsky, “Many-body spin interactions and the ground state of a dense rydberg lattice gas,” *Phys. Rev. Lett.*, vol. 106, p. 025301, 2011.

- [81] S. Ji, C. Ates, and I. Lesanovsky, “Two-dimensional rydberg gases and the quantum hard-squares model,” *Phys. Rev. Lett.*, vol. 107, p. 060406, 2011.
- [82] W. Zeller, M. Mayle, T. Bonato, G. Reinelt, and P. Schmelcher, “Spectra and ground states of one- and two-dimensional laser-driven lattices of ultracold rydberg atoms,” *Phys. Rev. A*, vol. 85, p. 063603, 2012.
- [83] J. Dalibard, Y. Castin, and K. Mølmer, “Wave-function approach to dissipative processes in quantum optics,” *Phys. Rev. Lett.*, vol. 68, pp. 580–583, 1992.
- [84] F. Barahona, “On the computational complexity of ising spin glass models,” *J. Phys. A*, vol. 15, no. 10, p. 3241, 1982.
- [85] R. Raussendorf, D. E. Browne, and H. J. Briegel, “Measurement-based quantum computation on cluster states,” *Phys. Rev. A*, vol. 68, p. 022312, 2003.
- [86] H. J. Briegel and R. Raussendorf, “Persistent entanglement in arrays of interacting particles,” *Phys. Rev. Lett.*, vol. 86, pp. 910–913, 2001.
- [87] B. Olmos, I. Lesanovsky, and J. P. Garrahan, “Facilitated spin models of dissipative quantum glasses,” *Phys. Rev. Lett.*, vol. 109, p. 020403, 2012.
- [88] I. Lesanovsky and J. P. Garrahan, “Kinetic constraints, hierarchical relaxation, and onset of glassiness in strongly interacting and dissipative rydberg gases,” *Phys. Rev. Lett.*, vol. 111, p. 215305, 2013.
- [89] K. Binder and A. P. Young, “Spin glasses: Experimental facts, theoretical concepts, and open questions,” *Rev. Mod. Phys.*, vol. 58, pp. 801–976, 1986.
- [90] J. Leandri, Y. Leroyer, S. V. Meshkov, Y. Meurdesoif, O. Kahn, B. Mombelli, and D. Price, “Thermodynamics of a mixed quantum - classical heisenberg model in two dimensions,” *J. Phys.: Condensed Matter*, vol. 8, no. 17, p. L271, 1996.
- [91] D. Boiron, C. Triché, D. Meacher, P. Verkerk, and G. Grynberg, “Three-dimensional cooling of cesium atoms in four-beam gray optical molasses,” *Phys. Rev. A*, vol. 52, no. 5, p. R3425, 1995.
- [92] B. Kaulakys, “Consistent analytical approach for the quasi-classical radial dipole matrix elements,” *Journal of Physics B: Atomic, Molecular and Optical Physics*, vol. 28, no. 23, p. 4963, 1995.
- [93] A. Kramida, Y. Ralchenko, J. Reader, and N. A. Team, “NIST Atomic Spectra Database (version 5.1).” <http://physics.nist.gov/asd>, July 2013.
- [94] J. Sansonetti, “Wavelengths, transition probabilities, and energy levels for the spectra of cesium (csi-cslv),” *Journal of Physical and Chemical Reference Data*, vol. 38, no. 4, pp. 761–923, 2009.

- [95] N. P. Georgiades, E. S. Polzik, and H. J. Kimble, “Two-photon spectroscopy of the $6s1/2 \rightarrow 6d5/2$ transition of trapped atomic cesium,” *Opt. Lett.*, vol. 19, pp. 1474–1476, Sep 1994.

Appendix A: Stark Shift Laser

In 2.3.2 we discussed a technique whereby the atom targeted for readout of its quantum state has the D2 line Stark shifted in order to reduce the possibility of scattered photons being absorbed by nearby atoms in the array. It was determined that a laser around 915 nm would be ideal in terms of amount of Stark shift versus unwanted state mixing. In order to implement this technique we fabricated a rather simple laser as shown in Fig. A.1. Since the requirements on frequency stability are quite lax due to its large detuning it is only locked via the PDH method to a medium finesse, $\mathcal{F} \sim 1000$, cavity that is neither temperature stabilized or under vacuum. The output of this laser

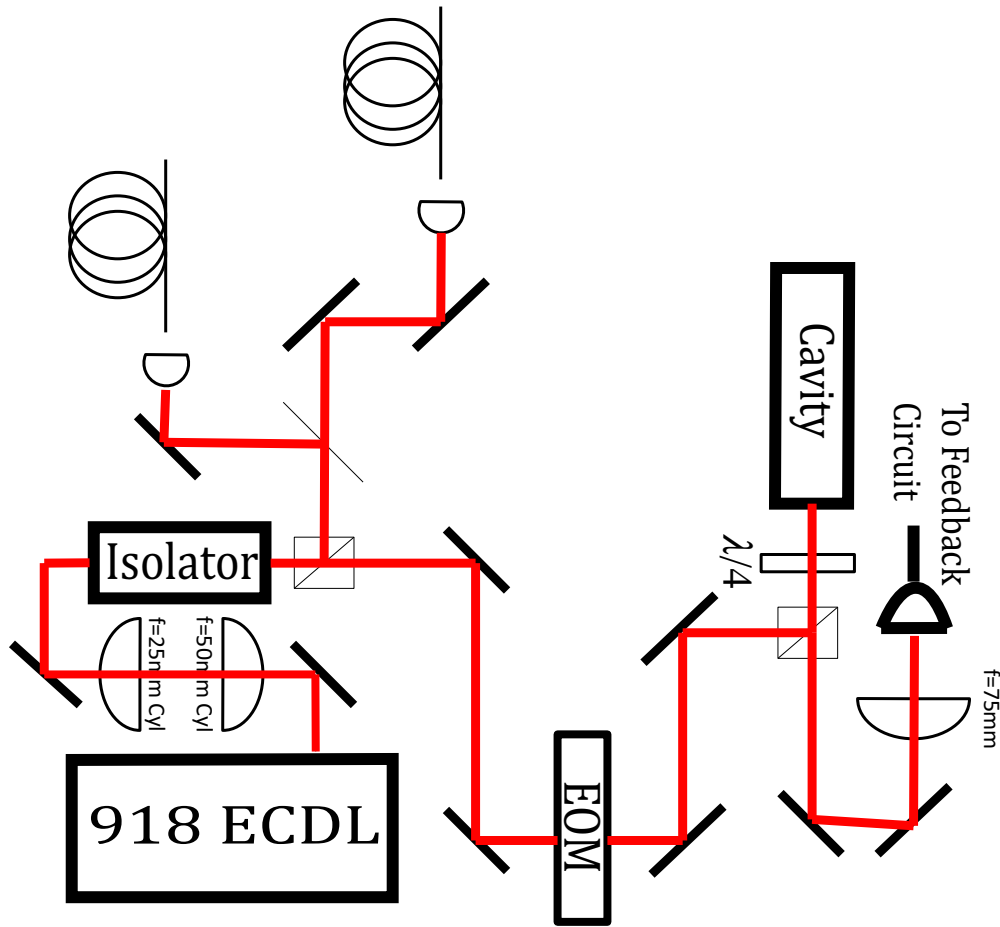


Figure A.1 Layout of the 918 nm Stark shifting laser used to reduce cross-talk during readout.

is taken through a fiber to the experiment where it goes through a two-dimensional beam scanner that allows targeting of single atoms for Stark shifting.

Appendix B: 459 nm Single Site Repumper Laser

AQuA is designed with the ability to address single atoms with blue light for purposes of Rydberg excitation and Raman ground state rotations. We combine these lasers with a repumping laser to enable us to repump only a single site. This is potentially useful for single site readout purposes as well as the ability to reload only one site and optically pump it into our computational states. This laser is tuned to the $|6s_{1/2}, F = 3\rangle \rightarrow |7p_{1/2}, F' = 4\rangle$ transition or 326.2569 THz.

The $7p$ transition is fairly narrow, $\tau = 170$ ns, so once again we utilized a PDH lock to a high finesse, $\mathcal{F} \sim 100,000$ ULE cavity that is temperature stabilized and under vacuum of about 3×10^{-9} Torr. The output of this 918 nm laser is fed into a commercial fiber-in, fiber-out frequency doubler by ADVR, the FIFO110502-459. This is a single pass device meaning the conversion efficiency is not as good as a ring cavity system for instance, but the power requirements for single site repumping are minimal, less than a μ W when focused down to a beam waist of 3μ m. Typical operating powers were 30 mW into fiber input of SHG device and 120 μ W at the fiber output. We

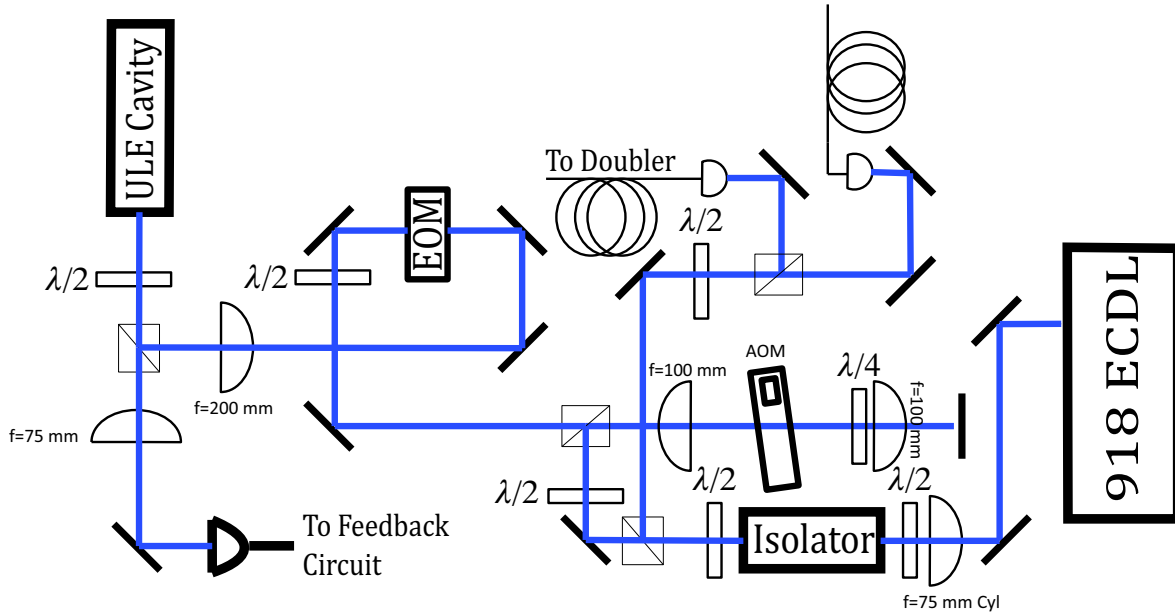


Figure B.1 Layout of the single site 459 nm repumper laser.

have scanned the frequency of this laser and found the desired line. For a short time it was also used to align all of the blue lasers in the experiment to the single atoms in our array.

Appendix C: Numerical Values of Matrix Elements Used to Calculate Magic Trap Parameters

In this section we list the hyperfine constants and radial reduced matrix elements used for calculations. Table I gives hyperfine constants and Tables II-V give radial matrix elements. Where possible we have used numerical values from [41]. For other transitions we have used the values found from WKB calculations following the theory of Ref. [92]. As a check on the WKB calculations we compare them in the tables to the published values in [41] and to Coulomb wave function (Cwf) calculations. The WKB and Cwf calculations use effective quantum defects extracted from the energy values listed in [93, 94]. We estimate the error of the WKB matrix elements to be less than 10% on the basis of comparison to values from [41]. The Cwf and WKB calculations give a value for $R_{nl_j}^{n'l'_{j'}}$ which is converted to a reduced matrix element using

$$\langle n'l'sj' || r || nlsj \rangle = (-1)^{1+s+j+(1+l+l')/2} \sqrt{(2j+1)(2j'+1)\max(l,l')} \begin{Bmatrix} l & s & j \\ j' & 1 & l' \end{Bmatrix} R_{nl_j}^{n'l'_{j'}}.$$

When calculating the third order hf-Stark polarizability the sign of the reduced matrix elements is significant. Note that $\langle n'l'sj' || T || nj \rangle = (-1)^{j-j'} \langle nj || T || n'l'sj' \rangle$. Thus $\langle n'p_{1/2} || T || ns_{1/2} \rangle = \langle ns_{1/2} || T || n'p_{1/2} \rangle$ but $\langle n'p_{3/2} || T || ns_{1/2} \rangle = -\langle ns_{1/2} || T || n'p_{3/2} \rangle$. There is inconsistency in the literature as regards signs of published reduced matrix elements. We have taken the signs from our Cwf or WKB calculations which agree with each other.

state	A (MHz)	B (MHz)
$6s_{1/2}$	2298.1579425	
$7s_{1/2}$	546.3	
$8s_{1/2}$	218.9	
$9s_{1/2}$	110.1	
$10s_{1/2}$	63.2	
$11s_{1/2}$	39.4	
$12s_{1/2}$	26.31	
$13s_{1/2}$	18.40	
$14s_{1/2}$	13.41	
$15s_{1/2}$	10.1 ^c	
$6p_{1/2}$	291.9309 ^c	
$7p_{1/2}$	94.35	
$8p_{1/2}$	42.97	
$9p_{1/2}$	23.19	
$6p_{3/2}$	50.28825 ^c	-0.4940 ^c
$7p_{3/2}$	16.605	-0.15
$8p_{3/2}$	7.58	-0.14
$9p_{3/2}$	4.123	-0.051
$5d_{3/2}$	48.78 ^a	0.1 ^a
$6d_{3/2}$	16.34 ^c	-0.1 ^c
$7d_{3/2}$	7.4 ^c	
$8d_{3/2}$	3.95 ^c	
$5d_{5/2}$	-21.24 ^a	0.2 ^a
$6d_{5/2}$	-4.69 ^b	0.18 ^b
$7d_{5/2}$	-1.7	
$8d_{5/2}$	-0.85	

Table C.1 Some hyperfine constants of Cs. Values from [45] except for a) Ref. [17], b) Ref. [95], c) Ref. [94]

final state	transition wavelength (μm)	theory $\langle nl_j r 6p_{1/2} \rangle^a$	Cwf		WKB
			r_{\min}	$\langle nl_j r 6p_{1/2} \rangle$	$\langle nl_j r 6p_{1/2} \rangle$
$6s_{1/2}$	-0.8946	4.489	0.	4.501	4.482
$7s_{1/2}$	1.359	-4.236	0.	-3.921	-3.970
$8s_{1/2}$	0.7611		0.	-0.9379	-0.9650
$9s_{1/2}$	0.6356		0.	-0.4956	-0.5159
$10s_{1/2}$	0.5840		0.	-0.3270	-0.3434
$11s_{1/2}$	0.5570		0.	-0.2396	-0.2533
$12s_{1/2}$	0.5408		0.	-0.1867	-0.1983
$13s_{1/2}$	0.5303		0.	-0.1513	-0.1614
$14s_{1/2}$	0.5230		0.	-0.1262	-0.1351
$15s_{1/2}$	0.5178		0.	-0.1075	-0.1155
$5d_{3/2}$	3.011	7.06	0.7	7.317	7.056
$6d_{3/2}$	0.8764	-4.15	0.7	-4.002	-4.228
$7d_{3/2}$	0.6725		0.7	-1.976	-2.070
$8d_{3/2}$	0.6012		0.7	-1.256	-1.308

Table C.2 Reduced matrix elements of coupled states $|nlsj\rangle$ in the j basis $\langle n'l'sj' || r || 6p_{1/2} \rangle$ for the Cs $6p_{1/2}$ state and transition vacuum wavelengths. Cwf are values calculated using Coulomb wavefunctions with experimental values for quantum defects, and r_{\min} a small r cutoff to avoid divergence. WKB are values calculated using the theory of [92]. Matrix elements are given in atomic units. a) From [41] with the sign from Cwf calculation.

final state	transition wavelength (μm)	theory $\langle nl_j r 6p_{3/2} \rangle^a$	Cwf		WKB
			r_{\min}	$\langle nl_j r 6p_{3/2} \rangle$	$\langle nl_j r 6p_{3/2} \rangle$
$6s_{1/2}$	-0.8523	6.324	0.	6.309	6.2856
$7s_{1/2}$	1.470	-6.473	0.	-6.026	-6.0946
$8s_{1/2}$	0.7946		0.	-1.349	-1.3847
$9s_{1/2}$	0.6588		0.	-0.7049	-0.7318
$10s_{1/2}$	0.6036		0	-0.4632	-0.4848
$11s_{1/2}$	0.5747		0.	-0.3386	-0.3568
$12s_{1/2}$	0.5575		0.	-0.2634	-0.2789
$13s_{1/2}$	0.5463		0.	-0.2134	-0.2269
$14s_{1/2}$	0.5386		0.	-0.1779	-0.1898
$15s_{1/2}$	0.5331		0.	-0.1515	-0.1621
$5d_{3/2}$	3.614	-3.19	0.7	-3.259	-3.167
$5d_{5/2}$	3.491	9.66	0.7	9.871	9.594
$6d_{3/2}$	0.9211	2.05	0.7	2.003	2.0923
$6d_{5/2}$	0.9175	-6.01	0.7	-5.860	-6.129
$7d_{3/2}$	0.6985		0.7	0.9524	0.9857
$7d_{5/2}$	0.6975		0.7	-2.816	-2.919
$8d_{3/2}$	0.6220		0.7	0.5973	0.6142
$8d_{5/2}$	0.6215		0.7	-1.773	-1.827

Table C.3 Reduced matrix elements of coupled states $|nlsj\rangle$ in the j basis $\langle n'l'sj' || r || 6p_{3/2} \rangle$ for the Cs $6p_{3/2}$ state and transition vacuum wavelengths. Cwf are values calculated using Coulomb wavefunctions with experimental values for quantum defects, and r_{\min} a small r cutoff to avoid divergence. WKB are values calculated using the theory of [92]. Matrix elements are given in atomic units. a) From [41] with the sign from Cwf calculation.

final state	transition wavelength (μm)	theory $\langle nl_j r 7p_{1/2} \rangle^a$	Cwf			WKB
			r_{\min}	$\langle nl_j r 7p_{1/2} \rangle$		$\langle nl_j r 7p_{1/2} \rangle$
$6s_{1/2}$	-0.4594	0.276	0.	0.465		0.4175
$7s_{1/2}$	-3.096	10.308	0.	10.18		10.18
$8s_{1/2}$	3.919	-9.313	0.	-9.115		-9.154
$9s_{1/2}$	1.943		0.	-1.921		-1.940
$10s_{1/2}$	1.530		0.	-0.9761		-0.9909
$11s_{1/2}$	1.358		0.	-0.6338		-0.6460
$12s_{1/2}$	1.265		0.	-0.4612		-0.4716
$13s_{1/2}$	1.209		0.	-0.3583		-0.3674
$14s_{1/2}$	1.172		0.	-0.2904		-0.2985
$15s_{1/2}$	1.146		0.	-0.2424		-0.2497
$5d_{3/2}$	-1.376		0.7	-1.897		-2.091
$6d_{3/2}$	12.14	18.0	0.7	17.92		17.86
$7d_{3/2}$	2.335	6.56	0.7	-6.402		-6.519
$8d_{3/2}$	1.654		0.7	-3.124		-3.193

Table C.4 Reduced matrix elements of coupled states $|nlsj\rangle$ in the j basis $\langle n'l'sj' || r || 7p_{1/2} \rangle$ for the Cs $7p_{1/2}$ state and transition vacuum wavelengths. Cwf are values calculated using Coulomb wavefunctions with experimental values for quantum defects, and r_{\min} a small r cutoff to avoid divergence. WKB are values calculated using the theory of [92]. Matrix elements are given in atomic units. a) From [41] with the sign from Cwf calculation.

final state	transition wavelength (μm)	theory $\langle nl_j r 7p_{3/2} \rangle^a$	Cwf		WKB
			r_{\min}	$\langle nl_j r 7p_{3/2} \rangle$	$\langle nl_j r 7p_{3/2} \rangle$
$6s_{1/2}$	-0.4557	0.586	0.	0.8158	0.7534
$7s_{1/2}$	-2.932	14.320	0.	14.13	14.13
$8s_{1/2}$	4.218		0.	-13.78	-13.84
$9s_{1/2}$	2.014		0.	-2.681	-2.705
$10s_{1/2}$	1.574		0.	-1.343	-1.361
$11s_{1/2}$	1.392		0.	-0.8672	-0.8825
$12s_{1/2}$	1.295		0.	-0.6294	-0.6424
$13s_{1/2}$	1.236		0.	-0.4882	-0.4996
$14s_{1/2}$	1.197		0.	-0.3953	-0.4054
$15s_{1/2}$	1.170		0.	-0.3298	-0.3389
$5d_{3/2}$	-1.343		0.7	0.7573	0.8310
$5d_{5/2}$	-1.361		0.7	-2.369	-2.591
$6d_{3/2}$	15.57	-8.07	0.7	-8.029	-8.011
$6d_{5/2}$	14.59	24.4	0.7	24.22	24.16
$7d_{3/2}$	2.438	3.32	0.7	3.253	3.300
$7d_{5/2}$	2.426	-9.64	0.7	-9.459	-9.604
$8d_{3/2}$	1.705		0.7	1.520	1.546
$8d_{5/2}$	1.702		0.7	-4.473	-4.554

Table C.5 Reduced matrix elements of coupled states $|nlsj\rangle$ in the j basis $\langle n'l'sj' || r || 7p_{3/2} \rangle$ for the Cs $7p_{3/2}$ state and transition vacuum wavelengths. Cwf are values calculated using Coulomb wavefunctions with experimental values for quantum defects, and r_{\min} a small r cutoff to avoid divergence. WKB are values calculated using the theory of [92]. Matrix elements are given in atomic units. a) From [41] with the sign from Cwf calculation.